Development and Assessment of Rare Earth-lean Th_1Mn_{12}-Phases for the Use in Permanent Magnets

Entwicklung und Bewertung seltenerdarmer Th_1Mn_{12}-Phasen zum Einsatz in Permanentmagneten
Zur Erlangung des akademischen Grades Doktor-Ingenieur (Dr.-Ing.)
genehmigte Dissertation von Daniel Simon aus Darmstadt
Darmstadt — D 17

TECHNISCHE
UNIVERSITÄT
DARMSTADT

FUNKTIONALE MATERIALIEN

BOSCH

Development and Assessment of Rare Earth-lean Th_1Mn_{12}-Phases for the Use in Permanent Magnets

Entwicklung und Bewertung seltenerdarmer Th_1Mn_{12}-Phasen zum Einsatz in Permanentmagneten

Genehmigte Dissertation von Daniel Simon aus Darmstadt

1. Gutachten: Prof. Dr. Oliver Gutfleisch
2. Gutachten: Prof. Dr. Helmut Ehrenberg

Tag der Einreichung: 23.04.2019
Tag der Prüfung: 08.07.2019

Darmstadt — D 17

Bitte zitieren Sie dieses Dokument als:
URN: urn:nbn:de:tuda-tuprints-89644
URL: http://tuprints.ulb.tu-darmstadt.de/8964

Erklärung zur Dissertation

Hiermit versichere ich, die vorliegende Dissertation ohne Hilfe Dritter nur mit den angegebenen Quellen und Hilfsmitteln angefertigt zu haben. Alle Stellen, die aus Quellen entnommen wurden, sind als solche kenntlich gemacht. Diese Arbeit hat in gleicher oder ähnlicher Form noch keiner Prüfungsbehörde vorgelegen.

Darmstadt, den 23.04.2019

(Daniel Simon)

’Any sufficiently advanced technology is indistinguishable from magic.’

Arthur C. Clarke, 1973

To my beloved parents.
For all our great time together.

Abstract

The first part of the work deals with the detailed investigation of ferromagnetic Th_1Mn_{12}-phases in the material systems Sm-Fe-Mo-Al and Ce-Sm-Fe-Ti-V. Different methods were employed to characterize existence ranges as well as magnetic and structural properties. Based on the obtained results, the suitability and potential of these phases for the use in future permanent magnets is discussed.
Specifically for the promising $Ce_{0.5}Sm_{0.5}Fe_{10}Ti_1V_1$(Ga)-phase, bulk magnets were successfully produced by hot-pressing and subsequent die-upsetting. The samples were characterized in detail, both, magnetically and structurally. The possibility of inducing a texture by die-upsetting was closely investigated and evaluated regarding the factors which are considered to be crucial in the case of Nd-Fe-B-magnets.

In the second part, Kerr microscopy was performed on a set of very different and well-reported permanent-magnetic phases. The magnetic patterns, visualized by polarized light microscopy, were evaluated quantitatively with image processing software and further compared to the respective intrinsic magnetic properties. The potential to quantify the magnetic properties of new ferromagnetic phases based on their domain contrast is assessed. There is a certain compositional sensitivity and the suitability to quickly check for uniaxial anisotropy or substantial polarization. However, quantification remains problematic because the influence of the local chemistry and physics (especially the reduced magnetizations) on the sample surface, regarding the rotation of the polarization plane, is obscure and furthermore overlain by measurement uncertainties.

Zusammenfassung

Im ersten Teil der Arbeit wurden die ferromagnetischen Th_1Mn_{12}-Phasen der Materialsysteme Sm-Fe-Mo-Al und Ce-Sm-Fe-Ti-V untersucht. Verschiedene Methoden wurden für die Bestimmung von Existenzbereichen sowie magnetischer und struktureller Eigenschaften eingesetzt. Auf Basis der Ergebnisse wird die Eignung dieser Phasen für die Verwendung in zukünftigen Permanentmagneten diskutiert.
Speziell für die vielversprechende $Ce_{0.5}Sm_{0.5}Fe_{10}Ti_1V_1$(Ga)-Phase konnten erfolgreich Bulkmagnete mittels Heißpressens und anschließenden -umformens hergestellt werden. Diese wurden sowohl magnetisch als auch strukturell eingehend charakterisiert. Die Möglichkeit zur Texturierung beim Umformen wurde genau untersucht und hinsichtlich der Faktoren, die für Nd-Fe-B-Magnete als entscheidend angenommen werden, bewertet.

Im zweiten Teil wurde ein Ensemble stark unterschiedlicher und verlässlich dokumentierter permanentmagnetischer Phasen mittels Kerr-Mikroskopie untersucht. Mittels polarisierter Lichtmikroskopie wurden die magnetischen Strukturen sichtbargemacht und unter Verwendung von Bildbearbeitungsprogrammen, für den weiteren Vergleich zu den entsprechenden intrinsischen magnetischen Eigenschaften, quantifiziert. Die Abschätzbarkeit der magnetischen Kennwerte neuer ferromagnetischer Phasen anhand deren Domänenkontraste wird beurteilt. Es existiert eine gewisse Sensitivität hinsichtlich Phasenzusammensetzungen und die Möglichkeit einachsige Anisotropie und beträchtliche Polarisation schnell zu erkennen. Quantitative Abschätzungen bleiben jedoch wegen unzureichender Kenntnis über den Einfluss der lokalen Chemie und Physik (besonders der reduzierten Magnetisierungen) auf die Rotation der Polarisationsebene problematisch. Weiterhin ist dieser Einfluss von Messunsicherheiten überlagert.

Contents

List of Figures

List of Tables

Abbreviations and Symbols

Abbreviations

At.%	Atomic percent
BSE	Back-scattered electrons
DFT	Density functional theory
DSC	Differential scanning calorimetry
DTA	Differential thermal analysis
DU	Die-upset
EBSD	Electron back-scatter diffraction
EDX	Energy-dispersive X-ray spectroscopy
FIB	Focused ion beam
GBDP	Grain boundary diffusion process
HDDR	Hydrogen disproportionation desorption recombination
HP	Hot-pressed
HRE	Heavy rare earth(s)
IAC	Ion adsorption clay(s)
ICP-OES	Inductively coupled plasma optical emission spectrometry
LRE	Light rare earth(s)
ND	Neutron diffraction
PLM	Polarized light microscopy
PPMS	Physical Properties Measurement System
PSM	Permanent magnet synchronous machine(s)
px	Pixels
RE	Rare earth(s)
REO	Rare earth oxide(s)
SEM	Scanning electron microscopy
SPD	Singular point detection
TG	Thermogravimetry
TKD	Transmission Kikuchi diffraction
TM	Transition metal
VSM	Vibrating sample magnetometer
Wt.%	Weight percent
X	Further element
XRD	X-ray diffraction

Symbols

α, β	Temperature coefficients of remanent flux density and coercive field strength
α_K, α_Ψ	Microstructure parameters
α_s	Analyzer angle
γ	Specific domain wall energy
δ	Domain wall width
δ_{cd}	Width of closure domains
ϵ	Dielectric permittivity
$\boldsymbol{\epsilon}$	Dielectric permittivity tensor
ϵ_0	Dielectric permittivity of vacuum
ζ, υ, ξ	Angles describing a particle in a magnetic field (Stoner-Wohlfarth)
η	Dimensionless energy (Stoner-Wohlfarth)
θ (Theta)	Angle between incident X-rays and crystallite's lattice plane(s)
ϑ	Angle between magnetization and c-axis
κ	Damping coefficient
λ	X-ray wavelength
μ_0	Magnetic permeability of vacuum
μ_B	Bohr magneton (magnetic moment of an electron)
ρ	Density
ρ_{XRD}	Theoretical density calculated from XRD-refinement
τ_i ($\overline{\tau_i}$)	Angle between macroscopic magnetization and local easy axis (average)
φ	Deformation degree
$\dot{\varphi}$	Deformation rate
χ	Magnetic susceptibility
ω	Angular frequency

$\mathbf{a}$, $\mathbf{b}$, $\mathbf{c}$	Lattice parameters of the a-, b- and c-axis
$\hat{\mathrm{a}}$, $\hat{\mathrm{c}}$	Magnetically hard- and easy axis of a particle (Stoner-Wohlfarth)
$\mathrm{c}_{\mathrm{light}}$	Speed of light
d_{sd}	Single domain particle size
$\mathbf{e}$	Charge of an electron
$\mathbf{f}$	Restoring coefficient
i	Countable index (universal)
$\mathbf{i}$	Imaginary unit
$\mathbf{m}$	Vector with reduced magnetizations
m_1, m_2, m_3	Reduced magnetizations
m_{e}	Mass of an electron
n	Number of the root
$\mathbf{r}$	Position of electron(s)
$\mathbf{t}$	Time
x	Stoichiometry index (universal)

A	Exchange constant
A_0	Reflected regular light component after analyzer
A_K	Kerr component/ amplitude after analyzer
B	Magnetic flux density
B_r	Remanent flux density
$(BH)_{max}$	Maximum energy product
$(BH)_{max,theo}$	Theoretical maximum energy product
C	Domain contrast
C_{11}, C_{22}, C_{33}	Components of the elasticity tensor (Voigt notation)
D	Dielectric displacement field
E	Electric field
$\mathbf{E}$	Energy
E_0	Amplitude of electric field
H	Magnetic field strength
H_a	Anisotropy field strength
H_c	Coercive field strength/ Coercivity
${}_BH_c$	Coercive field strength of the magnetic flux density
${}_JH_c$ $(:= H_c)$	Coercive field strength of the magnetic polarization
$H_{c,max}$	Maximum coercive field strength
H_d	Magnetic field strength of demagnetizing field
H_{ext}	Magnetic field strength of externally applied field
H_N	Magnetic field strength of nucleation field
I	Intensity of dark or bright domains
I_0	Relative background intensity
J	Magnetic polarization
$\mathbf{J}$ $(\mathbf{J_z})$	Total angular momentum quantum number (z-component)
J_r	Remanent polarization
J_s	Saturation polarization
K_1	First uniaxial anisotropy constant
K_d	Stray field energy coefficient
K_u	Uniaxial anisotropy coefficient
$\mathbf{L}$	Total orbital angular momentum quantum number
M	Magnetization
M_0	Magnetization of a particle (Stoner-Wohlfarth)
M_s	Saturation magnetization
N	Demagnetizing factor
$N_{\parallel}$, $N_{\perp}$	Demag. fac. parallel and perpendicular to magnetization (Stoner-Wohlfarth)
N_{eff}	Effective average value for the demagnetizing factor
Q	Complex Voigt constant
R_0	Reflected regular light component
R_K	Kerr component/ amplitude
RT	Room temperature
T	Temperature
T_C	Curie temperature

1 Introduction

Permanent magnets are important for the society as they are key constituents in technological devices. Especially with the promotion of energy efficient and environmentally friendly technologies, the demand for them will continue to grow [1–4].

In particular, electric motors, more precisely permanent magnet synchronous machines (PSM), use high performance magnets. These typically involve rare earth-elements (RE) and can, therefore, be responsible for up to 1/3 of the product's total costs. With required masses of up to 1.5 kg, the magnets contribute significantly to the weight of the concerned machines. Compared to induction-based principles, PSM allow weight savings what turns out to be decisive for applications associated with electromobility and the conservation of a clean environment [5]. The torque of PSM scales linearly with the magnet material's remanent polarization [6, 7]. Furthermore, operation usually involves elevated temperatures and temporally changing, opposed magnetic fields. This results in special requirements regarding these functional materials [1, 8, 9].

Since their discovery in the early 1980s, magnets based on the $Nd_2Fe_{14}B_1$-phase have become an unrivaled choice for high-performance applications. They finally replaced Sm-Co-magnets, suffering from the Co-crisis at that time [10, 11]. Nd-Fe-B-magnets are still being enhanced by targeted variations of the composition and employed elements as well as process optimizations [1, 2]. The demand for scarce RE like Dy and Tb, in order to meet today's demands for high coercive field strengths and Curie temperatures (but lowering saturation polarization), has recently become critical [2]. By the end of 2010, China's monopoly position with respect to the provision of RE and actual magnets has, thus, resulted in the RE-crisis. As a result, approaches like the grain boundary diffusion process were developed and the use of mischmetal was tested [11, 12]. The controlled usage of Dy and Tb as well as continuous improvements of recycling strategies, pronounce the importance of element-strategic considerations.

An interesting option, besides pushing the extrinsic properties of Nd-Fe-B further to their limits, is the development of alternative compromise ('plugging-the-gap' [13]) phases with maximum energy products potentially in the range of $100\,\mathrm{kJ/m^3}$–$200\,\mathrm{kJ/m^3}$. Potential extensions to the existing phase portfolio could be intermediates between ferrites and Nd-Fe-B regarding a cost/performance-ratio [10, 13]. Any approach to promote the rating of reported phases by the lowering of costs, resource issues and potential economical vulnerabilities is constructive as well.

There is a persistent interest in RE-Fe-rich intermetallics (mainly RE-lean) to be used as permanent-magnetic phases [2, 14, 15]. From the stated point of view, permanent magnet research has changed from a search for the revolutionary magnet towards the evolution of apparently well-established phases. Additions of elements like Co, Ga, Al, Ti, V, Cu, further RE and others have already shown to be suitable for the improvement of intrinsic properties or to provoke favorable secondary phases [16–20]. Gradual dependencies are expected within the respective stability ranges. These can occasionally be determined by using available phase diagrams [21–23]. Despite the fact that there are, by calculation, already thousands of suitable alloys for ternary systems, the development is likewise believed to lead towards multi-element systems. Of central interest are phases with the Th_1Mn_{12}-structure where Th-sites are occupied by RE [15, 17, 18, 21, 24–32]. Naturally, a favorably low demand of the latter can be expected. Particularly for Ce, the supply is excellent and expected to improve further [33, 34]. It is remarkable that so far little has been reported on the extrinsic properties of those phases. If so, these usually originate from rapid solidification experiments and coercivities are low compared to what would be expected based on the intrinsic values. Nevertheless, nanocrystallinity is a desirable property and a useful concept. Not only because of the concept of exchange-coupled magnets but also because advantageous properties are justified for fine microstructures [16]. It should be kept in mind that, eventually, these extrinsically attainable properties are decisive for applications.

Besides the possibility of lucky hits, an efficient search strategy needs to be established. Though the tailoring of compositions is rather unrestricted, manufacturing processes should allow a transferability to existing infrastructure. Fast screening methods like reaction sintering or reaction crucible approaches can be considered to easily form several, potentially quite stable, phases of a given system [35, 36]. Subsequently, these are recommended to be analyzed by Kerr microscopy for rapid assessments. The exhibited domain patterns are supposed to provide information on intrinsic characteristics [37–40].

Aim of the present work is the detailed investigation of different ferromagnetic Th_1Mn_{12}-phases in order to judge their suitability as new candidates in the assortment of typically used permanent magnets. The considered material systems are Sm-Fe-Mo-Al and Ce-Sm-Fe-Ti-V from which so far only ternary bounding systems have been analyzed [41–43].
First, focus is set on the ongoing substitution of Al for Fe in $Sm_1Fe_{10}Mo_2$. The prototype phase is more or less consistently charted in literature [44–46]. As dopant element, Al has previously shown to be beneficial for the magnetic properties [47–51]. Comprehensive studies are performed since corresponding influences are hard to predict.
Further, emphasis is on the V-doping of $Ce_{1-x}Sm_xFe_{11}Ti_1$. Here, x is an universal stoichiometry index. $Ce_1Fe_{11}Ti_1$, with potential as a desirable, low-cost permanent magnet, is unambiguously reported to lack sufficiently high coercive field strength while the V-substitution in $Sm_1Fe_{11}Ti_1$, as exceptional 1:12-phase, was found to significantly improve the latter [17,28,46]. It is desired to map the evolution of magnetic properties for the $Ce_{1-x}Sm_xFe_{11}Ti_1$- and $Ce_{1-x}Sm_xFe_{10}Ti_1V_1$-series to possibly find a trade-off material. Because of the superiority of bulk permanent magnets, the properties of this trade-off material shall also be transferred to a relevant product.

For each multi-component system, Fe-rich compositions are analyzed in order to elucidate equilibrium phases and their solubility ranges. The influence of individual substitutions is discussed. Corresponding results allow for the production of single phase samples (negligible amount of neighboring phases) whose structure is then analyzed by diffraction experiments to determine relevant lengthscales and preferential occupations of crystallographic sites by the dopant atoms. Characteristic magnetic values are measured and tracked as a function of composition. The development of coercivity is analyzed on intensively milled powders, annealed for different conditions, and the complementary material from melt-spinning experiments. Finally, a bulk magnet from hot-pressed ribbon material is characterized in detail and further subjected to die-upsetting at different rates in order to induce a texture.
Separately, the employed variety of characterization techniques is completed by Kerr microscopy. The potential to easily estimate the potential of magnetic phases, is tested and discussed. It is tried to provide a final statement on the significance of domain patterns to quantitatively derive intrinsic magnetic properties from them.

2 Fundamentals

The following section provides the necessary basics in order retrace the performed experiments and follow the evaluation of their corresponding results later on.

First, the established properties of ferromagnetic materials are explained. Despite different processing routes, structure/property-relationships and typically involved elements, the considered Th_1Mn_{12}-phases are introduced. Finally the magneto-optical Kerr effect is presented. In the respective contexts, fundamental references are indicated and further reading is presented.

2.1 Ferromagnetic materials

The introduction to the basic phenomena is presented based on relevant textbooks to which it is referred to for further details [52–54].

The term ferromagnetism refers to the property of materials to maintain a magnetization M after the removal of a magnetizing field H. Ferromagnets provide a stray field in their exterior as long as they are not demagnetized by an opposed field, mechanic work or exposure to a temperature T that exceeds their very distinct Curie temperature T_C. Macroscopic characteristics of a magnet evolve from the magnetization states of single grains and are determined by the magnetic phases and the micro- or nanostructure, respectively.

In the non-magnetized state, the magnet's grains are generally separated into domains whose arrangement causes a macroscopic absence of magnetic flux. Domains are volume partitions of equally orientated magnetic moments that are separated by domain walls mediating magnetization reversals by a rotation of spins. This rotation involves moments lying completely in the plane (Bloch wall, bulk material) or partially pointing out of the plane of the domain wall (Néel wall, thin films). Abrupt changes of magnetization are in conflict with the exchange interaction striving for parallel alignments. Equilibrium arrangements are a compromise regarding energy terms from stray fields and the existence of domain walls. In general, the magnet's exterior is less conductive for magnetic flux so that closed field lines in the interior are preferred.

Hysteresis

Figure 2.1 shows the dependence of the magnetic polarization $J = \mu_0 \cdot M$ for an initially non-magnetized permanent magnet as a function of an externally applied field strength H_{ext}. Here, μ_0 stands for the magnetic permeability of vacuum. In the beginning, the macroscopic polarization of the material is zero. As H_{ext} is raised, the magnetization describes the so-called initial magnetization curve which is characterized by the field-dependent susceptibility $\chi = M/H_{ext}$. Towards the saturation polarization J_s (saturation magnetization M_s), domain walls move so that preferably orientated domains grow. High field strengths can slightly rotate the magnetization direction of misoriented grains away from the local crystal axes in order to achieve saturation. Withdrawing H_{ext} causes a reduction of J_s to the remanent polarization J_r. Reason for the occurrence of remanence in ferromagnets is the exchange interaction. The application of a reversed H_{ext} consecutively reduces the polarization from J_r back to zero, yielding the demagnetization curve which is generally desired to exhibit a good rectangularity. The latter means the preservation of high J for maximum opposing fields until a steep decrease sets in. The required H_{ext}, to completely repress a previous polarization, is called coercive field strength (or coercivity) ${}_{J}H_c$ and will throughout this work be written as H_c. Further opposed fields finally cause saturation in the opposed direction from which on the described characteristics repeat, yielding the hysteresis graph (hysteresis loop). Its width $(= 2 \cdot H_c)$ allows to differentiate permanent magnets (high H_c,) from soft-magnets (low H_c).

The plot on the right in Figure 2.1 shows a measurement of J over T. For the limiting case $H_{ext} \rightarrow 0$, the Curie temperature can be determined.

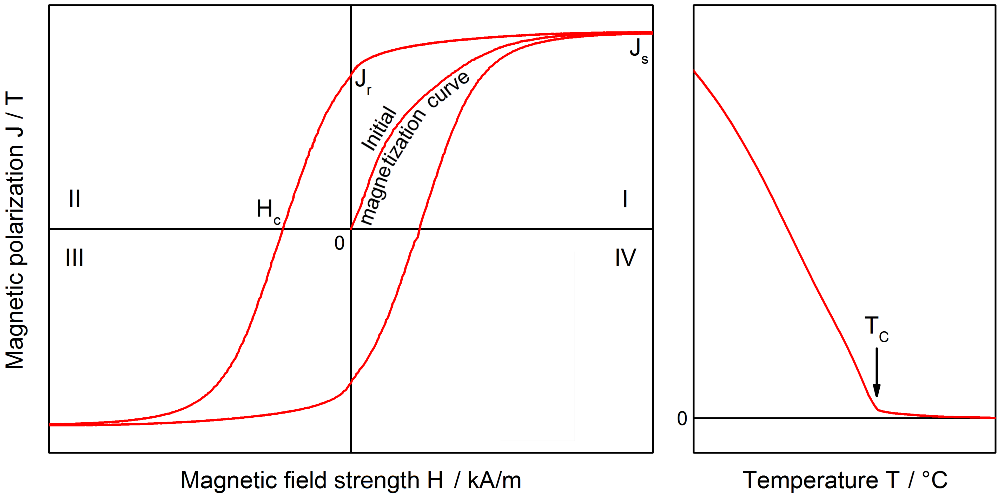

Figure 2.1: Hysteresis loop J(H) for a typical, nucleation-controlled permanent magnet (left) and the identification of its T_C from a J(T)-measurement (right). All decisive quantities are indicated.

Plotting the flux density $B = \mu_0 \cdot (H + M)$, rather than J, yields a similar hysteresis loop whose saturated branches have a slope of μ_0. It shall be noted that B vanishes at ${}_{B}H_c$ usually being lower than ${}_{J}H_c$. By analogy with J_r, B_r designates the remanent flux density. The plot B(H) is especially useful to determine the maximum energy product $(BH)_{max}$ as a measure for the maximum stored energy in the magnet (potential energy of oriented moments). It is the largest product of B and H corresponding geometrically to the area of the largest rectangle under the curve in the second quadrant. Theoretical maximum values can be estimated by Equation 2.1. Approximations for actual energy products can be conducted by replacing J_s for J_r.

$$(BH)_{max,theo} = \frac{J_s^2}{4 \cdot \mu_0}. \tag{2.1}$$

Aligned magnetic dipoles generate the magnet's poles where field lines emerge (north) and enter (south) to establish the solenoidal magnetic stray field. However, simultaneously a counter directed field tends to demagnetize the material and reduces the actual magnetic field in its interior. The demagnetizing field $H_d = -N \cdot M$ is proportional and oppositely directed to M and depends on the shape of the magnet which is accounted for by the demagnetizing factor N. Measuring the magnetic characteristics in an open magnetic circuit (e.g. vibrating sample- or pulsed field magnetometer) requires appropriate corrections.

Highest $(BH)_{max}$ are obtained for shapes yielding a demagnetizing factor of $N = \frac{1}{2}$ (cylinder with height ≈ radius) what results by differentiating a merged expression of $B = \mu_0 \cdot (H + M)$ and

$H_d = -N \cdot M$. If the demagnetization curve has an ideal square shape, $(BH)_{max} = (BH)_{max,theo}$ applies. The load line, defined by Equation 2.2, plays an important role for the definition of suitable shapes. It can be plotted in the second quadrant of the B(H)-hysteresis loop where it defines the working- or operation point depending on its slope and the loop shape (intersection). The working point needs to be in the region where B decreases rather constantly and reversed domains are not yet explicitly nucleated.

$$\frac{B}{-\mu_0 \cdot H} = \frac{1-N}{N}. \tag{2.2}$$

Anisotropy

Substantial coercive field strengths require considerable anisotropy which in return can have several origins. Fundamental for the analyzed phases, the following remarks are especially made with respect to tetragonal crystals. However, they remain largely valid beyond these.

In RE-magnets and ferrites, the by far largest contribution to anisotropy originates from magnetocrystalline anisotropy. This means the preferential alignment of J with local crystallographic directions giving rise to easy- and hard magnetization axes. Typically, permanent magnets show strong uniaxial anisotropy which means that one axis (usually called c-axis) is exceptional and easiest to be magnetized. Magnetocrystalline anisotropy depends only on the lattice and the atoms occupying the different sites. It originates from spin orbit coupling in a crystal electric field and the reciprocal interplay of magnetic dipoles. Universal with respect to the underlying crystal structure, it can in its easiest form be approximated by Equation 2.3.

$$\Delta \mathbf{E} \approx K_1 \cdot \sin^2(\vartheta). \tag{2.3}$$

Here, ΔE stands for the energy difference, K_1 for the first uniaxial anisotropy constant and ϑ for the angle between magnetization and c-axis. In case of RE-magnets, the quantity K_1 has especially large values so that further terms with additional constants can be neglected at room temperature (RT). However, depending on the crystal geometry, the signs of the latter determine different kinds of observable anisotropies. The field strength where saturation of a hard direction can be achieved is designated as anisotropy field strength H_a. Equation 2.4 shows how H_a can be calculated from the quantities K_1 and J_s.

$$H_a = 2 \cdot K_1 / J_s. \tag{2.4}$$

Shape anisotropy is a further effect that can be responsible for preferential magnetization directions. It originates from the dependence of demagnetizing fields on the magnet's physical shape. For instance, AlNiCo-magnets are characterized by special nanostructures with elongated precipitate particles, formed during spinodal decomposition [55, 56]. Extreme examples are ferromagnetic films where magnetization is preferably situated in-plane due to the low conductivity of magnetic flux in air.

Induced anisotropy is a last and typically less important contribution.

Classification of magnetic properties

Previous considerations associated with the hysteresis loop emphasize the importance of T_C, J_s, J_r, H_c and $(BH)_{max}$. While the first two quantities are only dependent on the magnetic phase and therefore called intrinsic, the remaining ones depend sensitively on the realized processing steps and the resulting microstructure (extrinsic). In theory, the alignment of individual grains in the microstructure allows to double J_r with the result that $(BH)_{max}$ quadruples (see Equation 2.1). Dependent on the particle- and grain size this can, in principle, be achieved by sintering or die-upsetting.

The intrinsic counterpart of the extrinsic quantity H_c is H_a. The latter defines the upper limit for H_c. Due to local magnetic softening, practical values often reach only 25 % to 30 % of H_a (Brown's paradox [57, 58]). However, a high H_a usually implies the potential for high H_c [10].

2.1.1 Processing permanent magnets

In order to make use of the inherent magnetic properties of an individual phase, it is important to control the microstructure. Thus, high performance magnets are the result of sophisticated processing that transfers intrinsic properties to the highest extent to extrinsic ones [8,13,59,60]. Generally, very different approaches have emerged within the last few decades which involve especially the production of particles in the micrometer range, the rapid solidification of melts and the annealing of mechanically amorphized powders [61–66]. Depending on the processing and resultant particle size, a single material can be suited for different operation fields. The major routes for the industrial production of anisotropic bulk magnets are presented in the following with a focus on the superior system Nd-Fe-B for which considerations and necessary prerequisites are especially true.

Sinter process

The principle is to fix an ensemble of previously aligned, single crystalline particles with an average size of 1 μm to 10 μm which is well above their single domain particle size ($d_{sd} \approx 0.3\,\mu$m) [67, 68]. It is the traditional processing technique which starts with the production of a Nd-Fe-B-alloy that typically has a slightly overstoichiometric Nd-content [69, 70]. The subsequently annealed ingot is subjected to a hydrogen decrepitation process that favorably splits the $Nd_2Fe_{14}B_1$-grains along their grain boundaries. Constantly handled under protective atmosphere, these single crystalline particles are jet-milled for a further, mechanically gentle refinement. Aligned by a magnetic field during the green body formation (uniaxial or isostatic pressing), the textured ensemble will then be sintered at temperatures around 1000 °C. The partial melting of $Nd_2Fe_{14}B_1$-grains at their exterior and the presence of a liquid (melts roughly at 670 °C) Nd-rich secondary phase, forming as a result of the overstoichiometric composition allow for liquid phase sintering and the formation of magnets with high densities [67, 71]. After a subsequent annealing, the Nd-rich phase finally covers the grains and magnetically decouples them. It constitutes a negligible volume fraction and can be extremely thin. The

fine microstructure and the decoupling phase are essential to obtain substantial hard-magnetic properties.
Reducing the Nd-surplus in the alloy and therefore the amount of grain boundary phase, the respective absolute J_r can be raised. However, the responsible coupling effects (stray field and exchange) among the grains, reduce H_c [5]. Stray fields are especially critical as the grains deviate from an ideal ellipsoid shape while exchange is limited to short lengthscales. Just like H_c, the hysteresis loop can significantly be tailored by the microstructure of the magnet. For instance, the demagnetization curve determines whether $(BH)_{max,theo}$ (see Equation 2.1) can be achieved. That is the case if $\mu_0 \cdot H_c > J_r/2$ holds true and the hysteresis is rectangular up to $H_{ext} = H_c$. With τ_i as angle between the macroscopic easy direction and the easy axis of an individual grain (counted by the universal index i), the expression $J_r/J_s = \cos(\overline{\tau_i})$ allows to judge the degree of texture from the average value $\overline{\tau_i}$ and, thus, whether a present magnet is iso- or anisotropic [72, 73].

In general, grains are progressively refined to make the bulk material less vulnerable to local, statistical defects which lead to a magnetization reversal [68]. The sintering of nanocrystalline particles (≤100 nm), without detrimental oxidation, can currently not be realized [74].

Hot-pressing and die-upsetting

This approach mainly starts from melt-spun ribbons that are nanocrystalline or permit to form this state by adequate heat treatments. Intensively milled powder or material from a previous hydrogen disproportionation desorption recombination (HDDR) step can also be utilized [1, 61, 75].

Powdered ribbons can also be used for the production of polymer-bonded magnets where especially their nanocrystallinity is advantageous. Due to their isotropic nature (arbitrary crystallization directions), corresponding magnets allow the realization of fine and complicated shapes. Multi-pole magnetization is possible and the magnets are usually well-protected from corrosion. This underlines the significance of their voluminous manufacturing [61, 76, 77].
Instead of mixing ribbons with polymers, densification to a bulk material can be achieved by hot-pressing. This is usually done at nominal temperatures above the melting point of the Nd-rich phase providing a density ρ close to the theoretical value [78, 79]. As a main difference to sintering, the process is pressure-assisted to favor a fast densification. Embedded in a paramagnetic matrix phase, the grains are not significantly larger than in the as-spun state and permit, thus, larger H_c than sintered magnets. The more stoichiometric the alloy, the larger are exchange coupling effects with respect to the much weaker far-reaching stray fields. The isotropic character explains why the hot-pressed compounds with non-interacting particles have low J_r. If they do interact, strong exchange effects can occasionally compete with the grains' magnetocrystalline anisotropy so that the favored magnetization direction of an individual grain is not necessarily parallel to its easy axis. As a consequence, J_r is raised over $J_s/2$ (remanence enhancement) and the whole hysteresis loop is altered [80].

The major disadvantage of low J_r is faced by a subsequent texturing step. As discussed later, this texturing is neither trivial nor universal. Suitable for the production of anisotropic nanocrystalline magnets are techniques like die-upsetting (low cylinders) or backward extrusion (radially oriented rings with frequently inherent inhomogeneity) [63,75,81]. Maximally textured, crack-free products are obtained if die-upsetting involves a liquid phase and the die diameter is not larger than the final magnet (compressive stresses on free surface) [78, 82]. Usually, temperatures are similar to those for hot-pressing (≥700 °C) allowing for high material transport and particle mobility within the hot-pressed precursor. A collective c-axis alignment parallel to the deformation direction is attained by plastic flow involving grain rotations as well as anisotropic growth. Common process parameters are the degree of deformation φ and the associated rate $\dot{\varphi}$, whereas tool geometries can affect the outcome just like temperature regulation does [82]. The deformation degree can be calculated as natural logarithm of the initial cylinder height divided by its final value. Even for successfully textured samples the reduced polarizations stay a characteristic disadvantage compared to sintered magnets. Advantageous, on the other hand, is the better temperature- and corrosion stability [77, 83].

Die-upset Nd-Fe-B-magnets

As stated before, magnets based on the showcase phase $Nd_2Fe_{14}B_1$ support die-upsetting as a process to significantly induce texture. This is possible because of multiple peculiarities that are described in more detail to understand necessary requirements.

Though microstructural mechanisms during hot-pressing are complex, it has been found that texturing is possible for process temperatures below the melting point of the Nd-rich phase [78]. Responsible are rotations and the gliding of grains with respect to neighboring ones. The Nd-rich phase acts as a solid lubricant. Since this eutectic phase is low-melting it further permits maximally textured, crack-free products if temperatures are chosen suitably. Among different proposed concepts it could further be shown that a solution precipitation creep mechanism is active during the deformation [84–88]. Creep describes a continuous deformation of a material occurring for stresses lower than the respective yield strength. At temperatures above the melting point of the grain boundary phase, the chemical potential for species in the liquid phase and on the crystallite surface is different causing atoms to constantly dissolve and precipitate again at energetically more favorable sites. This principle can be transferred to explain the growth of preferentially orientated grains in die-upset magnets. The thermally activated diffusional creep occurs jointly with the stated rotation and gliding effects.

Additionally, the tetragonal $Nd_2Fe_{14}B_1$-unit cell possesses anisotropic elastic properties for applications of uniaxial pressure [85, 89]. The elastically softest axis (c-axis) aligns parallel to the axis of largest stress. Experiments on single crystals have shown that the in-plane growth (a-axes) also occurs much faster so that as a consequence the growth in the basal plane is promoted and grains with the easy c-axis parallel to the pressure will consume others, resulting in the typical formation of platelet-shaped grains [84].

A favorable temperature for the deformation of Nd-Fe-B can be quantified to 800 °C and the strain rate is generally set to $0.01\,\mathrm{s}^{-1}$–$0.1\,\mathrm{s}^{-1}$ [78, 82, 90]. Increasing strains lead to a decrease of H_c by 300 kA/m or more, partially being restorable. The texturing benefit of J_r saturates for $\varphi \approx 0.8$ where values are substantially increased with respect to the initial, isotropic state. Best compositions, process parameters and tool designs are still hard to tell. Especially for new phases and material systems the transfer of processing knowledge is not straight forward.

2.1.2 Magnetic reversal mechanisms

There are different mechanisms which control magnetization reversals and are therefore decisive for the evolved H_c. Two major magnetization mechanisms are nucleation and pinning.

Nucleation

This mechanism is typical for Nd-Fe-B-sintered magnets with grain sizes of a few micrometers and present when domains can easily propagate through the grain interior without being considerably hindered by defects. If the grain is saturated, the nucleation field H_N (theoretically equal to H_a) for a reversed domain limits the energy effort for magnetization reversal [90]. Besides the magnetic decoupling (more grain boundary phase) and heat treatments (healing of grain surfaces and defects), grain refinement is suitable for magnetic hardening [90, 91]. Here, the lower size limit is defined by the beginning of the single domain regime. Equation 2.5 gives an approximation for the single domain particle size with A standing for the exchange constant [21, 92]. For single domain particles, the coercivity starts to decrease with further refinement and becomes zero as the superparamagnetic limit is reached [52, 54, 79]. At this threshold the remanence vanishes, too.

$$d_{sd} \approx \frac{9 \cdot \sqrt{A \cdot K_1}}{\mu_0 \cdot M_s^2}. \tag{2.5}$$

Pinning

Precipitation hardened Sm-Co-magnets are an example for materials in which the domain wall movement within the grains is hindered energetically. Local defects effectuate an energy contribution, proportional to the domain wall width, that detain the domain walls against H_{ext} [93]. Distinctive is furthermore the size of the defect.

The initial magnetization curve (see Figure 2.1) can give important hints concerning the dominant mechanism within a material. Magnetization from an (e.g. thermally) demagnetized state features the evolution from multiple domains per grain (zero net-magnetization) towards one which is characterized by the energetically favorable growth of domains that are parallel to H_{ext}. Nucleation-controlled magnets have a high initial susceptibility and saturate at fields considerably lower than H_c [93]. Finally the grains are supposed to be free of domain walls. For pinning magnets the magnetization can only be achieved for $H_{ext} \approx H_c$. The detained domain walls require high driving forces what relates H_c to the energy for unpinning [94, 95].
As contemplated before, there is no clarity regarding reversal mechanisms as the nanocrystalline regime is approached [62]. Here, distinctive features blur and it is referred to fine particle processes instead. So it is important to note that for hot-pressed magnets with single domain particles, it is not conducive to differentiate between the established magnetization processes based on the recorded initial magnetization curves.

2.1.3 Influence of the microstructure

The explicit microstructure of a magnet strongly determines its magnetic behavior. The grains are in general not uniform, may have sharp edges, lattice defects or incorporate impurity atoms [16, 96–99]. Locally increased stray fields reduce J_r and especially H_c. From experiments it could be derived that the coercive field strength of a permanent magnet can be described by Equation 2.6, independent of the way it was produced [16]. Phenomenologically, actual (bulk) K_1-values are about ten times larger than those describing the reduction in the grain boundary. The anisotropy scattering largely determines extrinsic properties and the shape of the hysteresis loop [16]. The microstructure parameters α_K and α_Ψ (=0.5) account for deviations of H_a, the present magnetization mechanism and misorientation effects, respectively.

$$H_c = \alpha_K \cdot \alpha_\Psi \frac{2 \cdot K_1}{J_s} - N_{eff} \cdot M_s. \tag{2.6}$$

N_{eff} is the effective average value for the demagnetizing factor. Approximating it by $N_{eff} = N_{\|} - N_{\perp}$, with $N_{\|}$ and $N_{\perp}$ as demagnetizing factors of parallel and perpendicular to M_0 (see Figure 2.2), and simplifying with $\alpha_K \cdot \alpha_\Psi = 1$, Equation 2.6 reproduces the Stoner-Wohlfarth model [100]. The latter assumes that the most unfavorable grains initiate demagnetization during magnetization reversal. This results in further remagnetization events due to exchange- and stray field coupling of grains. These cascades can actually be observed by Kerr microscopy [101] (see Section 2.4).

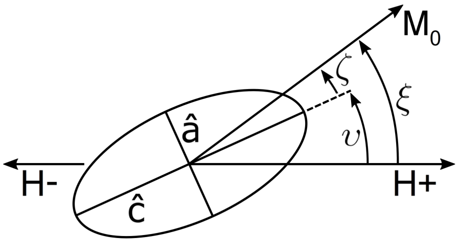

Figure 2.2: Sketch of a Stoner-Wohlfarth particle. After [100].

Stoner and Wohlfarth shed light on the magnetization of single domain ferromagnets with uniaxial magnetocrystalline anisotropy. They assume ideally oriented non-interacting, ellipsoidal particles. Figure 2.2 depicts the geometric arrangement and introduces the angles ζ, ξ and υ to describe the relation between easy ĉ-axis of the particle and the experienced field H+/H-. Focus is on the resultant normalized dimensionless energy η which follows per particle with magnetization M_0 and can be expressed by Equation 2.7.

$$\eta = -\frac{1}{4} \cdot \cos(2 \cdot \zeta) - \frac{H}{M_0 \cdot (N_{\perp} - N_{\|})} \cos(\xi). \tag{2.7}$$

The average over magnetization vectors M_0 gives the response of an isotropic ensemble. The sum field H, experienced by the particle, follows from the orientation of all other particles in the vicinity. An ensemble with isotropic distribution of easy axes yields $J_r \leq 0.5 \cdot J_s$.

The theoretical treatment of particles below 50 nm requires consideration of exchange coupling. Relevant lengthscales are comparable to the domain wall thickness δ being the largest range where ordered spin alignments can be mediated. Larger particles are only influenced in their outer shell where significant deviations of the magnetization direction from corresponding easy axes occur. Magnetization reversal at low H_{ext} is facilitated, reversibility for even lower fields is attained and J_r is increased.

2.1.4 Exchange spring magnets

Coupling in very fine-grained materials leads to the concept of exchange spring magnets. Fundamental feature of these hybrid nanocomposite magnets is the coupling of a soft- (e.g. α-Fe) with a hard-magnetic phase, reducing the volume fraction of the latter [102]. With the individual strengths of both, exchange spring magnets potentially exhibit high saturation polarization, elevated resistance to irreversible magnetization reversal and improved resistance against oxidation [102, 103]. Proper control of the nanostructure is required since ferromagnetic secondary phases are classically discussed to be detrimental [16, 91]. Though first proposed in 1991, it is likely that actual representatives were achieved unawarely before. The fact that two very different magnet materials with distinct characteristics behave as one, blurs their differentiability. It is important to keep in mind that all nanomagnets, with a soft-magnetic phase neighboring a hard-magnetic one, can be considered as composites.

For magnetic exchange, the involved phases need to be crystallographically coherent and dispersed on lengthscales which are comparable to the domain wall thickness. Since the soft-magnetic particles are coupled three-dimensionally, their maximum size should not exceed $2 \cdot \delta$. Favorable is a matrix structure of α-Fe (high J_s) with fine and equally occurring hard-magnetic particles distributed within. The size of the Fe-network is especially given by its Néel wall thickness of 11.4 nm [80]. The resulting composite material is characterized by moderate $(BH)_{max}$ and a reversible demagnetization curve. The texture-independent reversibility justifies the designation of the material class based on mechanical springs. The alignment of moments in the soft-magnetic phase with easy axes of the hard-magnetic phase is stable against external deflections which grains in the latter component can withstand. Magnetization reversal happens at lower field strengths than the coercivity of the hard-magnetic phase would suggest.

Production routes involve surfactant-assisted ball milling, quenching of melts, multilayer films, mixed-powder consolidation and the reduction of oxides [79, 102–105]. The actual formation occurs by homogeneous precipitation, or the transformation of certain precursors previously introduced into a matrix. A famous example is the nanocomposite $Fe_3B_1/Nd_2Fe_{14}B_1$ which is usually produced by strip casting [106]. Both phases form from metastable, Nd-containing $Fe_{23}B_6$ when crystallized from an amorphous initial state. The solubility for a significant amount of voluminous Nd-atoms is a special prerequisite in this case.
The presented principle has nowadays been commercialized [3]. However, so far it has not been possible to realize a bulk magnet with the corresponding characteristics.

2.2 Rare earth-elements

The 15 lanthanide elements (& Sc and Y) are referred to as rare earth-elements. The term traces back to the discoveries and relates to occurrences in oxide minerals [107]. The elements are characterized by distinct properties which are related to the consecutive filling of the 4f-shell. As a consequence, the atoms shrink more than it would be expected (lanthanide contraction). The close vicinity of consecutively inserted electrons to the atomic nucleus causes the non-affected outer shell to exhibit a similar chemistry throughout the series [21, 107, 108]. Obeying Hund's rules, orbitals start to be occupied twice for the second half of rare earths giving rise to a further subdivision into the light- (LRE) and heavy rare earths (HRE). Apart from their chemical similarity, the RE do all have unique physical properties.

2.2.1 Raw material and political issues

With their individual properties, the RE contribute to important functionalities and technologies of the modern high tech society. Recently, their uniqueness has made them indispensable in specific products and applications. These include electric components in smartphones and computers, lighting and cooling technologies, aerospace and mobility concepts as well as catalysis [2, 33, 107, 109]. Additionally, they play a significant role in the generation of regenerative energy which helps to power mankind in a sustainable way. For example they are involved in solar cells and as permanent magnets in generators of all fields.

The designation of all these elements to be rare is actually misleading. Their average abundance in the earth's upper continental crust is comparable to more common metals like Co, W, Mo, Cd and Cu [107, 108]. As representative of the HRE (in general more infrequent occurring than LRE), Dy is found twice as much as Au. The RE occur widely distributed on the planet, but they appear in low concentrations and never as isolated species. The individual RE, therefore, need to be concentrated by processes like floatation or gravimetric- and electrostatic processes. Most common sources for LRE-retrieval are the minerals bastnaesite and monazite while ion adsorption clays (IAC) are especially rich in HRE. Being home to more than 11 million people, cities like Baotou and Ganzhou are economically specialized on the production of LRE and HRE, respectively. IAC are predominantly obtained in the south of China.
Figure 2.3 presents typical mixtures of the individual representatives in the stated materials. Lately, mining was predominantly motivated by the demand of Nd(Pr) (didymium), Dy and Tb for the fabrication of Nd-Fe-B-magnets with reasonable high temperature (≥150 °C) characteristics [11, 67]. Nowadays, HRE-contents of 3 wt.%–10 wt.% contribute most to their final prices. The preferential interest on specific RE has led to vast excess of more frequent representatives. Major locations of commercially available RE-metals are China (Inner Mongolia), Mount Weld in Australia, and the Mountain Pass in the USA [107]. Economically extractable world reserves are estimated to approximately 130 Mt REO with more than 40 % in China [110]. From 2013 to 2017, the annual world production amounted roughly 120 kt REO while the demand is estimated to grow by circa 10 %/year which might not be supported without any problems. All of the given numbers are somewhat blurred by illegal mining.

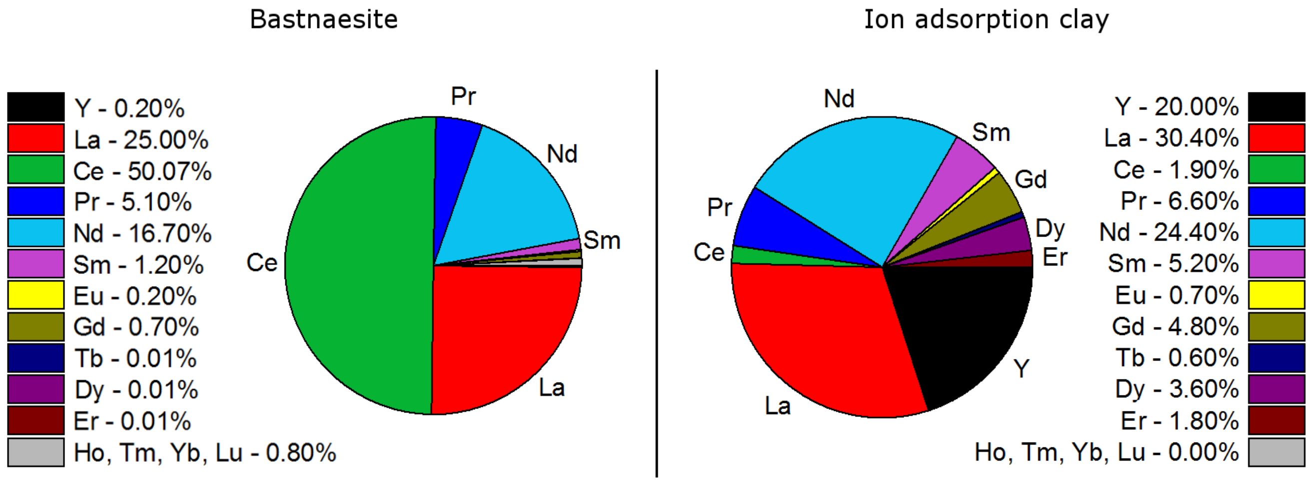

Figure 2.3: Mixtures of different RE as mined from bastnaesite (left) or ion adsorption clays (right), respectively. Bastnaesite is said to deliver mainly LRE while the infrequent IAC yield larger concentrations of HRE. After [111].

The facts from above result in diverse and far-reaching problems that are hereinafter referred to as manyfold RE-criticality. The hardly modernized exploitation of RE has extensive consequences on the environment. To release RE-ions, all ores require concentrated acids, bases and a lot of energy in the form of heat. The disposal of toxic as well as radioactive (enrichment of Th- and U-oxides) waste in landfills is a burden [107].

The largest country to mine and concentrate RE is China. It particularly generates value from the separation and refining within its national borders. The European Union imports more than 90 % of its demands from the People's Republic what results in a strong dependency that has impressively manifested as RE-crisis in 2011 [112]. As a result of export restrictions, prices increased tenfold especially affecting HRE. Consequently, recycling approaches gain an outstanding role. These are, however, subjected to problems due to the mixed employment of RE in tiny amounts. Where possible, substitution is another way to reduce dependencies. In the field of permanent magnets it is worth to elaborate this potential for the establishment of a sustainable development.

2.2.2 Distinct role in permanent magnets

Reason for the particular relevance of RE-permanent magnets is their RE-sublattice providing strong magnetocrystalline anisotropy [11,21]. The electrons in 4f-orbitals have a higher energy than those in 6s-states. However, they are spatially closer to the atomic core so that the 4f-electrons determine the magnetic characteristics by their angular momenta without altering the chemical behavior [108]. Just like the incapability of magnetostatic interactions to explain the high anisotropy of RE-TM-magnets, this screening results in a weak impact of the crystal electric field on the RE. The anisotropy energy per RE-atom without exchange coupling is equivalent to a temperature of about 4 K [11]. Without a coupling of RE- and TM-sublattices no anisotropy would be present at typical operating temperatures.

The anisotropy originates from the interplay of spin orbit coupling and the crystal field, i.e. the motion of the electrons in real space interacting with local charges of the lattice [10, 113, 114]. Thus, the magnetic structure of TM-dominated RE-Fe- or RE-Co-compounds arises from the magnetic moments and magnetocrystalline anisotropy of 3d- and 4f-sublattices as well as relevant interactions between them. Interactions among 3d-spins are strong and lead to a collective sublattice which can be described by mean values for moment and magnetocrystalline anisotropy. These interactions account for the exchange field (related to the molecular field) which acts on the RE-moment. This explains the exchange interactions between unpaired spins of RE- and 3d-magnetic moments. The intra-atomic exchange of the TM-sublattice predominantly defines the resultant Curie temperature, whereas the indirect exchange of 3d-4f-sublattices contributes only to a small extent. The latter, however, stabilizes the anisotropy brought in by the RE against thermal effects [10, 21]. Interactions among 4f-spins are small since the considered RE-Fe- or RE-Co-compounds possess only little amounts of RE. Their indirect exchange can therefore be neglected. Depending on the balance of competing RE- and TM-sublattice anisotropies, spin reorientation transitions can occur for certain temperatures.

In RE-TM-X-phases, LRE and HRE behave differently, thus justifying their distinction. For example in $Nd_2Fe_{14}B_1$ the moments of LRE couple parallel to the TM-moments while for HRE they couple antiparallel causing lower J_s. Therefore, the choice for specific alloys requires always far-reaching considerations and detailed experience.

2.2.3 Peculiarities of Ce and Sm

From previous considerations it is clear that Ce is an abundant RE, for which there are currently no extensive applications. The use of Sm is restricted to special applications like Sm-Co-magnets for high temperature applications or as neutron absorber in reactors [107]. Since its demand can be satisfied by the actual mining output, the apparent disposability is a snap-shot in time. Considering the abundance in Figure 2.3, it can be seen that a sustainable supply for voluminous production quantities is just as difficult as in the case of Dy or Gd.

With regard to physical characteristics, it turns out that the melting temperature of Sm (1075 °C) is about 300 °C higher than for Ce [108]. Its boiling point, however, is more than 1500 °C less which causes a high vapor pressure and certain difficulties when alloyed in liquid state [115]. As a result of the lanthanide contraction, Sm has a smaller diameter and higher density than Ce. Chemically, Ce is a curiosity among the RE because it exceptionally occurs with a 4^+-oxidation state which differs from the typical RE^{3+}-ions. In its neutral state it carries not only one 4f- but also one 5d-electron.

As one of the first three ions in the LRE-series, Ce has an axially compressed electron distribution of 4f-orbitals. For Sm, as part of the last three, it is axially elongated [116]. This form of the electron density depends on the z-component of the total angular momentum quantum number $\mathbf{J}_z$. Similarities of early/ late LRE with corresponding HRE originate from the fact that states with large total orbital angular momentum $\mathbf{L}$ and mostly planar probability densities are occupied first (Hund's rules). The Sm^{3+}-ion has an exceptional crystal field contribution to the **J**=7/2-multiplet being especially significant for anisotropy contributions of higher order. This is explained by the so-called **J**-mixing which commits to these excited states causing a spin structure that deviates from an one-dimensional nature [117]. That results for example in the substantially high uniaxial anisotropy of the ferromagnetic $Sm_1Fe_{11}Ti_1$-phase.

2.3 Th_1Mn_{12}-phases

The Fe-rich RE-TM-X-phases with 1:12-stoichiometry (1:12-phases) are promising candidates to be used as permanent magnets [15, 18, 25, 27–32, 118]. Their crystal structure is well-documented and due to their prospects, multiple representatives have been investigated already systematically for different RE. The limited number of bulk magnet studies concerning these phases is also presented and rated.

2.3.1 Structure and ferromagnetic properties

Crystallizing in space group number 139, the decoration of atoms in space is completely described by the expression I4/mmm. This spatial arrangement is often referred to as Th_1Mn_{12}-structure. The body-centered structure has a four-fold rotary axis and three simple mirror planes, each perpendicular to one of the crystallographic axes. Obeying this geometric constraint, 26 atoms (twice the elemental formula) are distributed on the tetragonal lattice whose dimensions are given by **a**, **b**(=**a**) and **c**. Due to the fact that one axis is extraordinary, tetragonal crystal systems (just like hexagonal or orthorhombic ones) meet the necessary prerequisite for permanent magnet applications. Sufficient condition is the (at least prevalent) coincidence of the easy magnetization direction with that extraordinary axis (positive anisotropy). For example, Sm_2Fe_{17} (rhombohedral) has an easy-plane anisotropy and cannot be used as a permanent magnet [113, 119].

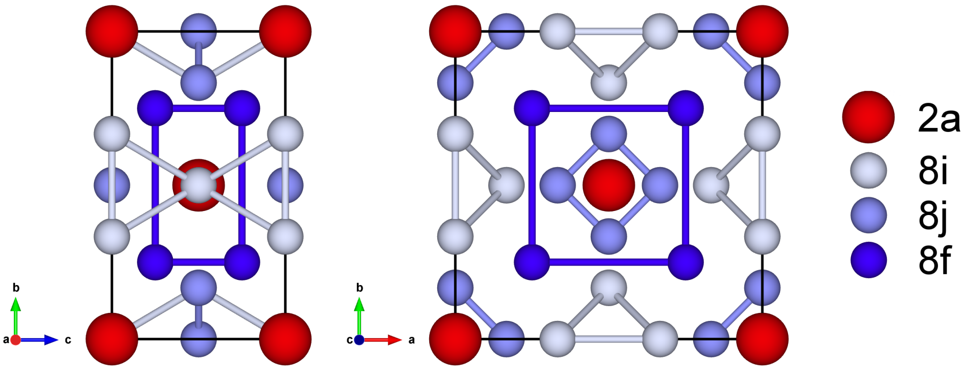

Figure 2.4: Geometry and different crystallographic sites of the Th_1Mn_{12}-crystal structure.

As shown schematically in Figure 2.4, phases with Th_1Mn_{12}-structure offer four non-equivalent crystallographic sites, denoted as 2a, 8i, 8j and 8f, characterizing the respective local geometry of each site. Atoms, situated on those, have different numbers of distinguishable nearest neighbors. For example, there are 1x2a, 5x8i, 4x8j and 4x8f neighbors for an atom on 8i-site. The 2a-site appears twice (8·1/8 + 1) per unit cell. Each of the three non-equivalent sites appears eight times. In RE – Fe-phases, the 2a-site is occupied by the large RE-atom while the remaining ones are filled with Fe.

Instead of forming binary Th_1Mn_{12}-intermetallics, the phases generally require stabilization by a third element X, substituting for Fe. From experiments it is known that $RE_1Fe_{12-x}X_x$-phases mostly occur for X=Mo, Al, Ti, V, Cr, Si or W [23, 26, 120–125]. Depending on X, limited stoichiometries are possible and often two or four Fe-atoms are substituted per unit cell. Lattice constants usually increase with raised X-content. Larger radii of RE result in an a-axis stretching while the c-axis is weakly strained. Ce, Eu and Yb show anomalies which might originate from mixed valence states [108, 126].
Based on the individual distances and coordination numbers, Fe-atoms on 8i-sites turn out to carry the largest moment ($\approx 2.0 \cdot \mu_B$) contributing to the overall magnetization [127, 128]. Here, μ_B designates the Bohr magneton (magnetic moment of an electron). Furthermore, the orbital moment of Fe on 8i predominantly induces anisotropy.

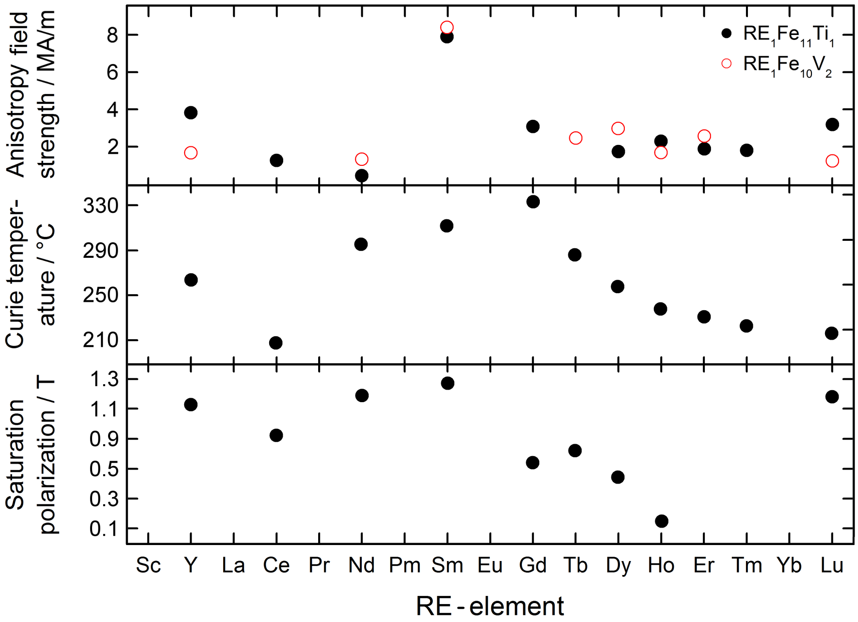

Figure 2.5: Intrinsic magnetic properties of the $RE_1Fe_{11}Ti_1$-series (partially also $RE_1Fe_{10}V_2$) as a function of the RE-element [129–142].

Figure 2.5 presents the intrinsic properties of $RE_1Fe_{11}Ti_1$-phases based on literature reports. In addition, anisotropy fields of the structurally related $RE_1Fe_{10}V_2$ are presented as a function of the considered RE. Matching previous considerations, the Sm-based representatives possess best-in-class properties and constitute a favorable choice. Their elevated anisotropy (large and positive K_1) benefits from the described 4f-electron distribution of Sm in the Th_1Mn_{12}-lattice where neighboring atoms are suggested to carry negative charges [11, 21]. The axially elongated 4f-orbital preferably points out of the (001)-plane to minimize electrostatic interactions. Furthermore, it stands out that Ce-based phases have a comparatively poor performance.

Like in other RE-Fe-X-series, $Gd_1Fe_{11}Ti_1$ has the highest T_C and is closely followed by $Sm_1Fe_{11}Ti_1$. For Gd the 4f-shell is half-filled, which is why it carries the largest spin-moment. This greatly affects the exchange energy which further supports ferromagnetism [11, 120, 143–145]. The ferromagnetic (ferrimagnetic) coupling for LRE (HRE) with Fe traces back to the differently pronounced 3d-4f-exchange interactions. Together with the dominant Fe-anisotropy for T > 25 °C, this explains the presented, systematic development of T_C.

2.3.2 Magnets from Th_1Mn_{12}-phases

Actual magnets from Th_1Mn_{12}-phases are rarely treated in the existing literature. The term occurs mainly in the context of powdered samples (mechanically alloyed) or ribbons (melt-spun), rather referring to the realized magnetic response of the processed phase instead of a bulk demonstrator magnet based on it. Common are reports on the magnetic properties for specific production parameters, treatments or new elemental compositions. Focus is on the obtainable coercivities, saturation- and remanent polarizations as well as structural aspects and stability ranges [26, 60, 146–149].

Despite provisional bonded magnets that allow for the respective measurements, only a few publications applied established methods for the fabrication of real bulk magnets [17, 150, 151]. In general, little information is available on experiments concerning (anisotropic) bulk 1:12-magnets [29]. Due to the special importance of these considerations, the powder metallurgical production of Sm-Fe-Ti- and Sm-Fe-Ti-V-sintered magnets stands out [17]. However, the coercivities reached in these magnets are reported to be considerably below these of melt-spun ribbons with equal compositions. Absolute values of the samples without (with) V are decreased from 445 kA/m (780 kA/m) to 65 kA/m (160 kA/m). The reduction is attributed to changes in the microstructure - from fine 1:12-grains in the ribbons to not well defined ones in the sintered samples - where V exhibits a positive effect, though. The achieved grain structure in the sintered magnets was not well-defined and contained multiple phases. The 1:12-grains had a size of 8 μm to 15 μm.
Similarly lowered H_c-values have also been found for sintered pendants of $U_1Fe_{12-x}Si_x$ [151].

The impracticality of Sm-Fe-Ti-X-systems regarding the sintering of 1:12-phases is especially explained by the absence of an equilibrium with a liquid phase around 1000 °C. Problematic is also the neighboring α-Fe as well as the evaporation of Sm, precluding even higher sintering temperatures [17, 29, 152].
Apart from classical sintering, there is also spark plasma sintering of $Sm_1Fe_{12-x}Ti_x$ reported [150]. This process is known to preserve the properties of nanocrystalline materials on macroscopic scales and suppress considerable grain growth. Yet, spark plasma sintering is not common for the contemporary production of permanent magnets.

2.4 Magneto-optical Kerr effect

Discovered in the year 1877 by John Kerr, the magneto-optical Kerr effect describes the change of intensity and the rotation of the polarization plane of linearly polarized light being reflected (transmission = Faraday effect) from magnetized metal surfaces [153]. This requires non-zero net-magnetization which can, for example, originate from the material being ferromagnetic or be caused by applying a magnetic field to a paramagnetic material. The information depth of this technique is very low and can be quantified to roughly 30 nm [154–156].

In principle, there are three main configurations which are presented in Figure 2.6. The polar-, longitudinal- and transverse Kerr effect differ by the incidence of light with respect to the magnetization direction. They might also appear simultaneously. The symbols R_0 and R_k stand for the reflected regular component of the light and the Kerr component/ amplitude, respectively.

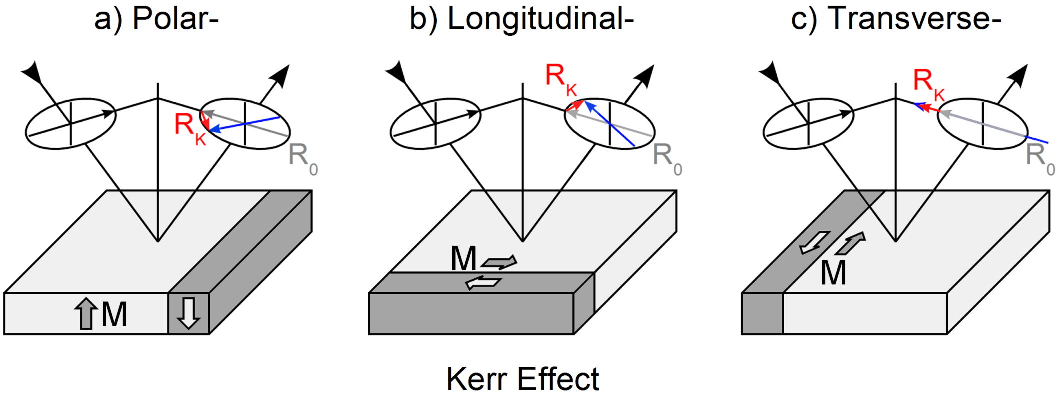

Figure 2.6: Geometry of the polar- (left), longitudinal- (center) and transverse (right) magneto-optical Kerr effect. The different types vary by the incident direction of light with respect to the magnetization direction of the material. After [154].

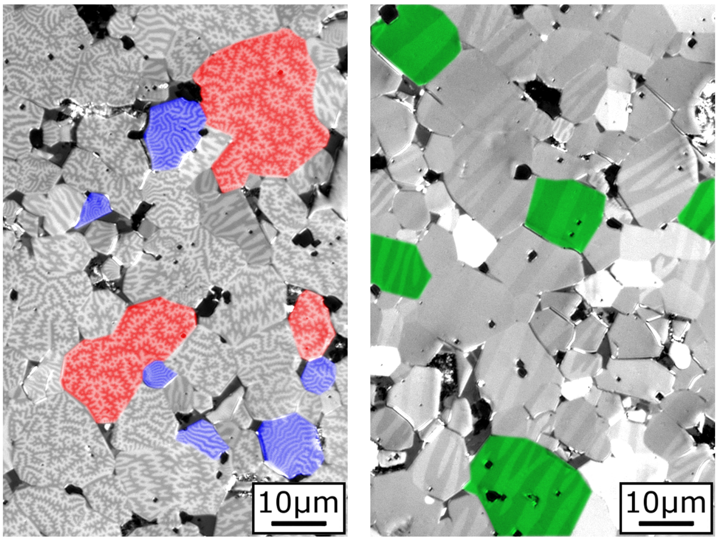

Figure 2.7: Different domain arrangements in a Nd-Fe-B-sintered magnet. Parallel to the macroscopic easy direction (left), the grains show star- (red) or maze-like (blue) closure domains. For grains with in-plane easy axes (right), characteristic stripe domains (green) occur.

Polarized light microscopy allows certain statements on the three-dimensional constitution of cross-sectional grains in prepared microsections. Due to stray field minimization, the domains form specific arrangements. The exposed patterns of individual grains are characteristic for their crystallographic orientation. Figure 2.7 shows examples which are common for RE-magnets (Nd-Fe-B).
Closure domains indicate that the particles' easy axes point out of the plane. Rather broad stripe domains have predominantly in-plane easy axes [101, 154, 155]. Furthermore, closure domains can be subdivided into star- and maze-like patterns which evolve depending on the residual thickness of the respective grain [157].

2.4.1 Physical model and mathematical description

Reflection on metallic surfaces happens as a consequence of the substantial number of non-localized conduction electrons. This special bonding condition, where electrons can easily be excited and moved, causes their shiny appearance and explains the good conduction of electricity and heat [158]. Linearly polarized light has an oscillating electric field component $E = E_0 \cdot \exp(\mathbf{i} \cdot \omega \cdot \mathbf{t})$ which causes electrons in the material to move parallel to its polarization plane (damped harmonic oscillator with resonances corresponding to state transitions). Here, E_0 is the amplitude of the electric field, ω the angular frequency, $\mathbf{i}$ the imaginary unit and $\mathbf{t}$ the time. In return, the received energy is radiated away. The regularly reflected light possesses the same polarization plane as prior to the interaction with the surface. In agreement with Huygens' principle, sufficiently flat surfaces enable expelled wavefronts to form a reflected ray which fulfills the reflection condition [158].

If the material has a magnetization M, the oscillating electrons at position $\mathbf{r}$ with charge $\mathbf{e}$ and mass m_e are further subjected to the Lorentz force giving rise to R_K which is usually small [154]. The implementation of this force into the equation of motion leads to Equation 2.8. The factors κ and $\mathbf{f}$ are the damping- and restoring coefficient while $c_{light} = 1/\sqrt{\epsilon_0 \cdot \mu_0}$ denotes the speed of light. The latter appears in the equation because the electrons oscillate with speeds near c_{light}, which is why the relativistic form of the Lorentz force needs to be used.

$$m_e \cdot \frac{d^2\mathbf{r}}{d\mathbf{t}^2} + \kappa \cdot \frac{d\mathbf{r}}{d\mathbf{t}} + \mathbf{f} \cdot \mathbf{r} = \mathbf{e} \cdot E_0 \cdot \exp(\mathbf{i} \cdot \omega \cdot \mathbf{t}) + \mathbf{e} \cdot \frac{d\mathbf{r}}{d\mathbf{t}} / c_{light} \times M. \tag{2.8}$$

As shown in Figure 2.6, the rotation of the polarization plane results from the superposition of R_0 with R_K. The rotation is proportional to the magnetization component in direction of the reflected light. Decisive are the reduced magnetizations m_i in the anisotropic dielectric permittivity tensor ϵ (here: cubic crystal). The vector $\mathbf{m}$ comprises the reduced magnetizations. This dielectric permittivity tensor determines the dielectric displacement field D which corresponds to the vector of the reflected light and is expressed by Equation 2.9. The material-dependent, complex Voigt constant Q causes an anisotropic permittivity of the material. Situated off-diagonal in ϵ, Q eventually alters the speed of light in the material. These different velocities cause a phase difference and therefore a rotation of the polarization/ oscillation plane. Here, K_u stands for the uniaxial anisotropy coefficient, K_d is the stray field energy coefficient and ϵ designates the dielectric permittivity. By analogy with μ_0, ϵ_0 is the dielectric permittivity of vacuum.

$$D = \boldsymbol{\epsilon} \cdot E = \epsilon \cdot E + \mathbf{i} \cdot \epsilon \cdot Q \cdot \mathbf{m} \times E \tag{2.9}$$

$$\text{with} \qquad \boldsymbol{\epsilon} = \epsilon \begin{pmatrix} 1 & -\mathbf{i} \cdot Q \cdot m_3 & \mathbf{i} \cdot Q \cdot m_2 \\ \mathbf{i} \cdot Q \cdot m_3 & 1 & -\mathbf{i} \cdot Q \cdot m_1 \\ -\mathbf{i} \cdot Q \cdot m_2 & \mathbf{i} \cdot Q \cdot m_1 & 1 \end{pmatrix} \qquad \text{and} \qquad Q = \frac{K_u}{K_d} = \frac{2 \cdot K_u}{\mu_0 \cdot M_s^2}.$$

Among the Kerr effects presented in Figure 2.6, the polar one is most pronounced. Thus, it represents the most common choice for Kerr microscopy. For this geometry, the plane of oscillation rotates and the previously linearly polarized light changes to elliptical after reflection. The effect is strongest when the light falls in perpendicular to the surface. As a first approximation, it is independent of the polarization direction of the light.

2.4.2 Intrinsic properties from domain patterns

The direct dependence of the rotation of the polarization plane on the sample magnetization suggests the estimation of intrinsic magnetic properties from Kerr microscopy. Literature states that from the contrast C (i.e. the mean grey value difference) of Kerr-images it is possible to determine saturation polarization, anisotropy constant and Curie temperature, both qualitatively and quantitatively [37–40]. Quantification is proposed to arise from comparisons with well-reported reference samples or the measurement of domain contrast over temperature for a $Nd_2Fe_{14}B_1$-standard. Motivation is Equation 2.10 which can be obtained by refining textbook approaches [40, 154]. It states that the observable contrast - as difference between the intensities $I_i = {A_0}^2 \cdot \sin^2(\alpha_s \pm A_K/A_0) + I_0$ of dark and bright domains - is linearly dependent on A_K. Here, A_K and A_0 designate R_K and R_0 after the analyzer while I_0 is the relative background intensity and α_s the analyzer angle. Thus, the linear dependence of C on M_s or J_s (typically present within a domain) is concluded.

$$C = 2 \cdot \sin(2 \cdot \alpha_s) \cdot A_K \cdot A_0. \tag{2.10}$$

Merging expressions for the specific domain wall energy $\gamma = 4 \cdot \sqrt{A \cdot K_u}$ [154] with a model for the width of closure domains $\delta_{cd} \propto \gamma/{J_s}^2$ in sufficiently large grains and assuming $K_u \approx K_1$, it is possible to obtain Equation 2.11 [159]. The exchange constant A has typical values of approximately 50 pJ/m. The anisotropy field strength follows from Equation 2.4.

$$K_1 \propto {\delta_{cd}}^2 \cdot {J_s}^4. \tag{2.11}$$

In contrast, the optical determination of T_C is trivial and requires the tracking of the contrast with temperature. The value of interest results from appropriate extrapolation and is characterized by a vanishing domain pattern.

3 Experimental Methods and Analysis

This section presents the sample preparation in detail and summarizes the experimental approaches for the determination of decisive characteristics and active mechanisms. In addition, all facilities and measuring devices are specified to allow for the complete repeatability of the obtained results.
In general, the samples contain RE which are known to be especially sensitive to oxidation. The employment of activated powders with high surface-to-volume ratios particularly raises the likelihood of degradation. The samples are therefore stored and handled in an Ar-glovebox with O_2- and water levels below 0.1 ppm. For heat treatments, they are encapsulated in quartz-tubes without ever allowing the contact to the surrounding atmosphere during the transfer.

3.1 Sample preparation

3.1.1 Alloy production

The samples were molten in a custom-built arc-melting furnace allowing to process small quantities of up to 20 g. With respect to their specific weight, pure elements (purity, metals basis: Ce 99.9 %, Sm 99.99 %, Fe 99.98 %, Mo 99.95 %, Al 99.95 %, Ti 99.99 %, V 99.7 %, Ga 99.9999 %) are placed in pits of a Cu-plate. In some cases, suitably chosen pre-alloys (required elements excluding the RE) were molten, polished and cut prior to the actual formation of the desired alloy in a following step. The Cu-plate forms the anode and is water-cooled from below. The cathode ends with a truncated W-tip and can be moved during melting. The potential difference is provided by a welding generator allowing for electric arcs whose currents are able to rapidly generate temperatures sufficiently high to melt all elements of the periodic table. The process chamber was threefold evacuated and flushed with Ar to establish an appropriate atmosphere. Residual O_2 reacts with supplementary Ti-pieces which are molten prior to the actual sample. The operating atmosphere pressure was set to 0.6 bar of Ar-gas. This is low enough to avoid overpressures as a consequence of evaporating species and the heating of the chamber-gas. At the same time it is preferably high to suppress the promoted evaporation of involved elements due to high vapor pressures. In this context, Sm is especially problematic because much of it leaves the alloy after repeated melting steps and is therefore provided with an initial surplus of about 25 %. Melts of Sm-alloys are furthermore highly viscous so that these were remelted six times and turned after each single step.
Homogenization and formation of equilibrium phases was done by annealing the arc-melted ingot in evacuated quartz-tubes at 1000 °C for 72 h with subsequent quenching in water.

3.1.2 Fast screening methods

For comparison of the annealed samples regarding information on the underlying phase diagram and the confirmation of potentially occurring equilibrium phases, two fast screening techniques were applied. These are reaction sintering and the reaction crucible method.

Reaction sintering means the reaction of powder particles in random stoichiometries which can be established by the mixing and consolidation of the individual element powders (metals basis: Sm 500 μm/99.9 %, Al 25 μm/99 %, Fe 60 μm/99 %, Mo 5 μm/99.9 %). In case of Mo, the particles were particular small to allow for large contact areas that may lead to diffusion since its melting point (2623 °C) is quite high. The mixtures were compacted using a toggle press and then wrapped in Ta-bags which were encapsulated in evacuated quartz-tubes. The reaction was allowed to occur for different times in a furnace followed by quenching.

Table 3.1: Light element contamination of the single element powders used for reaction sintering.

Powder	C / wt.%	O / wt.%	N / wt.%
Sm	0.012	0.434	0.061
Fe	0.061	0.701	0.049
Al	0.035	1.296	0.169
Mo	0.010	0.842	0.140

Table 3.1 characterizes the powders regarding their detrimental impurities. Despite partially notable O-contents, the powders have proven to be suitable for the experiments. The RE is protected by the particles' low surface-to-volume ratio. The quantification of light elements is described later.

The reaction crucible method means the filling of small bulk pieces of pure elements into a crucible. Since Fe is the main component of the phases of interest, the systems remaining elements were given into a common Fe-crucible which was closed airtight by a lid under Ar-atmosphere. Encapsulated in quartz, the crucible was then annealed upright at 1000 °C for 72 h. Depending on the local stoichiometry, different phases were allowed to form for subsequent analyses.

3.1.3 Melt-spinning

In contrast to bulk samples, material in the fine-grained state is suitable for the assessment of H_c-values. Nanocrystallinity plays a special role because corresponding material is particularly fine-grained. Furthermore, it can be produced in a suitable (nano-) structure with moderate effort in terms of required infrastructure (unlike sintering).

One major technique for the fabrication of nano- or even non-crystalline material is the rapid solidification of melts. The process where liquid melt is ejected on a Cu-spinning wheel is called melt-spinning and nowadays utilized in lab- as well as industrial scales. Besides the wheel speed as very decisive process parameter, the chamber- and ejection pressure as well as the nozzle geometry and distance from the wheel play an important role. Depending on these, the utilized material and the temperature of the melt, it is possible to achieve cooling rates of up to 10^6 K/s. The solidification rate largely determines grain size and crystallinity of the final material. The faster the melt is quenched, the higher is the nucleation rate and the smaller is the resulting average grain size. In case of very high wheel speeds (equivalent to fast cooling rates) it is even possible to suppress the formation of crystallites yielding amorphous material.

The latter shows a strong tendency to crystallize for very short annealings at rather low temperatures. Control and homogeneity of the resulting properties are reported to be much better compared to the direct quenching with optimized process parameters [160]. An advantage of the melt-spinning technique is that the formation of α-Fe can be avoided by rapidly traversing the temperature window where it is stable. Depending on the alloy and especially its ductility (or fraction of α-Fe), the obtained material can either form bands or ribbon pieces with thicknesses of approximately 10 μm to 70 μm.
The production of melt-spun material in this work started from arc-melted ingots whose surface was polished to remove contamination. The process chamber of the utilized Bühler Melt-Spinner SC was likewise threefold evacuated and flushed with Ar. Wheel speeds were varied from 20 m/s to 40 m/s and samples were molten in quartz-crucibles with a nozzle diameter of 1.5 mm. The distance from the Cu-wheel was constantly set to 0.2 mm: Chamber- and ejection pressure were set to 400 mbar and 500 mbar Ar, respectively. It was ensured that ejection temperature was well above 1400 °C. This temperature was found to be sufficient for the melting of the desired compositions by means of differential thermal analysis (DTA). Direct determination of the temperature using the built-in pyrometer failed due to the evaporating black smoke. From a total starting mass of approximately 10 g, 30 % to 50 % could be retrieved as final ribbon material.

Supplied with the corresponding quantities of pure elements, larger quantities of a Ga-containing material were similarly obtained in an upscaled facility by Mr. Thomas Wittig at Fraunhofer IFAM in Dresden. The utilized alloy ingots were produced in an induction furnace with a crucible coated with BN as high temperature release agent. The ribbon material was produced at a wheel speed of 25 m/s and later on used for the bulk magnet production via hot-pressing and die-upsetting.

3.1.4 Intensive milling and annealing

Complementary to melt-spinning, intensive milling can be used for the fabrication and study of nanocrystalline materials. Due to the low obtainable quantities, long process times and especially the α-Fe-residues after annealing, this process is not industrially used. Contrary to mechanical alloying, intensive milling does not start from pure element powders but from polished and crushed alloy ingots in which the respective elements are already finely distributed. This is advantageous since especially RE-powders tend to be considerably contaminated.

Protected by the inert glovebox-atmosphere, alloy pieces with a size of roughly 1 cm and a total mass of 50 g were given into a previously cleaned and dried 500 ml steel milling vial of a Retsch PM400 planetary ball mill. An equal number (15) of big and small steel balls with diameters of 2 cm and 0.5 cm, respectively, were added establishing a ball-to-powder ratio of 10:1. Without any milling agent, the vials were closed with a clamping ring and installed in the mill. Centrifugal forces were balanced by the simultaneous processing of two powders at the same time. A total milling time of 10 h at 400 rounds/min was attained in intervals of 5 min. Milling cycles were separated by breaks of 10 min to avoid overheating. Depending on the composition, the final powders needed to be carved from the lower vial wall.

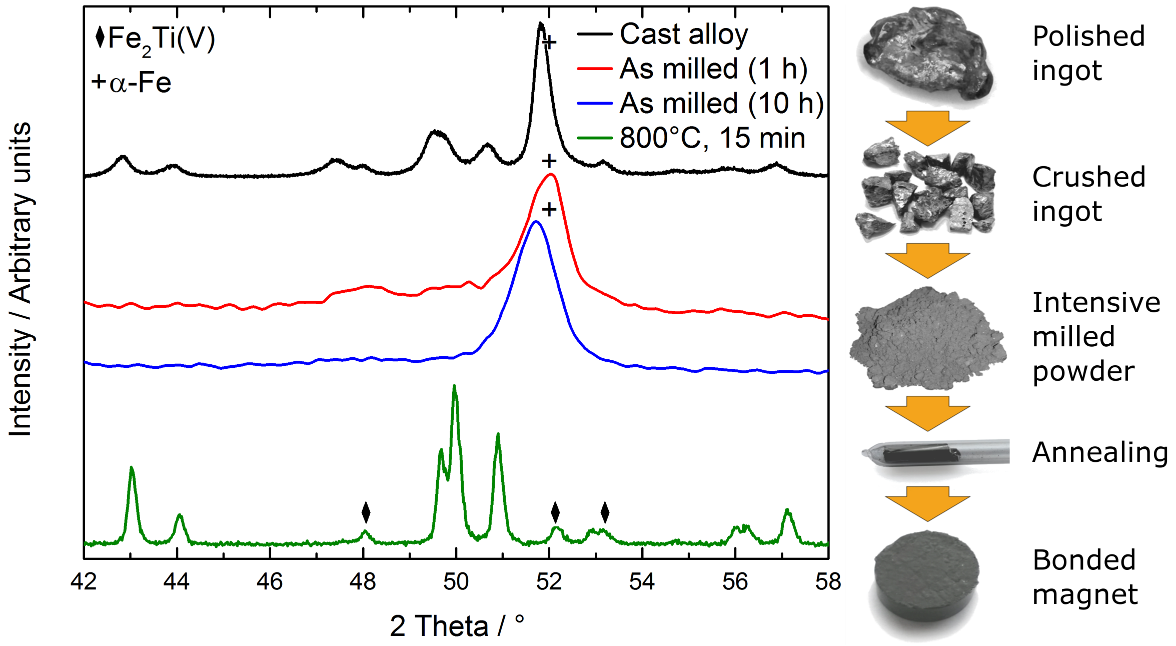

Figure 3.1: X-ray diffractograms of an exemplary $Ce_{0.5}Sm_{0.5}Fe_{10}Ti_1V_1$-alloy for different states of the processing (left). The influence of the duration of intensive milling on the structure is also presented. Corresponding pictures of an exemplary material are provided (right).

In X-ray diffractograms, the measured intensity of the diffracted radiation is plotted over 2·Theta (2θ) in degrees. This also applies to discussions on the position of reflections. Theta designates the angle between the incident X-rays and the crystallite's lattice plane(s).

Figure 3.1 shows diffractograms of an exemplary alloy for different states during the processing. Reflections of the cast material's multi-phase diffractogram (arc-melted without annealing) rapidly disappear with increasing milling time. The final state after 10 h is characterized by a broad reflection related to α-Fe. The width of the reflection indicates a very nanocrystalline state. Since Fe is the main component, the severe energy input results in the breaking of ordered phases squeezing the remaining elements in the body-centered cubic lattice (supersaturated solid solution). This becomes more pronounced with increasing milling time and causes the shift (maxima of the reflections recorded for 1 h and 10 h) of the signal due to the different lattice constants of the remaining elements.

Table 3.2: Light element contamination of a representative intensively milled $Ce_{0.5}Sm_{0.5}Fe_{10}Ti_1V_1$-powder as a function of milling time.

Milling time / h	C / wt.%	O / wt.%	N / wt.%
0 (as-milled)	0.035	0.060	0.102
1	0.036	0.304	0.128
2	0.044	0.357	0.131
5	0.039	0.402	0.145
8	0.045	0.413	0.144
10	0.044	0.445	0.143

Table 3.2 shows the representative characterization of a $Ce_{0.5}Sm_{0.5}Fe_{10}Ti_1V_1$-powder regarding light element impurities over milling time. Initial values were measured on polished bulk pieces. The O-content increases the most significantly over time while N and especially C have low and stable values. However, the absolute O-content after 10 h of milling is low enough to allow for the successful recrystallization of the 1:12-phase without much of the RE being consumed by the formation of oxides. The main reflections of Ce_1O_1 and Sm_1O_1 at angles of 35.8 °2θ and 41.6 °2θ can only be adumbrated in the diffractograms of annealed powders (see also Figure 3.1). The values in the table were obtained by carrier gas hot extraction using Leco ONH836 and CS230 devices. The compositions and RE-contents were checked by energy-dispersive X-ray spectroscopy (EDX) as well as inductively coupled plasma optical emission spectrometry (ICP-OES) using a Thermo Scientific iCAP 6300 ICP Spectrometer whose results are generally in good accordance.
All ICP-OES-measurements were performed by Ms. Bozena Siekierka in constantly close exchange with the author.

The activated state of the milled powders allows for a fast recrystallization already at rather low temperatures and time scales. The annealing was done for temperatures from 700 °C to 1000 °C for 2-30 min. Small amounts (few spatula tips) of the powders were individually sealed in quartz-tubes for the recrystallization of the hard-magnetic 1:12-phase from the supersaturated solid solutions. Wrapped in Ta-bags and at a pressure of $7 \cdot 10^{-2}$ mbar Ar, the powders are protected from the ambient atmosphere and ready for the respective heat treatments. Subsequently, the annealed powders were mixed with epoxy resin in order to facilitate the determination of H_c (bonded-powder magnet).

3.1.5 Hot-pressing and die-upsetting

Melt-spun ribbons with promising compositions were powderized by gently breaking them with low forces in a mortar. In order to transfer the properties of the nanocrystalline material to a bulk magnet, the shiny ribbon powder was hot-pressed (HP). Figure 3.2 shows a picture of the melt-spun Ce-Sm-Fe-Ti-V(Ga)-starting material as well as the geometric conditions (size of matrices) for different steps towards a die-upset magnet. The Ga-addition shall improve the processability while having only a negligible impact on the intrinsic magnetic properties of the 1:12-phase [63, 81, 161, 162].
A 500 kN press from the company Weber was used to compact approximately 3.5 g powder in an encased graphite matrix with steel punches of 8 mm in diameter. The ensemble was heated to 800 °C within 7 min under vacuum ($6 \cdot 10^{-2}$ mbar) what corresponds to a heating rate of roughly 115 °C/min. Pressing was continued for 3 min at a constant pressure of 5 kN ($\approx$ 90 MPa) achieving a size of 8 mm x 6 mm at a density of 7.51 g/cm^3 (Archimedes' principle) which is more than 98 % of the theoretical density calculated from X-ray-measurements (ρ_{XRD}=7.637 g/cm^3).

In a second step, the compacted magnets were heated again (now under Ar-atmosphere) with the same parameters to be die-upset (DU) in a steel matrix of 13.5 mm in diameter. A height reduction from 6 mm to approximately 2.4 mm specifies the degree of deformation as $\varphi = \ln(6/2.4) \approx 0.93$ which was induced maintaining mechanical integrity. Deformation rates $\dot{\varphi}$

were chosen as $0.001\,s^{-1}$, $0.002\,s^{-1}$ and $0.01\,s^{-1}$, respectively. Accordingly, the corresponding processes took 10 min, 5.5 min and 2 min.

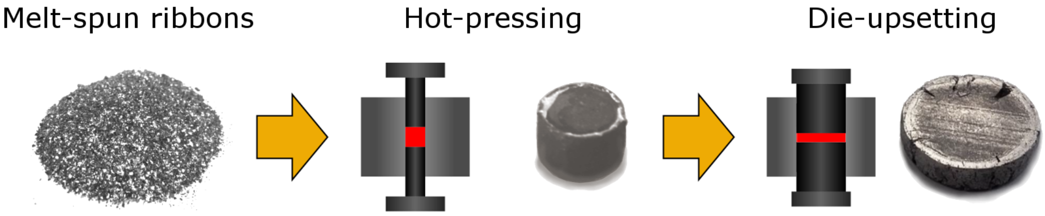

Figure 3.2: Production of hot-pressed (center) and die-upset (right) magnets from melt-spun ribbons (left). Pictures of the specimen after different steps during the process are presented.

Table 3.3 specifies the composition of the generally utilized Ga-containing material together with that of supplementary produced Ga-free one for comparison purposes regarding processability. The atomic percentages were derived from ICP-OES-analysis and indicate that the material in the lower column has an understoichiometric RE-content.

Table 3.3: Composition of the ribbon material used for hot-pressing and die-upsetting. Values are measured by ICP-OES-analysis.

Ribbon material	Ce / at.%	Sm / at.%	Fe / at.%	Ti / at.%	V / at.%	Ga / at.%
with Ga	4.14	4.28	75.28	8.15	7.64	0.51
without Ga	3.22	3.80	77.53	7.78	7.67	-

Staying constantly in a close and scientifically targeted exchange, the hot-pressing and die-upsetting were carried out by Dr. Simon Sawatzki. The actual experimental work was partially carried out in the presence of the author.

3.1.6 Density functional theory-simulation

In order to qualitatively estimate the dependence of elastic constants from the crystalline axes of $Ce_{1-x}Sm_xFe_{10}Ti_1V_1$, density functional theory (DFT)-simulations of the respective Sm-based unit cell were performed. Being experimentally hard to access, the components C_{11} ($=C_{22}$) and C_{33} of the related elasticity tensor (in Voigt notation) were extracted to discuss the outcome of the die-upsetting experiments later on and to compare the material with Nd-Fe-B in terms of processability. Furthermore, magnetic moments of the different atoms in the unit cell were determined to compare saturation polarizations of the phases with and without V.

Calculations for Sm_1Fe_{12}, $Sm_1Fe_{11}Ti_1$ and $Sm_1Fe_{10}Ti_1V_1$ comprised one unit cell with 26 atoms each. Periodic boundary conditions were set to represent a single crystalline bulk material. It had shown that the energy increases for constellations where Ti-atoms (always on 8i-sites) are far from each other. Where possible, results from diffraction analysis and limiting case calculations were applied. Based on that, Ti and V were introduced as shown in Figure A.1

(see appendix). The exact choice of crystallographic sites obeys, with second priority, the demand for satisfactory symmetry parallel to the a- and b-axis.

The calculations were performed using the Vienna Ab Initio Simulation Package [163] and their work flow management was done by the Automated Interactive Infrastructure and Database for Computational Science [164]. Electronic exchange and correlation effects were described using the Perdew-Burke-Ernzerhof parameterization of the generalized gradient approximation [165]. To model the core electrons, the Projector Augmented Wave framework was used while explicitly including the semi-core p-states of Fe, Ti and V [166]. The f-electrons of Sm^{3+} have been kept frozen in the core. Simulation results are representative for a temperature equal to absolute zero (-273.15 °C). All structures were fully relaxed including spin-polarization and after careful convergence testing for Sm_1Fe_{12}, a plane wave cutoff energy of 560 eV and a reciprocal k-point density of 160 $Å^{-3}$ have been found to be sufficient. For adequate accuracy of the elastic constants, a plane wave cutoff energy of 800 eV was used for the finite displacement method calculations, yielding the desired elasticity tensor.
After an introduction to the question and the definition of required quantities, the DFT-calculations were designed by Dr. Anika Marusczyk. The actual simulations were partially set up in the presence of the author.

3.2 Characterization

3.2.1 Electron microscopy

For microstructural investigations as well as the determination of phase compositions, samples need to be appropriately prepared. Where necessary, a Struers Accutom-50 was used for cutting and the exposure of surfaces close to the areas of interest. The samples were then embedded in epoxy resin and further processed by different grinding and polishing steps using a Struers Tegramin-30. Sandpaper with grit designations of 320, 500 and 1200 were used before polishing with diamond suspensions of 6 μm, 3 μm and 1 μm and an oxide polishing suspension of Si_1O_2. To allow for a good conductivity, the samples were finally coated with Pt/Pd or graphite, sputtered from corresponding targets.
The analysis was mainly carried out with a Zeiss Leo Supra 35 VP scanning electron microscope (SEM) in back-scattered electron mode (BSE). Generally, the acceleration voltage was set to 15 kV to excite all lines of the sample elements for quantification by energy-dispersive X-ray spectroscopy (EDX) using an Oxford Instruments INCA X-sight system at a working distance of 8.5 mm. Multiple EDX-measurements including the variation of the acceleration voltage were used to measure the global composition of samples as well as individual phases.

For electron back-scatter diffraction (EBSD) and transmission Kikuchi diffraction (TKD) a Zeiss Supra 55VP was used. The lamellas, especially used in this context, were prepared with a FEI FIB Helios NanoLab 600i focused ion beam (FIB) device. Figure 3.3 shows different moments during their production and handling. Reference data for the matching of crystalline phases from the collected data was provided from own findings.

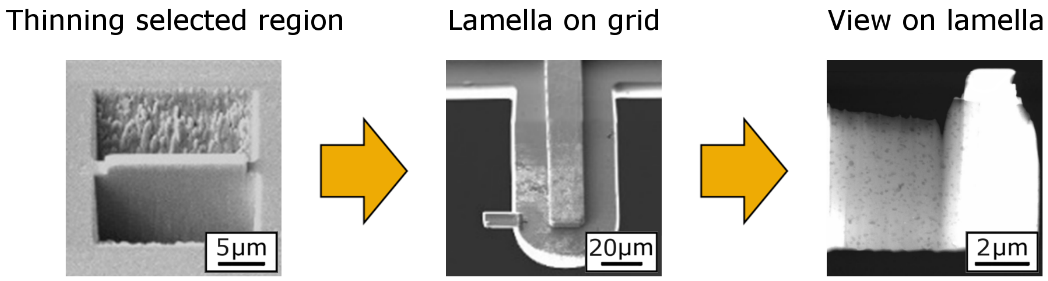

Figure 3.3: Preparation of a FIB-lamella (left), its attachment to the transfer grid (center) and an overview SEM-image on the prepared surface (right).

The lamella preparations and TKD-analyses were done by Mr. Stefan Hinderberger. The samples were selected by the author who also provided information regarding the crystal structures.

3.2.2 X-ray- and neutron diffraction

For the identification of crystalline phases, crystallite sizes (Scherrer equation and reflection profile [167]) as well as contents (wt.%) in the samples of interest, X-ray diffraction (XRD) using a Bruker D8-Advance with Bragg-Brentano geometry was carried out. It shall be noted that crystallite size is throughout understood as average dimension of coherently scattering, single crystalline partitions of the microstructure. It can be a measure of the actual grain- or particle size and does approximate it the better the smaller its value is. However, it is in general smaller or equal to the grain- or particle size. Moreover, the technique allows to determine lattice constants and therefore the theoretical density ρ_{XRD}.
The tube-material was chosen as Co (λ=1.78897 Å) because of a low portion of fluorescence radiation in the case of Fe-based samples. Here, λ is the wavelength of the X-ray radiation. An energy-dispersive Bruker Lynxeye XE 1D-detector counted the diffracted radiation, generally guided through slit apertures of 1.0 mm. The sample was constantly rotated for better statistics. The step width was set to 0.02 °2θ and the integration time was 3 s–12 s. In order to qualitatively match reflections with their responsible phases, Bruker EVA with data from the Inorganic Crystal Structure Database was used. Quantification was done via Rietveld refinement using Bruker Topas 4.2 and the fundamental parameter approach. The device parameters were determined from routine measurements on a well-known La_1B_6 standard with reflections spanning over a large angular range. This allows standardless measurements of samples with overlapping reflections and reduces the parameters for the reconstruction of the sample pattern significantly.

In order to determine occupational preferences of crystallographic sites, single phase samples with distinct compositions were prepared for analysis by X-ray- and neutron diffraction (ND). While X-rays interact with the electronic structure of atoms, neutrons interact with the atomic nuclei. The simultaneous refinement of both datasets profits from the joint information on the sample allowing to refine atom positions of four species in a physically meaningful way.
Investigated samples were $Sm_1Al_2Fe_8Mo_2$ and $Ce_1Fe_{10}Ti_1V_1$. Compositions were chosen to ensure that even strong preferences reveal the site occupations of the dopant elements Al and V. The materials were analyzed in form of annealed powders that were filled into hollow cylinders

made from the Al-alloy AlMg3. Because of the extremely high effective cross-section of Sm ($\approx$ 22 cm^{-1} [168]), Ce was preferred in case of the second material assuming that V occupies the same site for both RE and mixtures of them. Measurement was done under Ar-atmosphere, with a neutron wavelength of 1.5482(1) Å and 5 h exposure time.
In association with Prof. Dr. Helmut Ehrenberg, Neutron diffraction was performed by Dr. Anatoliy Senyshyn with the high-resolution neutron powder diffractometer SPODI at FRM II Forschungs-Neutronenquelle in Garching bei München [169].

3.2.3 Magnetic characterization

Melt-spun ribbons as well as bulk samples, including single phase material or hot-pressed and die-upset magnets, were characterized using a Quantum Design Physical Properties Measurement System (PPMS) equipped with a vibrating sample magnetometer (VSM). This setup is especially useful to record initial magnetization curves and full hysteresis loops (see also Figure 2.1). Advantage of the technique is the small sample volume and the flexibility regarding sample geometry. Disadvantageous is the open magnetic circuit which leads to distortions as a result of demagnetization effects (and need to be corrected by the factor N) as well as the usage of a superconducting magnet which requires cooling with liquid He and only allows slow ramping rates. For the conversion of units, phase densities - determined from refinements of XRD-data - were employed. Note that all PPMS-measurements were carried out at RT, for which they are therefore representative.
The application of very high fields allows to estimate saturation polarizations (high-field polarizations at 8 MA/m are used synonymously to J_s in the present work). For textured samples, the intersection of measurements parallel and perpendicular to the easy magnetization axis, determines H_a. The textured samples, as substitute for single crystals, were produced from single crystalline powder particles that were mixed with epoxy resin on the large pole faces of a massive Nd-Fe-B-permanent magnet (homogeneous field). The anisotropy field strength has also been derived by the singular point detection (SPD)-technique. This method relies on the hidden singularity in magnetization curves which can be revealed by differentiating two or more times. The singularity originates from grains whose easy axes are perpendicular to the applied field [170–172].
The actual PPMS-measurements were done by Dr. Léopold Diop. These were provided by the author who partially attended the measuring process. The textured, epoxy-bonded samples from single crystalline powder particles were produced and measured by Dr. Konstantin Skokov. For this purpose, annealed alloy pieces with high phase purities were provided by the author.

A Magnet Physik Dr. Steingroever Permagraph was supplementary used to conduct measurements in a closed magnetic circuit (N=0.0) and to extract especially values like remanence, coercivity and $(BH)_{max}$ from a standardized method (DIN IEC 60404-5) [173]. In addition, temperature coefficients have been derived by repeated measurements at different sample temperatures (equilibrated for up to 30 min). Linear relations from RT to about 110 °C are basis for the determination of the temperature coefficients α and β. Both are defined by Equation 3.1 and Equation 3.2, respectively.

$$\alpha = \frac{1}{B_r} \cdot \frac{\Delta B_r}{\Delta T} \cdot 100\,\%. \tag{3.1}$$

$$\beta = \frac{1}{H_c} \cdot \frac{\Delta H_c}{\Delta T} \cdot 100\,\%. \tag{3.2}$$

The samples had coplanar surfaces and well-defined areas. During measurement, the latter were in contact with the pole shoes of electromagnets. Concentric measuring coils around the sample recorded the flux through the sample and in the air gap in its vicinity. For bonded samples, the polarization values are undefined because the area and amount of magnetically active material is unknown. Nevertheless, coercivities of annealed powders or melt-spun ribbons could easily and reliably be determined in this way.

3.2.4 Kerr microscopy

Hard-magnetic bulk samples were analyzed by polarized light microscopy (PLM) using a Zeiss Axiophot with Epiplan Neofluar oil immersion objective (50x/1.0 Oil Pol). This allowed to obtain pictures of their respective domain patterns for subsequent evaluations. Those included qualitative changes of the domain contrast with composition and the attempt to quantify saturation polarizations based on the latter. For contrast determinations, closure domains (magnetization directed out of plane) were exclusively considered.

Besides representatives of the Th_1Mn_{12}-phases of this work, several Fe- and Co-based reference samples were produced especially for this purpose. The set of samples covers a range of $0.3\,T < J_s < 1.6\,T$.

Prior to the analysis, all samples were freshly polished in order to grant equal conditions. However, regarding possible surface tensions, different impacts are expected for different materials. Unlike SEM-samples, the surfaces were not sputter-coated with Pt/Pd. The microscope was adjusted to properly image the patterns of closure domains for the material with lowest J_s at an exposure time of 200 ms. Then all settings have remained unchanged throughout the analysis of all further samples. The uninterrupted investigation within roughly 4 h excluded external influences, possibly contributing to an altered contrast, to the highest possible extent. Relevant contributions might be the lamp temperature (light spectrum), indirect daylight and the room temperature.

Figure 3.4 presents the analysis procedure for the determination of a quantified contrast from an exemplary domain pattern. Using graphics software, the respective grey values of pixels (px) within dark and bright domains were extracted. Their scattering was statistically evaluated by considering grey value histograms of approximately ten pictures per sample. All pictures were used in the as-recorded version. For at least twenty independent areas with visible patterns, the grey value distribution was fitted with two Gaussians. Thus, the individual mean values could be quantified and their differences calculated. Averaging the differences yields a number which can be interpreted as a number for the domain contrast. The contrasts for all samples have then

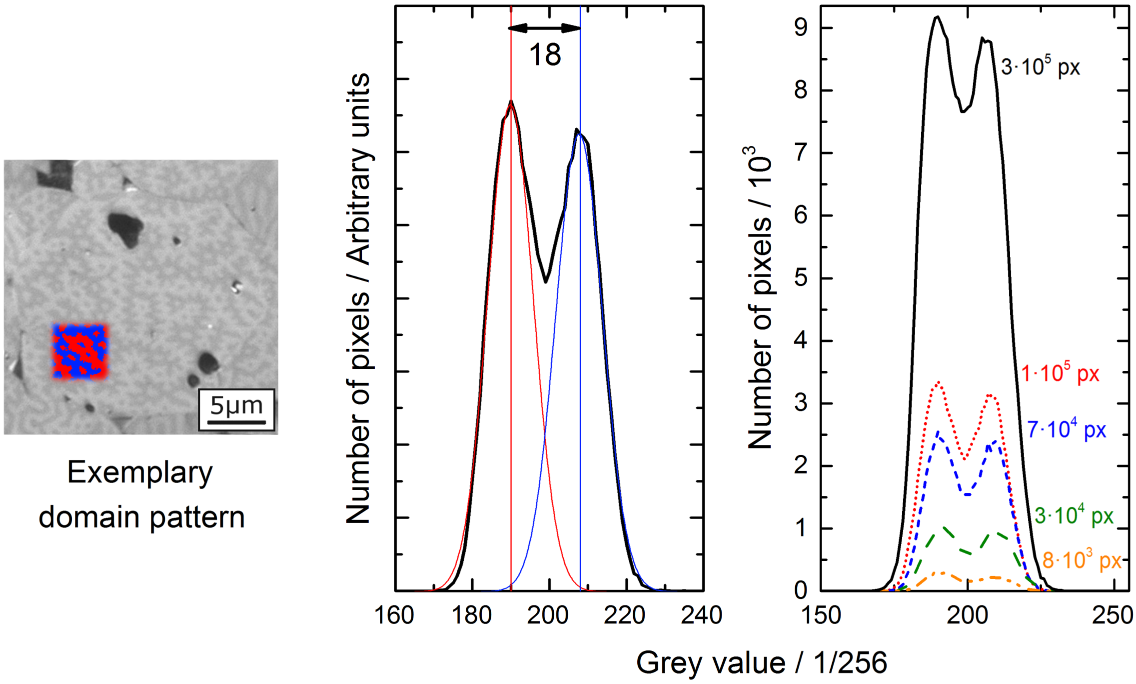

Exemplary domain pattern

Figure 3.4: Determination of the domain contrast from domain patterns recorded by PLM. The grey value histogram of a selected analysis area (left) is reconstructed by two Gaussians (center). Their mean value difference yields the contrast which is independent of the size of the actual area (right).

been compared to the corresponding saturation polarizations measured in this work or taken from literature.

For sufficiently large areas it was found that the obtainable grey value histograms are independent of the actual number of considered pixels. Showing the same shape and features, the histograms do therefore coincide when multiplied with a specific scaling factor.

3.2.5 Thermal analysis

Curie temperatures were measured under Ar-atmosphere on single phase samples with a mass of about 30 μg using a Seiko Instruments Exstar 6300R TG/ DTA balance customized by a permanent magnet mounted below the sample support (Magnet-TG). Here, TG stands for thermogravimetry. Attracting forces between the external magnet and the initially ferromagnetic sample contribute to an apparent gain in mass of the latter. Reaching T_C, the prompt loss of the contribution from magnetic interactions leads to a strong change of the measured weight load. That transition to the paramagnetic state determines T_C.

Figure 3.5 shows the determination of T_C using the Magnet-TG-setup for an exemplary sample. The differentiated signal yields approximately the same characteristic temperature as the temperature-dependent tracking of magnetization in a corresponding VSM-measurement. The lower the externally applied field, the sharper the transition and the more exact the value. This, however, comes at the expense of the measured signal's intensity.

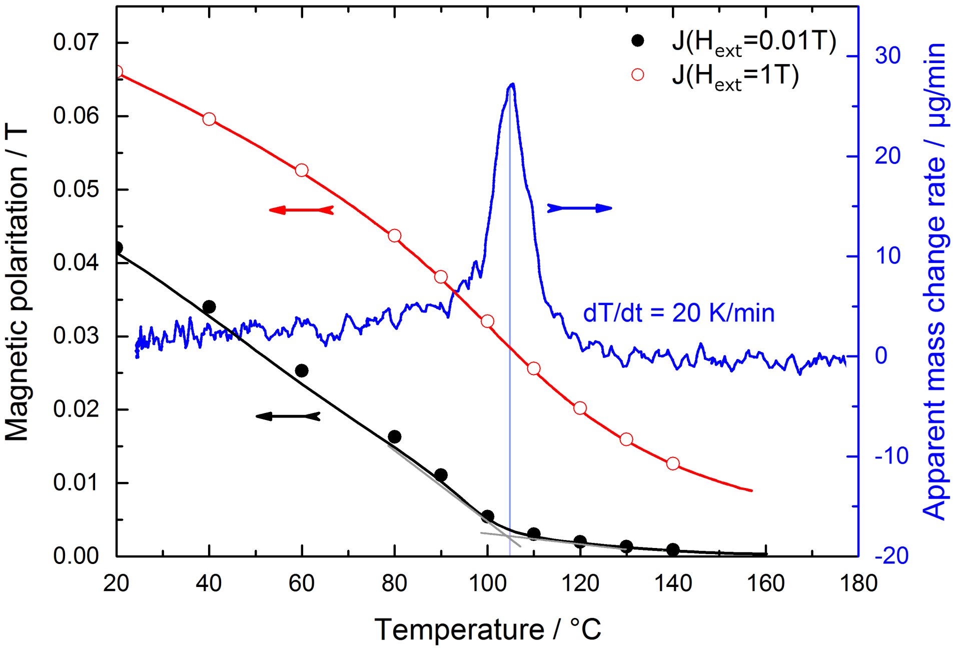

Figure 3.5: Comparison of techniques for the determination of Curie temperature in case of an exemplary $Sm_1Fe_{10x}Al_xMo_2$-sample. The (with decreasing H_{ext} increasingly defined) loss of magnetization at T_C measured in a VSM yields the same value as the Magnet-TG-setup.

Interestingly, samples have shown to behave differently when heated up once or repeatedly during the Magnet-TG-analysis. While the apparent mass increases steadily with an actual signal at T_C in the first measurement, this increase is no longer observed during following measurements. The initial heating behavior reoccurs if the cold sample is turned on its support prior to a subsequent run.

Conventional DTA-measurements (without the mounted magnet) were occasionally used to identify melting temperatures of specific phases for the estimation of appropriate process temperatures regarding melt-spinning, hot-pressing and die-upsetting.
The respective devices for DTA- and Magnet-TG-measurements were operated by Mr. Mario Tuchen. The samples were prepared and chosen by the author. The same is true for the interpretation of the raw data.

4 Results and Discussion

In the following, the elaborated results are presented. The obtained results are separated based on the different material systems as well as the Kerr microscopy analyses. The respective parts are completed by closing evaluations.

Within the framework of this dissertation, parts of the presented results were published in relevant journals. These original sources are listed explicitly as own publications at the very end.

4.1 The system Sm-Fe-Mo-Al

4.1.1 Phase diagram studies

Starting point for the study of Al-substitution for Fe in the ferromagnetic $Sm_1Fe_{10}Mo_2$-phase is the investigation of the underlying phase diagram. While the constitutions in binary mixtures are extensively reported in literature, ternary analyses are infrequent and limited to few temperatures [21, 24, 26, 42, 43, 122, 174].
In order to derive the quaternary, Fe-rich phase diagram, arc-melted samples with different compositions were annealed and analyzed. The samples are representative for isothermal conditions at 1000 °C and suitable to identify important intermetallics as well as border phases coexisting with the Th_1Mn_{12}-phase. The temperature seems appropriate because it allows the $Sm_1Fe_{10-x}Al_xMo_2$-phase to be stable. It represents a regime which would be favorable for the production of a sintered magnet - provided that the characteristics of the phase are reasonable. Furthermore, the corresponding heat promotes driving forces for reaching equilibrium states within reasonable time scales.

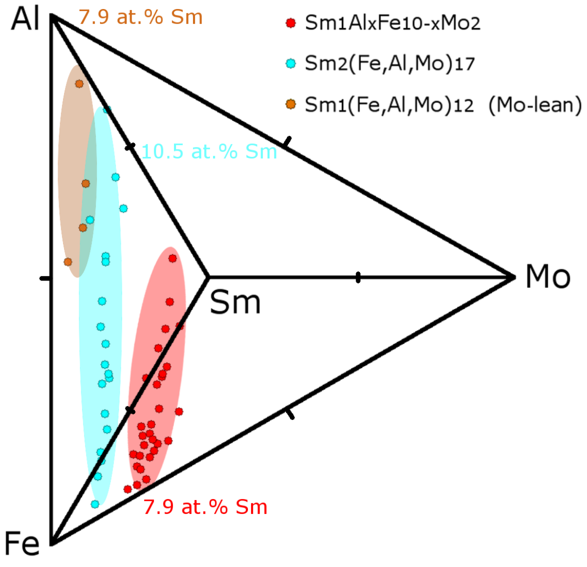

Figure 4.1: Stability ranges of selected phases in the quaternary, Fe-rich system Sm-Fe-Mo-Al for isothermal conditions of 1000 °C. Emphasized is the successive substitution of Al for Fe.

Figure 4.1 presents the constructed quaternary phase diagram as a tetrahedron plot being looked upon from the Sm-edge. The respective stability regions of $Sm_1Fe_{10-x}Al_xMo_2$, its Mo-lean counterpart (high Al-contents) and the corresponding 2:17-phase, $Sm_2Fe_{15.7-x}Al_xMo_{1.3}$, are plotted. Further prominent phases of the system are neglected for clarity. For both, the 1:12- and 2:17-phase, it is in principle possible to substitute nearly all Fe-atoms by Al. However, the 1:12-phase undergoes a transition close to 50 at.% Al (x=6.5). For higher contents, the role of Mo as structure-stabilizing element is taken over by Al. It will be shown later, that the phase then loses its ferromagnetic properties at RT, which is why it is not analyzed in more detail. Corresponding properties are provided in literature [175, 176].
The ferromagnetic, Mo-rich 1:12-phase occurring for low Al-contents will throughout be referred to as $Sm_1Fe_{10-x}Al_xMo_2$. With a constant tolerance regarding the index of Mo already at x=0.0, possible amounts of the latter element increase slightly when more Al is added. Values of about 15 at.% with deviations in the order of 2 at.% are in accordance with literature [22, 44, 45, 149, 177, 178].

Depending on the global composition, there are further phases in equilibrium with the discussed phases of interest. The complete set of detected phases in the annealed samples is presented in Table 4.1. Their occurrence is in agreement with available information. Solubility ranges for the involved elements of the material system Sm-Fe-Mo-Al are also presented. $Sm_1(Fe,Al)_2$ shows a full interchangeability of Fe and Al while other phases are more restricted in their composition.

Table 4.1: Solubilities of main equilibrium phases that occur in the vicinity of $Sm_1Fe_{10-x}Al_xMo_2$ at 1000 °C.

	Phase	Sm / at.%	Fe / at.%	Al / at.%	Mo / at.%
1	1:12	7.6-8.1	39-77	0-38	14-21
2	Mo – lean 1:12	7.8-8.1	5-43	49-83	0-4
3	2:17	10.3-11.1	9-100	0-72	0-8
4	$Sm_1(Fe,Al)_2$	30-34	0-100	0-100	0-3
5	Fe_7Mo_6	-	50-62	0-14	37-47
6	Mo_3Al_1	-	0-5	20-22	73-75
7	Sm solid solution	90-100	0-2	0-6	0-1
8	α-Fe solid solution	-	80-100	0-6	0-8

Supplementary to the previous findings, relevant phases of the material system were tried to be obtained by the reaction sintering and -crucible method in order to test the suitability of these approaches for the fast screening of unknown phases. Figure 4.2 presents the corresponding results. Reaction sintering does not necessarily identify all of the potential phases. For 2 h, 10 h and 24 h at 1000 °C the observable phases are strongly correlated with the chosen element ratio. If equal masses of all elements are provided, there is only the Mo-lean 1:12-phase together with Mo_3Al and an Al-rich 2:17-phase detectable. For a global composition close to the stoichiometric 1:12-phase (especially Fe-rich), the latter can be obtained in significant amounts together with solid solutions of Fe and Sm. Since the local composition may deviate, it is possible to explain traces of Fe_7Mo_6. Essentially, the samples behave like the annealed bulk alloy pieces. The technique is limited to previously defined compositions and it is not ensured to necessarily find all phases in that region of interest. Furthermore, phase regions might be very small so that they are hard to find, identify and characterize, particularly by Kerr microscopy.

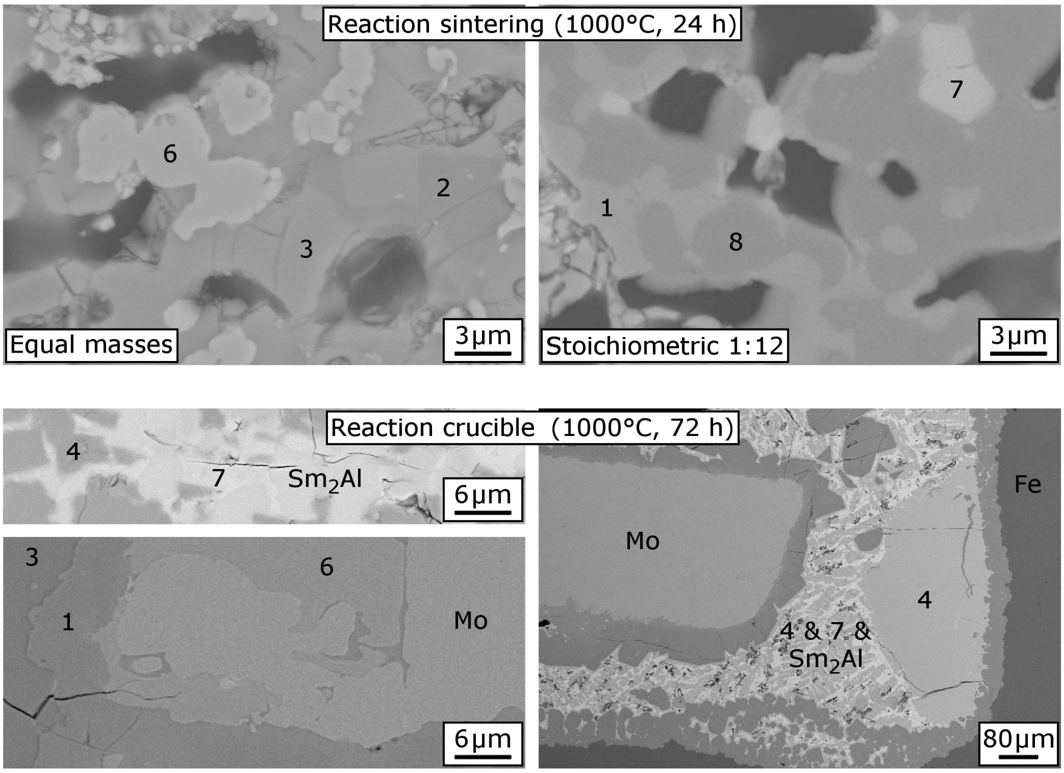

Figure 4.2: Determined phases for the system Sm-Fe-Mo-Al from reaction sintering (top) and the reaction crucible method (bottom). Phases are labeled according to their numbers in Table 4.1.

The reaction crucible method is more suitable for the efficient elucidation of phases in a multi-component material system provided that crucibles from a key component can be produced. Due to the massive sample, quenching may be too slow to suppress the formation of phases like Sm_2Al_1 which is formed when falling below 860 °C [179]. The high melting point of Mo and its poor contact with the Fe-crucible might prevent the occurrence of Fe_7Mo_6.
From the phase diagram analyses, it can be concluded that the formation of $Sm_1Fe_{10-x}Al_xMo_2$ and its equilibrium phases in the Fe-rich corner (0.0 at.% $\leq$ Mo $\leq$ 15.4 at.% & Al < 50 at.%) is significantly determined by the actual Sm-content. It can be differentiated between the following four multi-phase regions:

I Sm < 7.9 at.% :
Equilibrium of α-Fe solid solution, Fe_7Mo_6 and $Sm_1Fe_{10-x}Al_xMo_2$.

II 7.9 at.% $\leq$ Sm $\leq$ 10.5 at.%:
Equilibrium of $Sm_1Fe_{10-x}Al_xMo_2$ and $Sm_2Fe_{15.7-x}Al_xMo_{1.3}$.

III 10.5 at.% < Sm $\lesssim$ 14 at.%:
Equilibrium of $Sm_1Fe_{10-x}Al_xMo_2$, $Sm_2Fe_{15.7-x}Al_xMo_{1.3}$ and $Sm_1(Fe,Al)_2$.

IV Sm $\gtrsim$ 14 at.%:
Equilibrium of $Sm_2Fe_{15.7-x}Al_xMo_{1.3}$, $Sm_1(Fe,Al)_2$ and Sm solid solution.

4.1.2 Structural characterization

The increasing substitution of Al for Fe in $Sm_1Fe_{10-x}Al_xMo_2$ affects the unit cell of the material. Table 4.2 quantifies the effect based on Rietveld refinements of diffractograms obtained for arc-melted and annealed bulk samples. The latter are characterized by high percentages of the main phase and therefore suitable for the determination. The amount of secondary phases can be quantified to less than 15 wt.%. The determined lattice parameters (**a** and **c**) of the limiting phase $Sm_1Fe_{10}Mo_2$ agree well with those reported in literature [22, 44, 46].

Table 4.2: Dependence of the lattice parameters and the theoretical density of $Sm_1Fe_{10-x}Al_xMo_2$ on the Al-content. All values are based on Rietveld refinements of corresponding XRD-measurements.

Phase	x	a / Å	c / Å	ρ_{XRD} / g/cm^3
$Sm_xFe_{10-x}Al_xMo_2$	0.0	8.590 ± 0.003	4.806 ± 0.003	8.435 ± 0.007
	0.5	8.608 ± 0.003	4.817 ± 0.003	8.252 ± 0.007
	0.9	8.632 ± 0.003	4.822 ± 0.003	8.093 ± 0.007
	1.3	8.644 ± 0.003	4.834 ± 0.003	7.947 ± 0.007
	1.5	8.662 ± 0.003	4.843 ± 0.003	7.831 ± 0.007
	2.2	8.697 ± 0.003	4.871 ± 0.003	7.534 ± 0.007
	3.0	8.739 ± 0.003	4.891 ± 0.003	7.235 ± 0.007

As the Al-content is consecutively raised, both increase linearly. Thus, the effect is equally pronounced for all directions. The stretching of the unit cell, accompanied by the subsequent replacement of Fe by Al, can be traced back to the radius of Al which is greater than that of the original Fe [45, 47–49, 180]. Densities, calculated based on the refined data, decrease steadily which is due to the linearly growing unit cell and the increasing proportion of lighter atoms therein.

A more detailed picture of the crystal structure can be obtained by the determination of occupational conditions on the individual crystallographic sites. Thus, the simultaneous refinement of X-ray- and neutron diffraction data helps to explain the observed, isodirectional expansion of the unit cell and to resolve the interatomic distances of the different atoms. Figure 4.3 shows both datasets together with fits that correspond to their calculated, common structure. The derived unit cell in correct scale is also provided. The underlying powdered $Sm_1Fe_8Al_2Mo_2$-sample is virtually a single phase material as can be derived from the measurements. Reflection positions and shapes can be well reproduced by the refinement. Additional reflections, that are not described by the fit, originate from the AlMg3-sample support or negligible amounts of secondary phases. The depicted unit cell shows the particularly large Sm-atoms [181] occupying solely crystallographic 2a-sites. The remaining species, Fe, Al and Mo, are situated with specific occupation ratios (pie diagrams) on the remaining ones. Al distributes in a way that 1/3 of the dopant atoms occupy 8i- and 2/3 the 8j-sites. The 8f-site exclusively accommodates the original Fe. The fact that stabilizing- and dopant elements can divide on multiple sites is in accordance with former experiments [131, 182–185]. Dopant atoms are especially stated to occupy 8j-sites in addition to 8i, even though the prior contributes to a smaller energy decrease. Therefore, this cannot be explained by calculations based on the total energy [186, 187]. Since

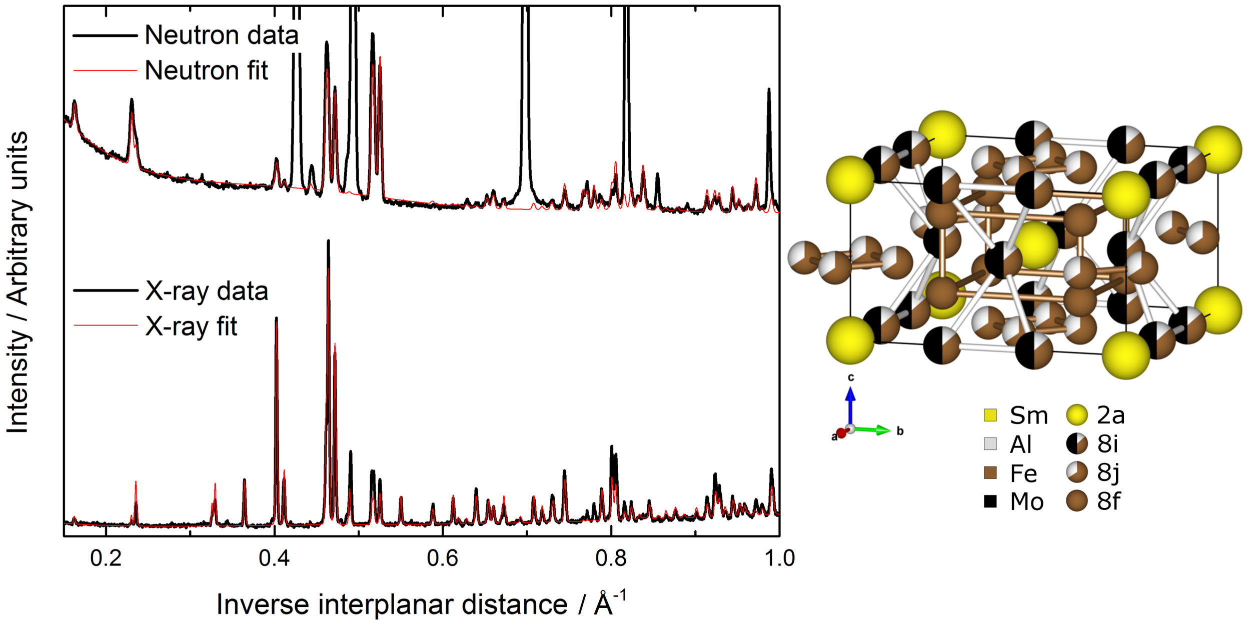

Figure 4.3: Raw data and refinement results of the X-ray- and neutron diffraction experiment on annealed $Sm_1Fe_8Al_2Mo_2$-powder (left). Reflections that originate from the AlMg3-sample support or negligible amounts of secondary phases are ignored. The resulting structure with the determined occupation of crystallographic sites is also provided (right).

the addition of Al is supplementary regarding the stabilization of the structure, there are basically no calculations for phases with this element performed in literature. Furthermore, due to its greater radius, dopant Al forms a special case. Its likewise incorporation on 8i and 8j affects all crystalline directions. The observation of an uniformly stretched unit cell can be explained by the size mismatch between Al and Fe. Moreover, the present refinement confirms the strong 8i-preference of the structure-stabilizing Mo being especially stated to decrease the overall energy [24, 46, 182, 187–189]. Since the proximity of Sm- to Mo-atoms is associated with a positive energy contribution and there are only 4 nearest 8i-type neighbors in the vicinity of the 2a-site (unlike 8 each in case of 8j- and 8f-type), the observed preference seems reasonable [190].

4.1.3 Magnetic characterization

Intrinsic properties

Changes of the unit cell result in altered interatomic distances and may therefore result in altered magnetic properties which are not necessarily explainable by the simple substitution of magnetically active atoms, like Fe in the present case. For an estimation of J_S, melt-spun ribbons (constant wheel speed of 20 m/s) with a Sm-content of 8.0 at.% to 8.4 at.% were produced. This content is slightly above the calculated amount for a nominal, stoichiometric composition of $Sm_1Fe_{10-x}Al_xMo_2$ (≈ 7.7 at.%). The resultant ribbon material, corresponding to three different Al-contents, turns out to be composed almost exclusively of the main phase, with less than 2 wt.% of α-Fe as the only secondary phase. PPMS-measurements up to high fields are shown in Figure 4.4. The observable high-field polarizations decrease from 0.66 T (x=0.0) over 0.52 T (x=0.8) down to 0.44 T (x=2.0). All stabilizing Mo-atoms in the $Sm_1Fe_{10-x}Al_xMo_2$-unit cell, exclusively occupy 8i-sites where Fe would contribute particularly to a high moment. This lowers the potential J_s of the phase series as experimentally confirmed by the measurements. The observed decrease with increasing Al-content is attributed to the further reduction of the number of Fe-atoms. However, the decaying evolution of J_s (high-field polarizations are taken as a measure for J_S) is non-linear, indicating complex changes of the interactions between individual atoms on the underlying lattice. These seem to go beyond the non-equivalent consideration of the individual sites.

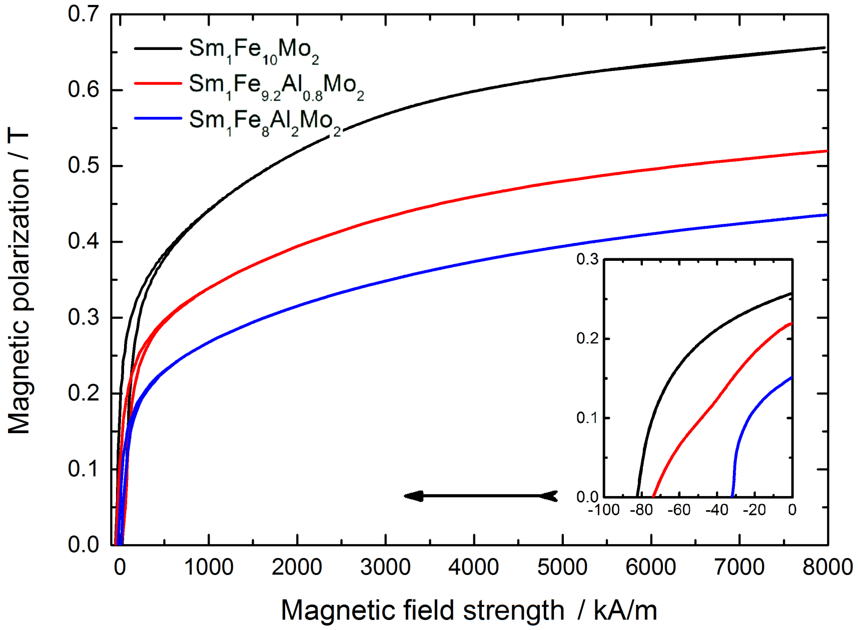

Figure 4.4: PPMS-measurements of single phase $Sm_1Fe_{10-x}Al_xMo_2$-melt-spun ribbons with different Al-contents. Magnetic polarizations obtained in a field of 8 MA/m are taken as a measure for the saturation values J_s. The inset highlights the obtained coercivities in the as-spun state.

As a further intrinsic quantity, Curie temperatures (Magnet-TG) were measured on single phase bulk samples of $Sm_1Fe_{10-x}Al_xMo_2$ and $Sm_2Fe_{15.7-x}Al_xMo_{1.3}$. Mixtures, occurring for a global Sm-content between 7.9 at.% and 10.5 at.%, were also taken into consideration. Figure 4.5 shows the changing of T_C with Al-content regarding both of the initially (x=0.0) ferromagnetic phases. It can be seen that the respective trend curves initially indicate an increase of T_C, which saturates at x=0.5 and x=1.0 for the 1:12- and 2:17-phase, respectively. For higher Al-contents, the values decline non-linearly until for samples with x=3.0 (1:12) and x=5.5 (2:17) no more signals can be registered by the Magnet-TG-technique above RT. Absolute values for the Al-free (x=0.0) phases fit to those reported in literature. However, there are discrepancies of more than 70 °C in case of $Sm_1Fe_{10}Mo_2$ which might be due to the solubility range regarding Mo [149, 183, 189]. For some specific compositions, this effect has been presented before [45]. The trend of decreasing T_C with ongoing substitution of Mo for Fe has also been reported [190]. In the present work, the change with Al-content is observed and the Mo-content kept unchanged. A decrease with further dopant elements holds true which might also be explained by an increase in Fe-Fe-exchange interaction length [180].

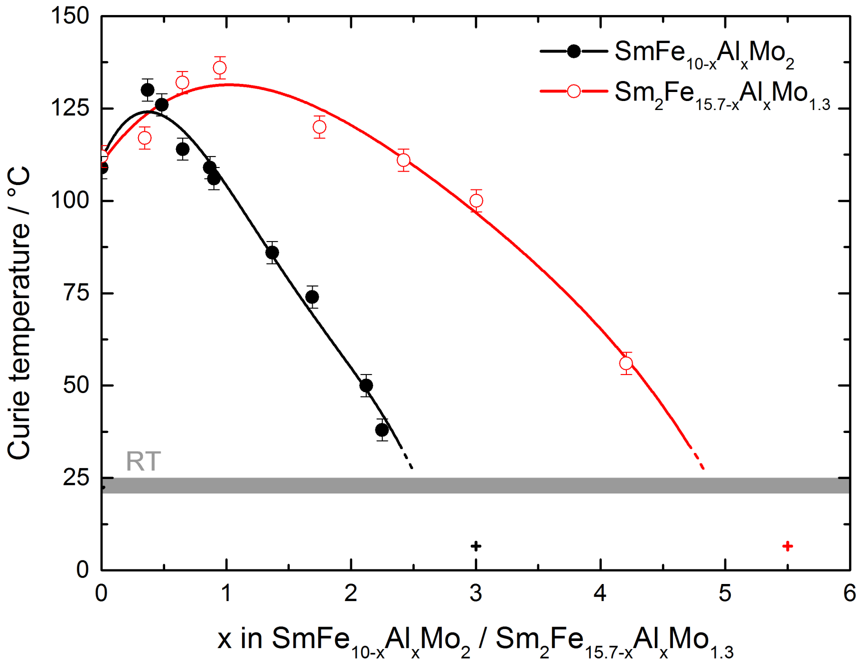

Figure 4.5: Development of T_C with increasing Al-content for $Sm_1Fe_{10}Al_xMo_2$ and $Sm_2Fe_{15.7-x}Al_xMo_{1.3}$. Measurements for x=3.0 and x=5.5, respectively, do no longer yield a signal above RT.

Extrinsic properties

The following section covers the evolution of coercive field strength for different annealings of intensively milled $Sm_1Fe_{10-x}Al_xMo_2$-powders. The global compositions of these are presented in Table A.1 (see appendix). Like the single phase melt-spun ribbons for the estimation of J_S, the related powder compositions have an Sm-excess with respect to the nominal 1:12-stoichiometry. Due to the processing via ingot precursors, the actual content varies between 8.1 at.% and 8.5 at.%.

Figure 4.6 illustrates the H_c-values measured for the individually annealed samples. Within a reasonable range of conditions, it is generally possible to perceive a coercivity increase with progressively raised annealing times and -temperatures. The increase from the practical absence of any H_c in the as-milled state to the first meaningful value of a recrystallized material is especially pronounced. At temperatures below 800 °C, considerable coercivities can hardly be obtained. For sufficiently high temperatures, steady maximum values $H_{c,max}$ are reached within 10 min to 30 min. In the present case the corresponding temperature can be concretized to 900 °C. For very short times at 1000 °C, coercivity approximates $H_{c,max}$, however falling rapidly as the heat treatments get longer. This confirms that the considered experiments cover the full range of obtainable H_c. Therefore, the scope from Figure 4.6 is sufficient to identify optimal treatments for the tuning of the nanocrystalline materials. The content of detrimental light elements is low enough so that the obtained values are not affected (compare Table 3.2).

The measured maximum coercivities for x=0.0 and x=0.8 are 153 kA/m and 139 kA/m, respectively. The composition with highest Al-content (x=2.0), in contrast, achieves coercivities that are below 40 kA/m and preferentially obtained for 700 °C to 800 °C. These findings are in

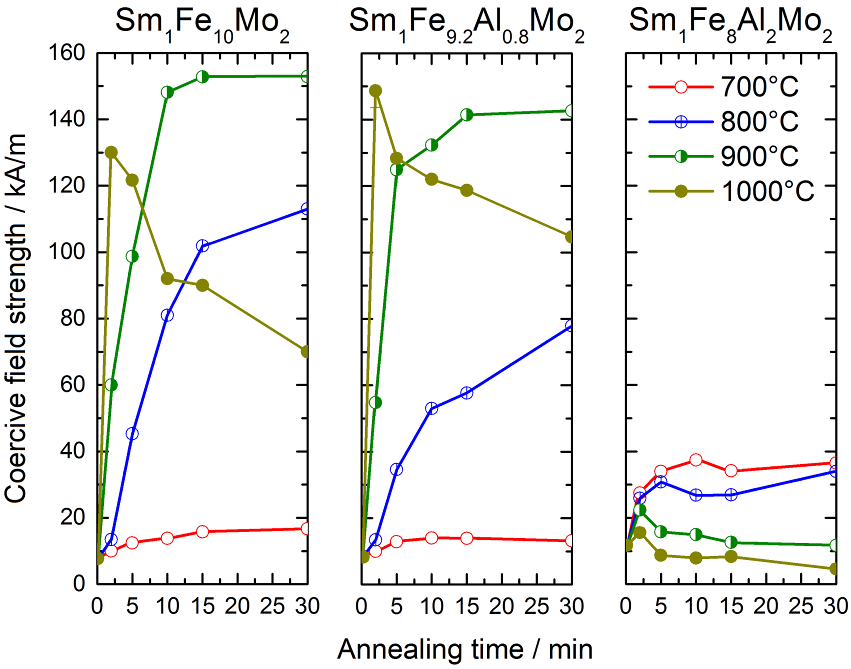

Figure 4.6: Coercivities measured on intensively milled and subsequently annealed $Sm_1Fe_{10-x}Al_xMo_2$-powders.

accordance with measurements of the nanocrystalline melt-spun ribbons in their as-spun state. The coercivities, given in the inset of Figure 4.4, might still be tunable but fall into a comparable range. Thus, it is concluded that the possible $H_{c,max}$ strongly decreases as the Al-content exceeds a certain limit above x=0.8. These materials can no longer reach values that are comparable to the compositions with less Al.

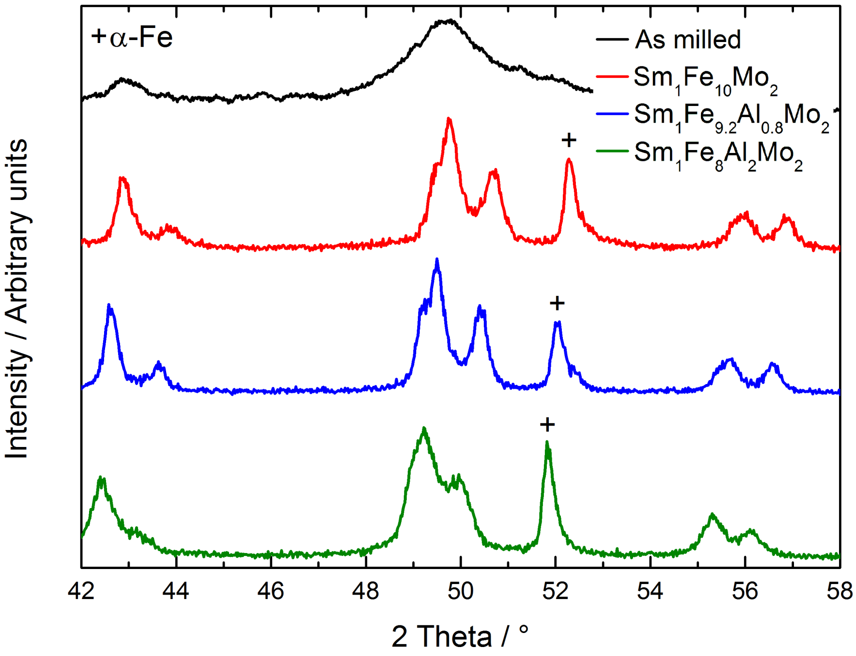

Figure 4.7: X-ray diffractograms of an exemplary powder in the as-milled state together with representatives of the different compositions annealed for 30 min at 900 °C.

Complementary to the previous characterization of H_c, Figure 4.7 presents corresponding X-ray diffractograms of the annealed powders. Starting from the exemplarily plotted, as-milled state of the respective powders, annealings of 30 min at 900 °C lead to the formation of the characteristic Th_1Mn_{12}-lattice reflections. Detailed analysis indicates the presence of neighboring α-Fe solid solution for all three compositions. Partially, this solid solution contains significant percentages of Al in the body-centered cubic lattice. As the crystallization originates immanently from an α-Fe-related structure it is not possible to completely avoid its presence in the final powders [191, 192].

Since the characteristic triplet at about 50 °2θ has not yet evolved completely, its formation has been closer investigated in the context of emerging coercivity. The progressive crystallization for a temperature of 900 °C is given in Figure 4.8. Contents of residual α-Fe can equally be quantified to approximately 10 wt.%–15 wt.% depending on the powder.

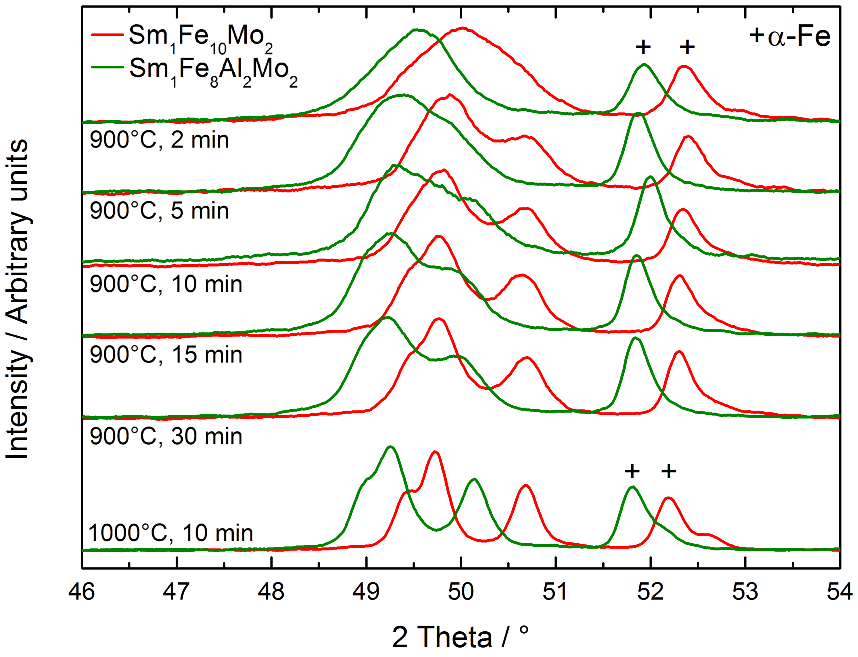

Figure 4.8: Diffractograms of the intensively milled $Sm_1Fe_{10}Mo_2$- and $Sm_1Fe_8Al_2Mo_2$-powders annealed for different times at 900 °C and 1000 °C, respectively. Focus is set on the characteristic triplet and the α-Fe-reflection. The latter reflection shifts because of a significant Al-percentage in the lattice.

For all annealing times, the Al-free composition is found to crystallize significantly faster. In reverse, the altered kinetics for powders with high Al-content (x=2.0) might explain their inverse evolution of H_c with annealing temperatures (see Figure 4.6). Both, the definedness of reflections and the obtained coercivities are consequences of the achieved crystallite size after recrystallization. Exemplary quantifications from refinements of associated diffractograms yield typical n-th-root-shaped increases from roughly 15 nm (900 °C, 2 min) to 35 nm and 23 nm (900 °C, 30 min) for x=0.0 and x=2.0, respectively (see Figure A.2 in the appendix). Here, n is the number of the root. It therefore proves the trend which is already apparent from the developments of H_c. An initial (as-milled) crystallite size cannot be determined because the relevant structure does not yet exist. For an annealing of 10 min at 1000 °C, the resultant crystallite sizes show a similar ratio with absolute sizes of 82 nm (x=0.0) and 55 nm (x=2.0). For both temperatures, fitting of the crystallite sizes requires n>2 (number of the root) which is typical for fine dispersed particles hindering the movement of grain boundaries (Zener pinning) [193]. Achieving a final, maximum size of recrystallized 1:12-grains can also be due to the size of powder agglomerates.

Furthermore, increasing Al-contents shift reflections of equivalent lattice planes to lower angles which is a consequence of the described stretching of the unit cell when Al is substituted for Fe in $Sm_1Fe_{10-x}Al_xMo_2$. The same information can be taken from Figure 4.7 where diffractograms of powders with all three Al-contents are shown.

For annealings at 1000 °C the Th_1Mn_{12}-reflection triplet of $Sm_1Fe_8Al_2Mo_2$ becomes sufficiently defined. However, the consistently lower coercivities indicate that the greatly reduced values are indeed reasoned by the composition. Assuming that the extrinsic values are equally reduced for all compositions (with respect to their intrinsic counterparts), it is concluded that the 1:12-phase with $x=2.0$ has a significantly lower H_a and reduced magnetocrystalline anisotropy compared to Al-lean representatives of the series.

4.1.4 Closing evaluation

The $Sm_1Fe_{10-x}Al_xMo_2$-phase is characterized by moderate values for the saturation polarization and especially low Curie temperatures. Coercive field strengths cannot be increased significantly above 150 kA/m in the experiments. The substitution of Fe by Al even leads to a decrease.
Even though the 1:12-phase forms easily for the chosen conditions, it appears impracticable for a new material with intermediate properties. Furthermore, it reduces the relevance of the system Sm-Fe-Mo-Al in this context. Due to the weak prospects for future applications, there is no motive to produce a demonstrator product. In addition, the prerequisites for a corresponding approach are questionable because of the observed neighboring phases.

4.2 The system Ce-Sm-Fe-Ti-V

4.2.1 Phase diagram studies

The phase diagram of the material system Ce-Sm-Fe-Ti-V has been assessed with predominantly Fe-rich samples annealed at 1000 °C. Most of the limiting binary and ternary diagrams are well-known because especially Ti and V are common alloying elements for steel (prevention of intercrystalline corrosion, increase of tensile strength). As presented previously, the corresponding (binary and ternary) ferromagnetic phases are prominent and intensively studied, especially since the RE-crisis [4, 13, 124, 194–196].

Constructed from annealed samples with different global compositions, Figure 4.9 sets focus on the stability ranges of the ferromagnetic Th_1Mn_{12}-phases and thus the interchangeability of the stabilizing transition elements. It can be noticed that, independent of the RE-element, the stoichiometry of the 1:12-phase tends to change from $RE_1Fe_{11}TM_1$ (favored for Ti) towards $RE_1Fe_{10}TM_2$ (favored for V) allowing also for intermediates. Furthermore, the 2:17-phase requires not necessarily the stabilization by Ti and V and does only allow for considerably less amounts of these. With a just slightly larger solubility for V, the phase extends more similarly with substitutions of Ti and/ or V for Fe.

It should be mentioned that $Ce_1Fe_{10}V_2$ could never be obtained for the present annealing conditions. The opposed stoichiometry, $RE_1Fe_{11}V_1$, could infrequently and in small amounts be observed when temperatures were considerably higher (1150 °C) and annealing times longer.

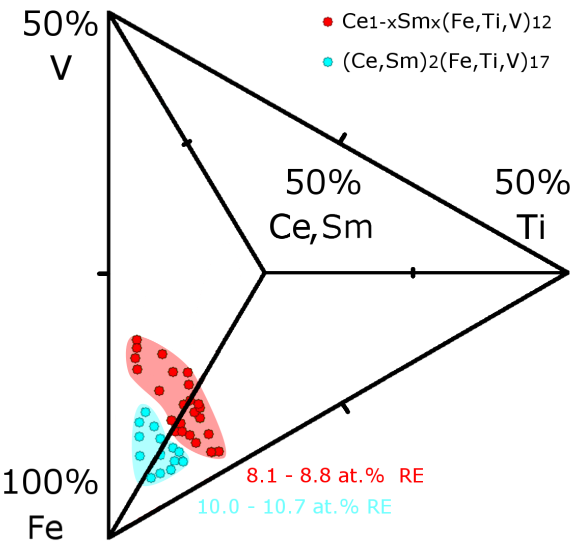

Figure 4.9: Stability ranges of selected, ferromagnetic phases in the pseudo-quaternary, Fe-rich system RE-Fe-Ti-V (RE=Ce, Sm) for isothermal conditions of 1000 °C. Note that the region of interest is magnified.

From annealed bulk samples with various global compositions, valuable information about possible stoichiometries of relevant phases in the system Ce-Sm-Fe-Ti-V can be obtained. The results are listed in Table 4.3. The compositions of enumerated phases are - where available - in accordance with reports [27, 41, 124, 197–201].

Table 4.3: Solubilities of main equilibrium phases that occur in the vicinity of $Ce_{1-x}Sm_xFe_{11}Ti_1$ and $Ce_{1-x}Sm_xFe_{10}Ti_1V_1$ at 1000 °C.

	Phase	Ce / at.%	Sm / at.%	Fe / at.%	Ti / at.%	V / at.%
1	1:12	0-8.9	0-8.1	76-87	0-9	0-15
2	2:17	10-11	10-11	83-89	0-6	0-7
3	RE_1Fe_2	0-36	0-36	63-65	0-2	0-2
4	Fe_2Ti_1	-	-	38-70	27-37	0-29
5	(Ce, Sm) solid solution	0-100	0-100	0-2	0-2	0-2
6	α-Fe solid solution	-	-	71-100	0-4	0-29

Knowledge of the preferential phase compositions for given conditions has a special relevance for experiments with multi-element, nanocrystalline material. It is also required for the fabrication of virtually single phase samples that are suitable for magnetic characterization. Resultant sample morphologies (e.g. nanocrystallinity) may not allow for EDX-quantification. The identification and distinction of phases, which may behave different in terms of magnetic response, by XRD can be problematic especially if the patterns partially coincide.

Besides the ferromagnetic phases from Figure 4.9, Table 4.3 lists also phases with potentially broad solubility regions. For those, the typical equilibrium compositions for global compositions close to stoichiometric $RE_1Fe_{11}Ti_1$ and $RE_1Fe_{10}Ti_1V_1$ are of central interest. The intermetallic RE_1Fe_2 does, thus, contain usually 5 at.% Sm even if equal amounts of Ce and Sm are present. In addition, Fe_2Ti_1 comes, for respective compositions (V-containing samples) with 5 at.% V in average.

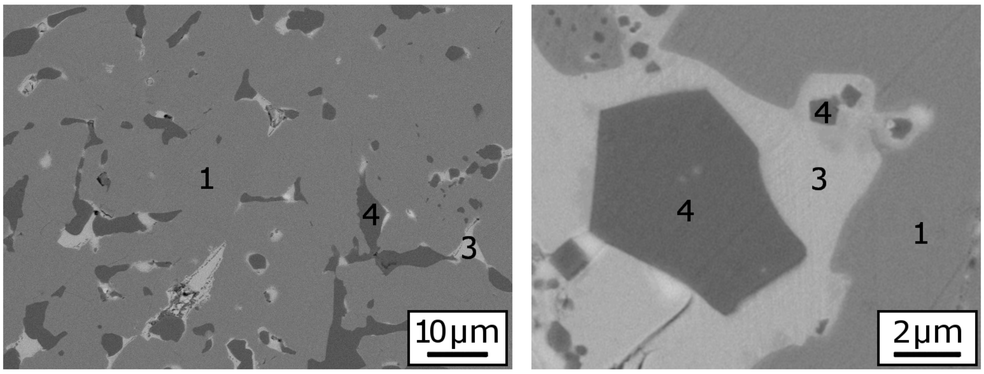

Figure 4.10: Impact of the presumable reaction between Ce_1Fe_2 and the ferromagnetic $Ce_1Fe_{11}Ti_1$-phase. For different magnifications, the phases are labeled according to their numbers in Table 4.3.

Pairings of the involved elements in bulk samples do also expose microstructural characteristics that are important for all lengthscales. An exemplary, annealed Ce-Fe-Ti-sample is shown in Figure 4.10. For different magnifications it can be seen that the boundaries of the 1:12-phase (main phase) are tattered where they are in touch with the bright Ce_1Fe_2. Particles of Fe_2Ti_1, which appear dark because of the absence of the heavier RE-atoms, form isles close to the concerned regions. The bright phase is known to be liquid at annealing temperatures above 925 °C and therefore thought to react at some point with the main phase. In Sm-based samples, the corresponding phase is solid at 1000 °C which might be the reason why the described effect does not show up there. Mixed RE, however, behave similarly like Ce-based ones as RE_1Fe_2 has shown to consist mainly of Ce (only 5 at.% Sm), not representing the global RE-ratio and therefore being liquid, too. The 1:12-phase accordingly suffers from the consumption resulting form the contact with Ce_1Fe_2. It is necessarily assumed that the tattered interfaces are detrimental regarding demagnetization processes in actual magnets.

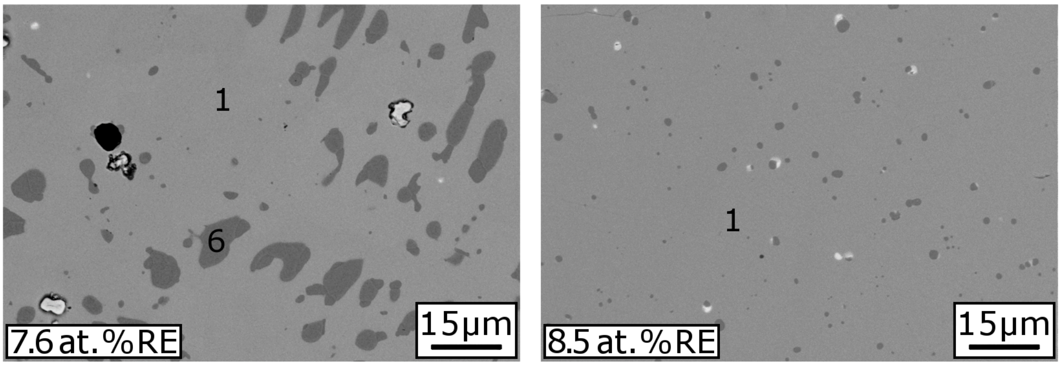

Figure 4.11: Arc-melted and annealed (1000 °C) $Ce_{0.5}Sm_{0.5}Fe_{10}Ti_1V_1$-samples with different RE-content regarding the global composition. An understoichiometric (left) and a stoichiometric (right) material is presented. Phases are labeled according to their numbers in Table 4.3.

The production of single phase bulk samples with compositions of $RE_1Fe_{11}Ti_1$ and $RE_1Fe_{10}Ti_1V_1$ has shown to be very sensitive to the elaborated element ratios. Figure 4.11 shows that the microstructure contains significant amounts of secondary phases, especially Fe_2Ti_1 or Fe with optionally certain concentrations of Ti and V, if the RE-content is close to the nominal 7.7 at.% suggested from the 1:12-stoichiometry.

Table 4.4: Measured equilibrium phase compositions of the different $Ce_{1-x}Sm_xFe_{11}Ti_1$- and $Ce_{1-x}Sm_xFe_{10}Ti_1V_1$-phases in arc-melted bulk samples annealed at 1000 °C.

Phase	x	Ce + Sm / at.%	Fe / at.%	Ti / at.%	V / at.%
$Ce_{1-x}Sm_x Fe_{11}Ti_1$	0.0	8.7	84.1	7.2	-
	0.2	8.5	83.4	7.5	-
	0.5	8.4	83.6	8.1	-
	0.8	8.1	84.8	7.1	-
	1.0	8.1	84.9	7.0	-
$Ce_{1-x}Sm_x Fe_{10}Ti_1V_1$	0.0	8.9	77.1	5.1	8.9
	0.2	8.5	77.0	5.3	9.2
	0.5	8.5	76.9	5.2	9.4
	0.7	8.3	77.6	6.2	7.9
	1.0	8.1	76.6	6.6	8.7

Proper magnetic characterization requires suitable samples, which are single phase after annealing. It has shown that for their fabrication the global compositions need to coincide with those, which were found by numerous EDX-point analyses of the respective phases. Corresponding average values, measured on annealed bulk samples, are listed in Table 4.4. Besides certain constraints, regarding the contents of stabilizing transition metals, which emerge from the desired RE-ratio and the presence of V, it is derived that the actual RE-percentage in the 1:12-phase shows a dependency on the Ce/Sm-ratio. With increasing Ce-content, it increases from 8.1 at.% to 8.7 at.%–8.9 at.%.

For the sake of simplicity, the phases will in the following still be referred to as $RE_1Fe_{11}Ti_1$ and $RE_1Fe_{10}Ti_1V_1$. The tolerance of the 2:17-phase regarding the RE-content is not further analyzed in terms of a Ce/Sm-dependence.

4.2.2 Structural characterization

Rietveld refinements of the obtained single phase samples allow to determine and track the evolution of the samples' individual lattice parameters **a** and **c**. Table 4.5 summarizes the corresponding results. With increasing Sm-content, the unit cell expands almost linearly in all directions which is, at a first glance, in contradiction to the lanthanide contraction suggesting shrinking radii for consecutive elements in the RE-series. However, calculated atomic radii match with the findings from this work and justify the increase of both lattice parameters [202]. Another possible explanation could arise from the uncommon chemistry of Ce (see Section 2.2.3). The progressive stretching with increasing Sm-content manifests with a slightly larger impact on lattice constant **c** compared to the a/b-plane. This can be attributed to the significantly shorter distance of neighboring RE-atoms parallel to the c-axis compared to repetitions along the space diagonal or a(=b)-axis.

Table 4.5: Dependence of the lattice parameters and the theoretical density of $Ce_{1-x}Sm_xFe_{11}Ti_1$ and $Ce_{1-x}Sm_xFe_{10}Ti_1V_1$ on the RE-ratio. All values are based on Rietveld refinements of corresponding XRD-measurements.

Phase	x	a / Å	c / Å	ρ_{XRD} / g/cm^3
$Ce_{1-x}Sm_x Fe_{11}Ti_1$	0.0	8.536 ± 0.003	4.782 ± 0.003	7.647 ± 0.007
	0.2	8.543 ± 0.003	4.787 ± 0.003	7.646 ± 0.007
	0.5	8.544 ± 0.003	4.788 ± 0.003	7.672 ± 0.007
	0.8	8.552 ± 0.003	4.793 ± 0.003	7.679 ± 0.007
	1.0	8.554 ± 0.003	4.796 ± 0.003	7.690 ± 0.007
$Ce_{1-x}Sm_x Fe_{10}Ti_1V_1$	0.0	8.529 ± 0.003	4.776 ± 0.003	7.622 ± 0.007
	0.2	8.534 ± 0.003	4.779 ± 0.003	7.628 ± 0.007
	0.5	8.541 ± 0.003	4.784 ± 0.003	7.637 ± 0.007
	0.7	8.544 ± 0.003	4.786 ± 0.003	7.648 ± 0.007
	1.0	8.556 ± 0.003	4.794 ± 0.003	7.643 ± 0.007

For all Ce/Sm-ratios, the replacement of Fe by V reduces the size of the unit cell. Unlike the steric considerations for the treatments of increasing Sm-content, calculated atomic radii fail to explain this observation. However, the radii experimentally determined from actual crystals indicate that V is smaller than Fe [203, 204].

With the described impacts of atom substitutions in the unit cell, the resulting volume and average mass of individual phase compositions determine the individual densities listed in the last column of Table 4.5. Actual values for the different representatives are likewise obtained from the refined diffractograms. With respect to inaccuracies from measurements and the evaluation technique, the densities of both series increase with increasing Sm-content. The V-free compositions are throughout less dense.

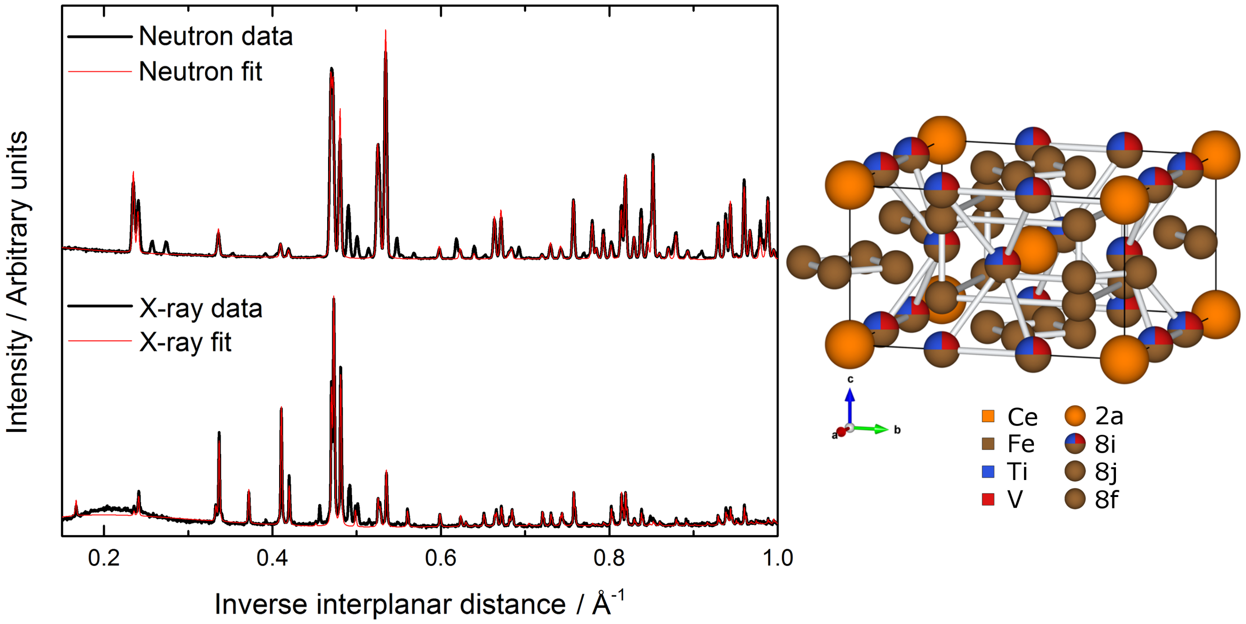

Figure 4.12: Raw data and refinement results of the X-ray- and neutron diffraction experiment on annealed $Ce_1Fe_{10}Ti_1V_1$-powder (left). Reflections that originate from the AlMg3-sample support or negligible amounts of secondary phases are ignored. The resulting structure with the determined occupation of crystallographic sites is also provided (right).

The simultaneous refinement of XRD- and ND-data is motivated by reports claiming different moments for Fe-atoms dependent on their individual crystallographic site [188, 205]. Figure 4.12 presents measurements and a refined fit for a $Ce_1Fe_{10}Ti_1V_1$-sample. The derived unit cell with correct lengthscales and site occupancies is also shown. Reflections of secondary phases are ignored in the fit of both datasets.

Assuming that the presence of Sm does not change the situation, it is derived that the RE-atoms occupy the 2a-site, Ti and V are both located on 8i and Fe fills the remaining positions. The strong preference for the occupation of 8i-sites of Ti and V agrees with results from literature where, just like in case of Mo, a decrease of cohesive energy is associated with the presence of these elements in the Th_1Mn_{12}-structure [141,174,206–209]. Irrespective of required amounts, these elements are therefore found to stabilize the phase. The Ce-based phase stabilized by Ti and V at the same time has not been studied before. The results are consistent with the limiting cases where only Ti or V is present.

4.2.3 Magnetic characterization

Intrinsic properties

The intrinsic magnetic properties are strongly determined by the observed crystal structure. Besides simple, geometric effects, the choice of the Ce/Sm-ratio has further far reaching impacts on the characteristic properties of the individual phase.

First, the saturation polarization is studied for multiple representatives of the $Ce_{1-x}Sm_xFe_{11}Ti_1$- and $Ce_{1-x}Sm_xFe_{10}Ti_1V_1$-series. Exact stoichiometries can be taken from Table 4.4. Corresponding high-field polarizations, measured on single phase bulk samples, are in the following taken as a measure for J_s. Figure 4.13 shows the corresponding data and allows for comparisons among the phases. Assuming an absolute error of 0.01 T, to account for inaccuracies of the measured sample mass and the derived theoretical density, both series do significantly separate into two narrow value ranges with widths of approximately 0.1 T and a difference of roughly 0.25 T between them. Samples of $RE_1Fe_{11}Ti_1$ and $RE_1Fe_{10}Ti_1V_1$ cover values from 1.13 T to 1.25 T and 0.85 T to 0.95 T, respectively. Within each series, the variation of the Ce/Sm-ratio causes only slight differences in J_s without a systematic dependence on the actual Sm-content.

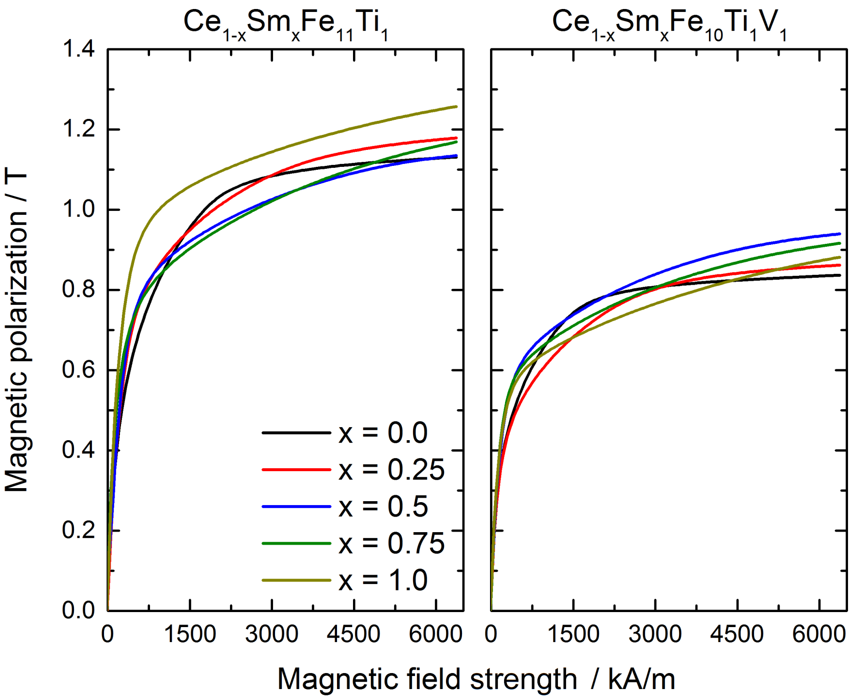

Figure 4.13: PPMS-measurements of single phase $Ce_{1-x}Sm_xFe_{11}Ti_1$- and $Ce_{1-x}Sm_xFe_{10}Ti_1V_1$-bulk samples with different RE-ratios. Magnetic polarizations obtained in a field of 6.5 MA/m are taken as a measure for the saturation values J_s.

Literature values are only available for the V-free phases with x=0.0, x=0.5 and x=1.0 [46,123, 131,133]. The measured values of this work agree well with these. The consistently inferior values of the V-containing samples in this work can be explained to the greatest extent by the lower number of Fe-atoms and the sites on which they are substituted. The number of atoms with considerable magnetic moment plays a major role. The fact that V occupies preferentially 8i-sites, where original Fe contributes especially to the total moment, yields a correction to deviations from a simple proportional approximation.

The significantly reduced J_s lower the potentially obtainable energy products for actual magnets provided that adequate processing is possible. The calculated $(BH)_{max,theo}$ (see Equation 2.1), are presented in Table 4.6 together with the corresponding J_s.

Anisotropy field strengths have been determined from measurements parallel and perpendicular to the easy magnetization axis of textured samples. The annealed and powderized starting materials are characterized by high phase purities.
Figure 4.14 exemplarily shows the estimation of H_a for $Ce_1Fe_{10}Ti_1V_1$. The slope, associated with its magnetically hard axis is extrapolated from the origin and yields the anisotropy field strength as intersection with the measurement parallel to the easy axis. It is understood as corresponding response of the pure material. Accordingly, small amounts of rapidly saturated secondary phases are responsible for the subtracted offset after an early increase with high susceptibility. The second derivative of the measurement perpendicular to the easy axis is also shown. According to SPD-theory, the cusp of the differentiated data reveals the previously hidden singularity whose position is likewise characteristic for the magnitude of H_a (see Section 3.2). Both approaches lead to comparable values and are suitable for the determination.

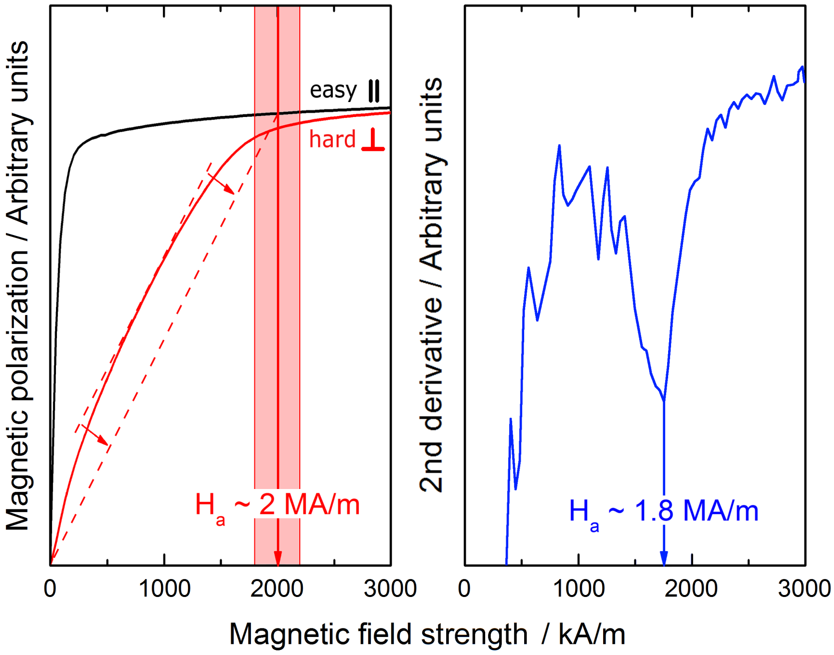

Figure 4.14: Estimation of the anisotropy field strength for aligned $Ce_1Fe_{10}Ti_1V_1$-powder particles. Measurements parallel and perpendicular to the easy axes allow to find the corresponding intersection (left). The position of the cusp in the differentiated curve yields a similar value (right).

Corresponding values for the different samples of interest are listed in Table 4.6. A selection of magnetic measurements on textured samples for the determination of the anisotropy field strengths is given in Figure A.3 (see appendix). The comparison among the derived values shows that the magnetocrystalline anisotropy is especially high in Sm-rich phases and that the anisotropy decreases linearly with increasing Ce-content. The presence of V does not significantly affect H_a and its dependence on the RE-ratio. This agrees with literature reports where equal anisotropy field strengths of V-free and -containing phases were reported for the limiting case of RE=Sm (x=1.0) [17]. Therefore, the V-free and -containing series should in principle have the potential for similar coercivities.

Table 4.6: Dependence of the intrinsic properties of $Ce_{1-x}Sm_xFe_{11}Ti_1$ and $Ce_{1-x}Sm_xFe_{10}Ti_1V_1$ on the Sm-content. All values have been determined from measurements on single phase bulk samples.

Phase	x	J_s / T	$(BH)_{max,theo}$ / kJ/m^3	H_a / MA/m	T_C / °C
$Ce_{1-x}Sm_x$ $Fe_{11}Ti_1$	0.0	1.13 ± 0.01	254 ± 2	2.2 ± 0.3	208 ± 3
	0.2	1.18 ± 0.01	277 ± 2	3.7 ± 0.5	239 ± 3
	0.5	1.13 ± 0.01	254 ± 2	6.0 ± 1.4	269 ± 3
	0.8	1.17 ± 0.01	272 ± 2	7.7 ± 1.0	297 ± 3
	1.0	1.25 ± 0.01	311 ± 2	8.0 ± 1.6	310 ± 3
$Ce_{1-x}Sm_x$ $Fe_{10}Ti_1V_1$	0.0	0.85 ± 0.01	144 ± 2	2.0 ± 0.2	184 ± 3
	0.2	0.87 ± 0.01	151 ± 2	3.0 ± 0.3	215 ± 3
	0.5	0.95 ± 0.01	180 ± 2	5.1 ± 0.5	258 ± 3
	0.7	0.93 ± 0.01	172 ± 2	7.9 ± 0.6	305 ± 3
	1.0	0.89 ± 0.01	158 ± 2	8.7 ± 0.8	312 ± 3

Curie temperatures of the phases, listed in Table 4.6, were exclusively measured on single phase samples by means of Magnet-TG. For both series the values show an increase from about 200 °C to 300 °C as Ce is increasingly replaced by Sm. Despite the dependence on the RE-ratio, V does not considerably alter the evolution of T_C. In Figure 4.15, the slope of V-containing samples might be somewhat steeper, however it is hard to call this a fundamental effect.

Thus, concerning the intrinsic quantities, additional V does only affect J_s while H_a and T_C remain largely unchanged.

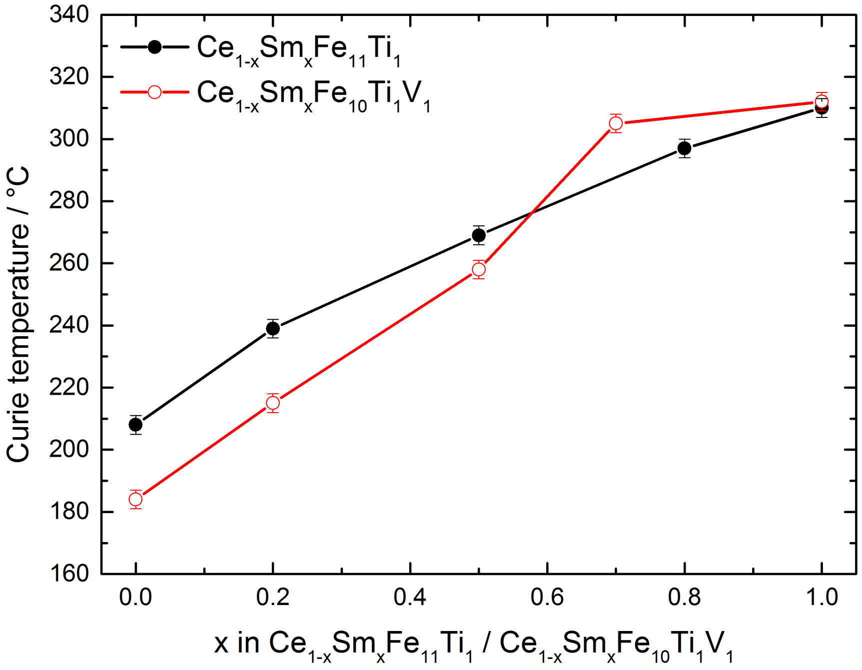

Figure 4.15: Development of T_C with increasing Ce/Sm-ratio for $Ce_{1-x}Sm_xFe_{11}Ti_1$ and $Ce_{1-x}Sm_xFe_{10}Ti_1V_1$.

Extrinsic properties

From the preliminary phase diagram investigations, necessary compositions regarding the requirements of single phase samples were derived. Due to differences compared to the nominal RE-content, the influence of the latter on the obtainable $H_{c,max}$ and the associated evolution of coercivities, after recrystallization of intensively milled powders, was initially checked. The measured values for $Ce_{0.5}Sm_{0.5}Fe_{10}Ti_1V_1$ with 7 at.%, 8 at.%, 9 at.% and 10 at.% are presented in Figure 4.16 with logarithmic scale on the ordinate (see Table A.2 in the appendix for detailed compositions).

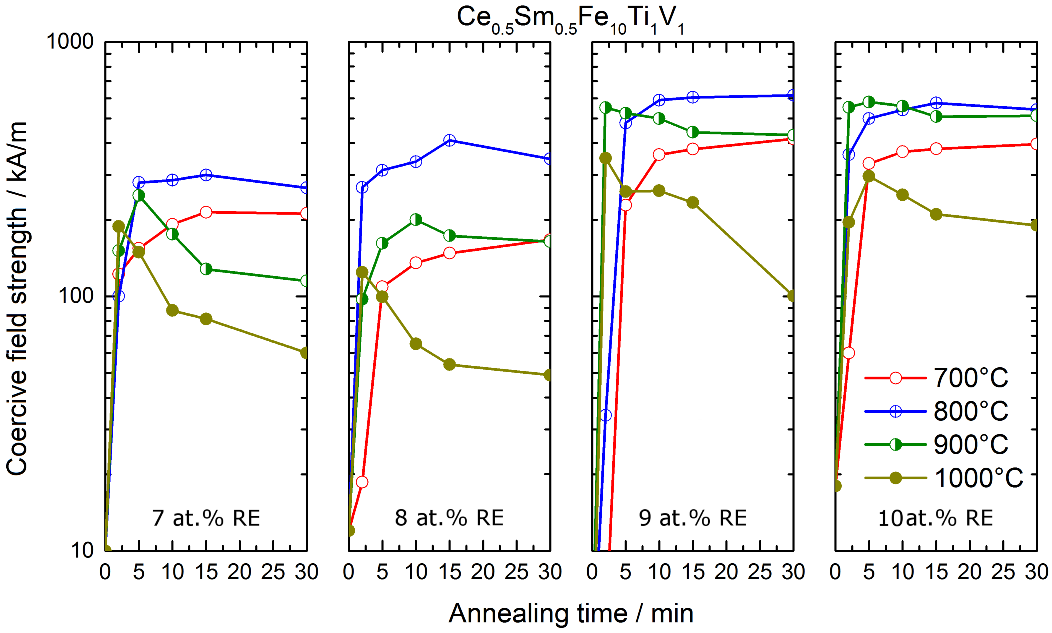

Figure 4.16: Coercivities measured on intensively milled and subsequently annealed $Ce_{0.5}Sm_{0.5}Fe_{10}Ti_1V_1$-powders with different RE-contents.

The principal development of H_c is similar for all RE-contents. Required annealing parameters for $H_{c,max}$ are identical. However, the obtained maxima increase from 7 at.% to 9 at.%.

The powder with 9 at.% RE is the first which exceeds the 8.5 at.% which were found to be actually present in the phase (see Table 4.4). This theoretically permits to form a microstructure without detrimental phases, lowering coercivity, in equilibrium. As known from the exchange spring magnet, the amount of tolerable secondary phase α-Fe in nanocrystalline materials is limited. At some point the main phase is sufficiently well bordered and shielded from each other. Correspondingly, a further increase of the RE-content is not believed to raise $H_{c,max}$ significantly. Indeed, Figure 4.16 presents comparable magnitudes of the relevant values. Note that the Ce-content is marginally raised for the powder with 10 at.% RE.

Figure 4.17 presents diffractograms of the different powders annealed at 1000 °C for 30 min. Due to the fact that the short annealings will never result in equilibrium conditions, the contents of V-containing Fe_2Ti_1 are roughly similar. However, it is especially important to note the predominance of α-Fe in the compositions with understoichiometric RE-content (according to Table 4.4). In accordance with the phase diagram studies, the amount of α-Fe decreases with increasing RE-content and disappears if the elaborated concentration is exceeded. The composition with 9 at.% RE is the first to fulfill this criterion.

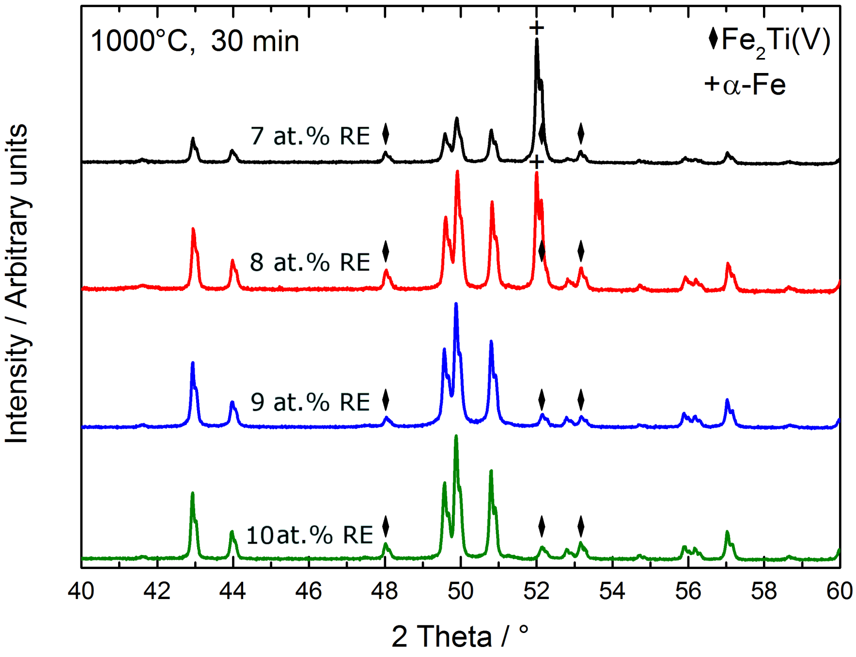

Figure 4.17: X-ray diffractograms of $Ce_{0.5}Sm_{0.5}Fe_{10}Ti_1V_1$-powders with different RE-contents annealed at 1000 °C for 30 min.

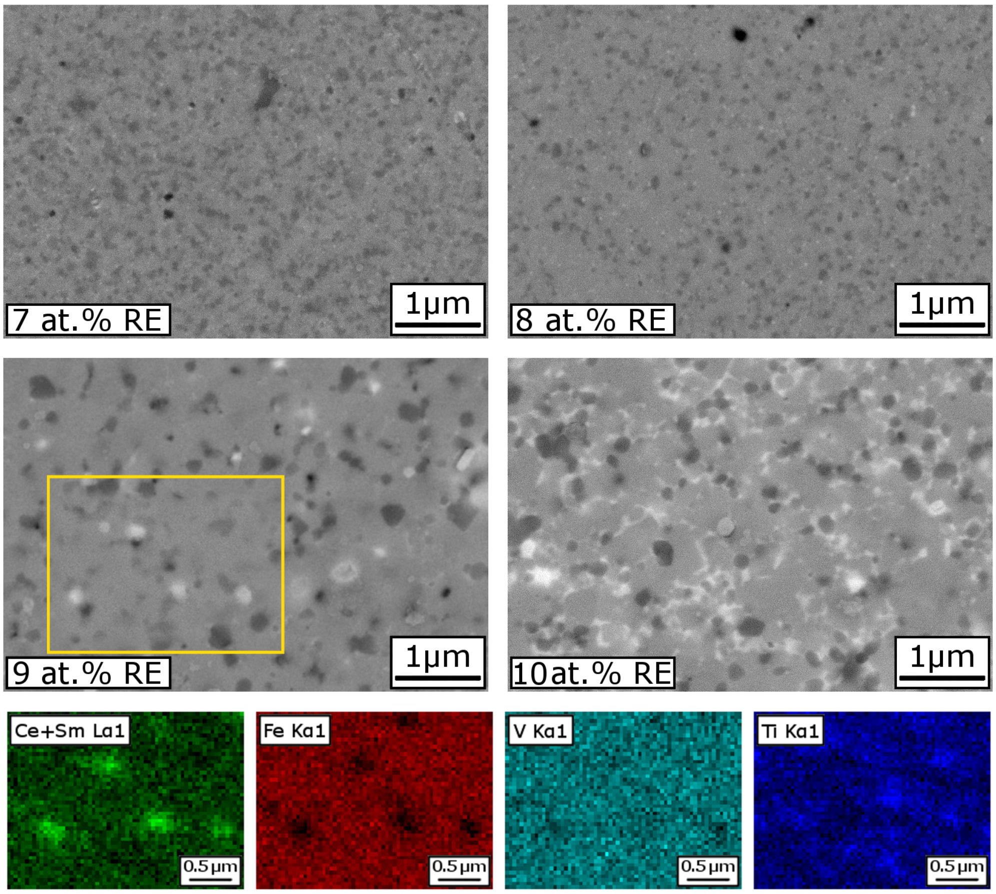

Figure 4.18: Micrographs of $Ce_{0.5}Sm_{0.5}Fe_{10}Ti_1V_1$-powders with different RE-contents annealed at 800 °C for 15 min (top and center). Element maps for the framed area are also provided (bottom).

Micrographs of the considered powders are given in Figure 4.18. The powders were annealed at 800 °C for 15 min which corresponds approximately to the states yielding $H_{c,max}$. The structural features clearly coarsen while it can also be observed that the dark particles become less. For the overstoichiometric compositions, a RE-rich phase occurs which is thought to oxidize quickly in air, causing very weak reflections of Ce_1O_1 and Sm_1O_1 in the prepared samples during the measurement in air. The amount of this phase is especially high for the composition with highest RE-content. It furthermore tends to surround particles of the main phase instead of minimizing interfaces with the latter. Since from 9 at.% RE on, $H_{c,max}$ has not shown to be dependent on the amount of RE-rich phase, the avoidance of detrimental, Fe-based phases is decisive.

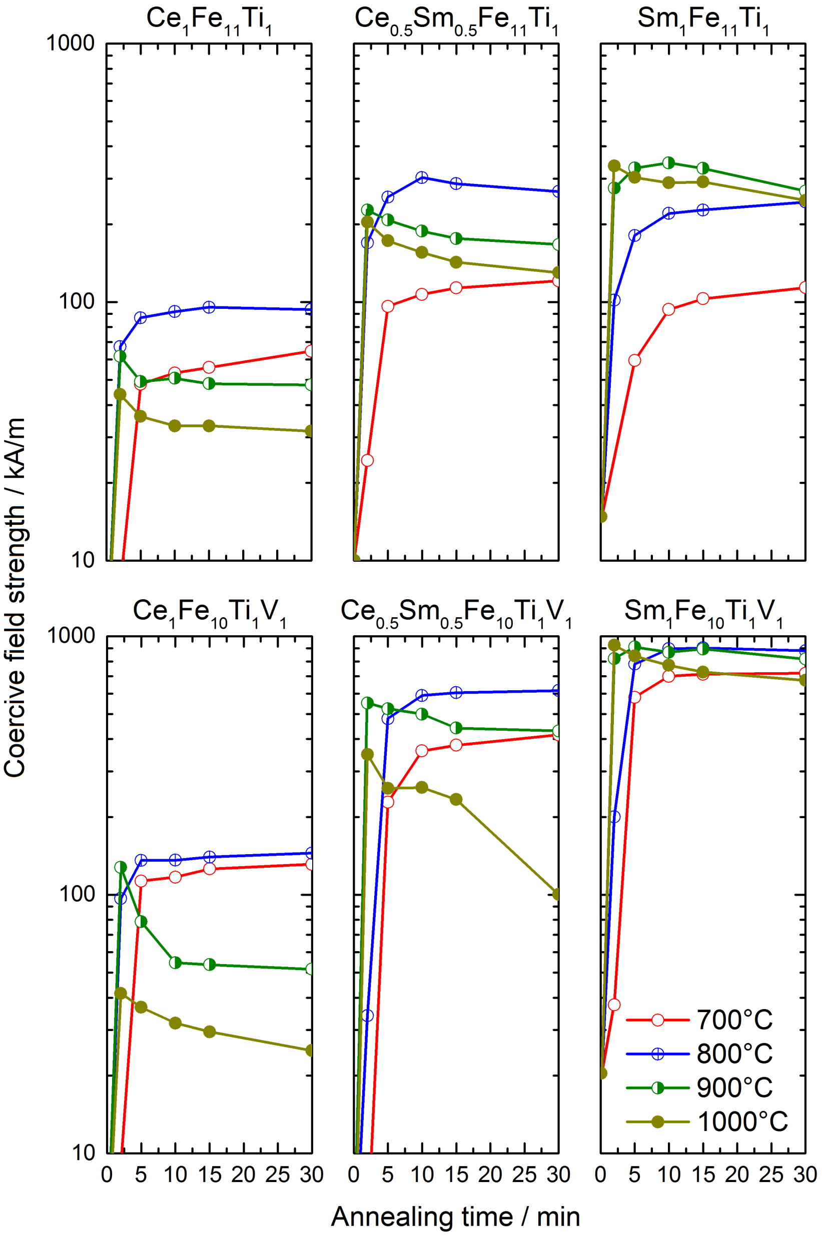

Figure 4.19: Selected coercivities obtained for intensively milled and subsequently annealed $Ce_{1-x}Sm_xFe_{11}Ti_1$- and $Ce_{1-x}Sm_xFe_{10}Ti_1V_1$-powders. The RE-content is slightly overstoichiometric.

The results have shown that the previously determined phase compositions need to be taken into account for the fabrication of nanocrystalline material if the latter is supposed to reveal the maximum potential of the phase in terms of coercivity. As further RE-excesses have little impact, the true $H_{c,max}$ can always be obtained if the RE-content is above the respective limits in Table 4.4. For all Ce/Sm-ratios this has in the following been ensured by an ever overstoichiometric RE-content.

In order to clarify the individual $H_{c,max}$ with main emphasis on the RE-ratio and the role of V, the remaining powder compositions of Table A.2 (see appendix) have been analyzed. A selection of coercivities obtained from annealings of the respective powders are shown in Figure 4.19. The corresponding values of the skipped powders are presented in Figure A.4 (see appendix) together with further, not listed compositions that accidently became understoichiometric, thus showing collectively lower $H_{c,max}$. The values in Figure 4.19 show that differences regarding the employed RE-ratio are even more pronounced than for the previous comparison of under- and overstoichiometric powder compositions. The development of H_c for different annealing conditions shows throughout similar trends. A temperature of 700 °C causes low driving forces and reduced kinetics for the crystallization of the hard-magnetic phase. The evolution of H_c exhibits a gradual increase up to the maximum values, generally obtained for moderate times at 800 °C or 900 °C. Despite initial peak values, higher temperatures generally exceed the optimal state and lead to a decrease.

It can be noticed that the Sm-content increasingly raises the temperature which yields $H_{c,max}$. Furthermore, associated conditions for $Sm_1Fe_{11}Ti_1$ and $Sm_1Fe_{10}Ti_1V_1$ are similar to these of $Sm_1Fe_{10-x}Al_xMo_2$ (see Section 4.1.3). Characteristic $H_{c,max}$ for the presented RE-ratios without (with) V are 95 kA/m (145 kA/m), 303 kA/m (617 kA/m) and 345 kA/m (924 kA/m), respectively. Strikingly, the V-containing samples possess throughout superior coercivities.

Figure 4.20 summarizes the determined $H_{c,max}$ for various compositions. The coercive field strengths of $Ce_{1-x}Sm_xFe_{11}Ti_1$ increase with Sm-content what in principle agrees with literature, even though the rise shows another quantitative dependency [28]. The values of V-containing samples are raised threefold for high Sm-contents or by a factor of 1.5 for RE=Ce, showing that the beneficial effect of V is particularly dependent on the RE-ratio. These considerations define a kink approximately at x=0.5 which is already present for $Ce_{1-x}Sm_xFe_{11}Ti_1$ but amplifies under the presence of V. It is especially interesting that more than 600 kA/m can be obtained for the $Ce_{0.5}Sm_{0.5}Fe_{10}Ti_1V_1$-powder. The similarities of compositions possessing equal amounts of both RE with those on the Sm-rich end indicate that Ce-based phases perform especially poor in terms of coercivity.

The V-free and -containing powders reach coercivities that deviate from the linear trend of their intrinsic counterparts (see anisotropy fields in Table 4.6). For V-free phases the values correspond to roughly 4 % to 5 % of the respective H_a. Here, the kink does not noticeably affect the factor by which the extrinsic quantity is reduced. The presence of V, however, causes the coercivity to reach values of about 7 % (Ce-rich) or even 11 % (Sm-rich) of the anisotropy field. That emphasizes the role of V. Assuming the classical limits of Brown's paradox, even the drastically increased H_c of $Sm_1Fe_{10}Ti_1V_1$ might have potential for further improvement ($0.25 \cdot H_a$ to $0.3 \cdot H_a$).

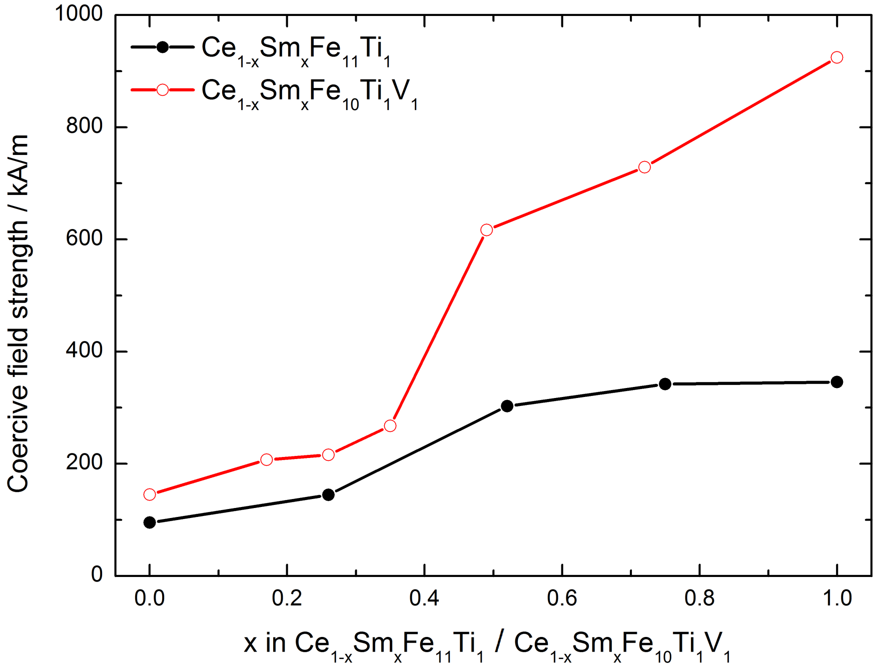

Figure 4.20: Maximum coercive field strengths obtained from annealings of intensively milled $\mathrm{Ce_{1-x}Sm_xFe_{11}Ti_1}$- and $\mathrm{Ce_{1-x}Sm_xFe_{10}Ti_1V_1}$-powders.

The determined temperature coefficients β (see Equation 3.2 and Table A.3 in the appendix) of the annealed powders fall in the range of -0.4 %/°C to -0.7 %/°C, thus being comparable to Nd-Fe-B-magnets [61, 63, 73]. Differences between V-free and -containing phases are generally negligible but tend to be raised for the latter series. The composition with equal contents of Ce and Sm shows slightly lower β.

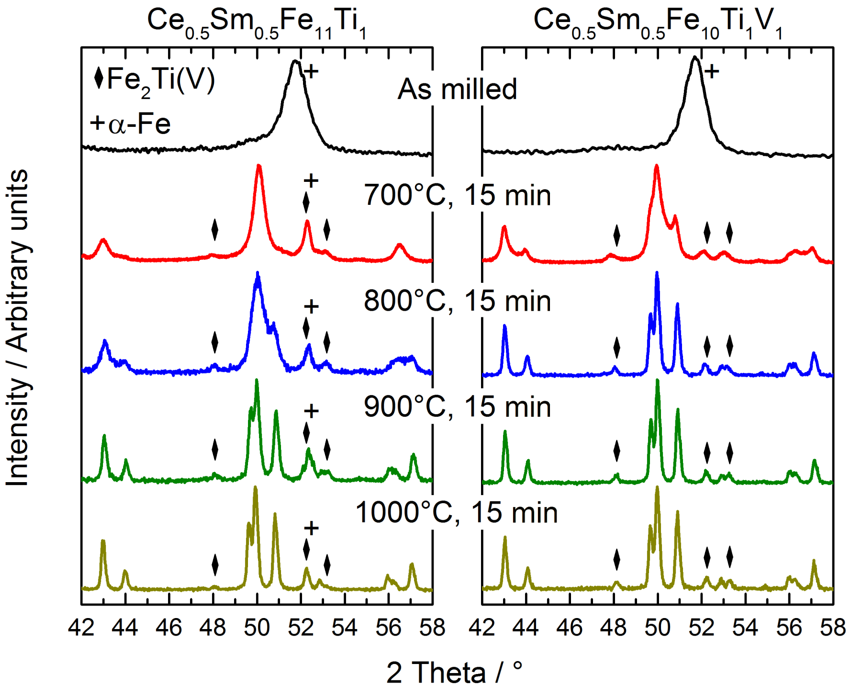

Figure 4.21: X-ray diffractograms of intensively milled $\mathrm{Ce_{0.5}Sm_{0.5}Fe_{11}Ti_1}$- and $\mathrm{Ce_{0.5}Sm_{0.5}Fe_{10}Ti_1V_1}$-powders annealed at selected conditions.

From the present results it is concluded that the beneficial effect of V is related to an advantageous microstructure formation and therefore extrinsic. This also agrees with literature reports where microstructural benefits are discussed for V [17] (compare Section 2.3.2). The XRD-patterns from Figure 4.21 can directly be associated with the data points in the very center of Figure 4.19 (15 min). It stands out that V significantly speeds up the crystallization (definedness of reflections for equal annealings). This is true for all temperatures and all RE-ratios. Reflections of representatives yielding $H_{c,max}$ ($\approx$ 800 °C, 15 min) are very different and in both cases not yet very well-defined. The nanocrystalline structures are differently fine-grained.
The evolution of refined crystallite sizes is plotted in Figure A.5 (see appendix). Sizes associated with $Ce_{0.5}Sm_{0.5}Fe_{10}Ti_1V_1$ show a fast initial increase to maximum sizes around 250 nm which remind of a n-th-root-shaped behavior. However, the increase cannot satisfy $n \leq 2$ due to the damped increase from 15 min on. The V-free material yields significantly smaller crystallite sizes and an accordingly flattened increase. The presence of small secondary phase particles in the micrographs of Figure 4.18 suggests, like for the previous material system Sm-Fe-Mo-Al, that Zener pinning is present [193]. These particles can further be detected in the diffractograms as a small amount of a Fe_2Ti_1(V)-related structure.
Moreover, the closer investigation of Figure 4.21 shows α-Fe as an additional phase in the V-free material. It is particularly present for low annealing temperatures and might contribute to the Zener pinning in $Ce_{0.5}Sm_{0.5}Fe_{11}Ti_1$. It does not occur in the V-containing powder with very similar RE-content and marks a further difference regarding the formation of the 1:12-phase from the as-milled state. As α-Fe is undesirable, this is interpreted as another reason for the beneficial effect of V with respect to obtainable coercivities.

For selected RE-ratios, nanocrystalline $Ce_{1-x}Sm_xFe_{10}Ti_1V_1$-material was complementary produced by melt-spinning at variant wheel speeds. Coercivities of the considered compositions - in the as-spun states and after suitable annealings - are presented in Figure 4.22. Favorable parameters for the heat treatments are adopted from the intensive milling experiments (see Figure 4.19). The as-spun coercivities show maximum values at 30 m/s. Higher wheel speeds lead to relatively low H_c, just like it is the case for 25 m/s and 20 m/s. Annealing experiments are limited by the rather small amount of receivable material per run. It is noteworthy that the ribbons can achieve similar values after annealing, independent of the wheel speed at which they were produced (even underquenched). This is contrary to classic expectations based on Nd-Fe-B [210–214]. The highest coercivities are especially exhibited by the samples annealed at 800 °C. The obtainable values do not fully reach the respective $H_{c,max}$ of the milling experiments (see Figure 4.19). This might be due to the confined set of production- and annealing parameters. However, available reports for melt-spun $Sm_1Fe_{10}Ti_1V_1$ state even inferior maximum coercivities [17]. Though both routes yield nanocrystalline material, melt-spinning and intensive milling are different approaches with complementary but unequal products. The prevailing agreement still affirms the presented results for different sample compositions.

An advantage of the rapid quenching technique is that the formation of α-Fe can potentially be suppressed [61, 215, 216]. Diffractograms of the characterized melt-spun ribbons are presented in Figure 4.23. Even though there was no α-Fe observed for the corresponding (V-containing) intensively milled powders, associated reflections occur occasionally in the measurements of the ribbons. Besides the observed Fe_2Ti_1(V), α-Fe is increasingly present in the as-spun state or after annealings at 800 °C.

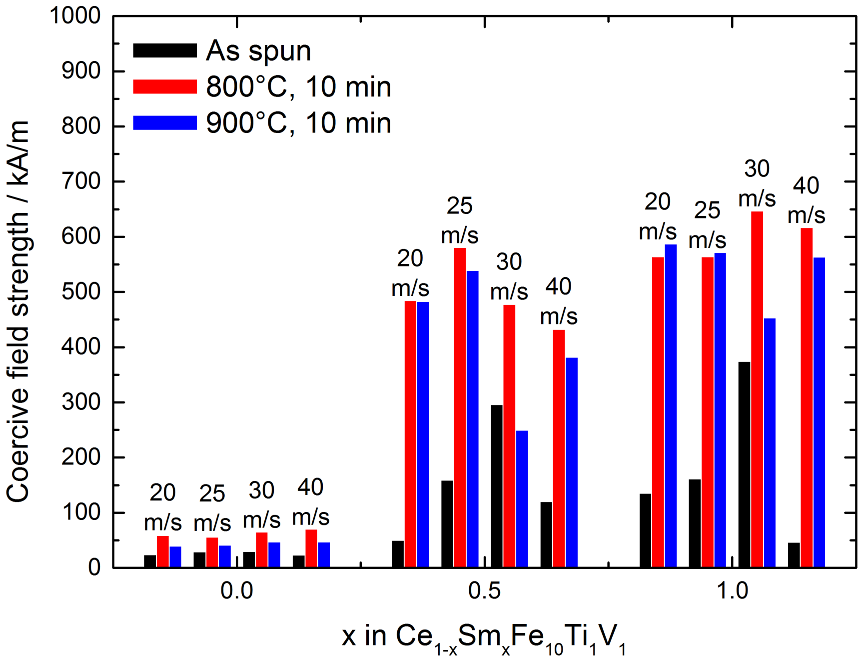

Figure 4.22: Coercive field strengths achieved by melt-spinning of V-containing alloys with different RE-ratios and slightly overstoichiometric RE-content. The different wheel speeds are indicated.

Regarding crystallinity, it can be concluded that both, increasing temperatures and decreasing wheel speeds, cause reflections of the 1:12-phase to become more defined. Generally, deviations to the argumentation and perceivable trends can be attributed to the peculiar viscosity and processability of especially Sm-based melts. Due to the limited sample set and resembling absolute values, it is hard to judge, which structural characteristics are favorable for high coercivities.

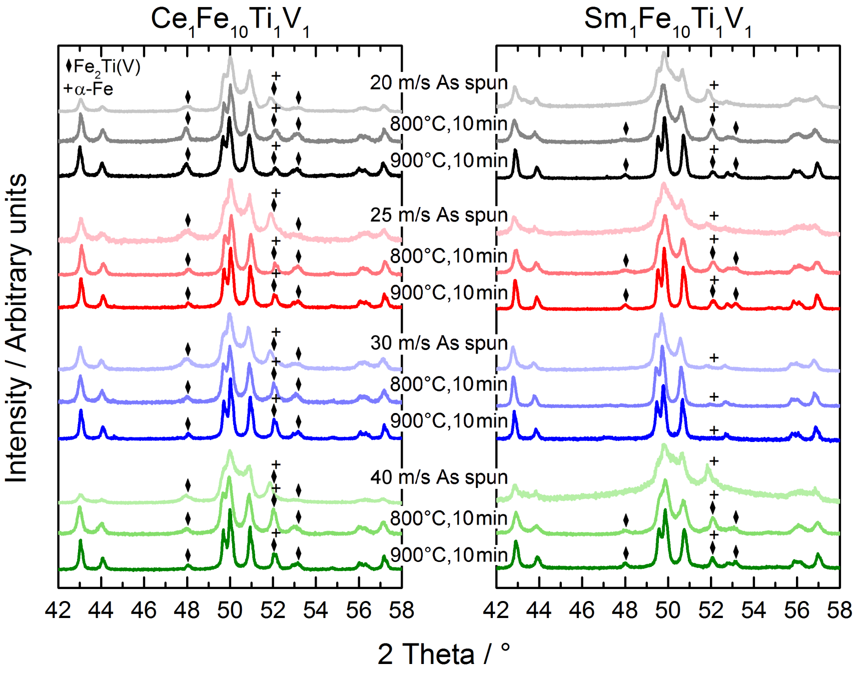

Figure 4.23: X-ray diffractograms of as-spun and annealed $Ce_1Fe_{10}Ti_1V_1$- and $Sm_1Fe_{10}Ti_1V_1$-melt-spun ribbons produced at different wheel speeds.

The discussed trend of as-spun coercivities needs to originate from an advantageous crystallization of the hard-magnetic phase. In contrast to overquenched ribbon material (≥ 30 m/s), low wheel speeds are assumed to cause too large grains which are not predicted to improve H_c substantially by subsequent annealings. This is in contradiction with the results of this work. Based on the collected data and remembering that V has shown to promote and tolerate larger crystallites in the milled powders, it is suggested that heat treatments have an influence on the distribution and/or shaping of involved phases. This goes beyond simple grain growth mechanisms. Thus, comparatively large grains can likewise improve H_c of their ensemble. Together with the final results from comparisons of obtainable $H_{c,max}$ with the corresponding H_a, this provides evidence for improved (or improvable) microstructures when V is present.

4.2.4 Bulk magnet

In the following section, melt-spun ribbons have been crushed, hot-pressed and die-upset to produce a bulk magnet based on the previously treated $Ce_{0.5}Sm_{0.5}Fe_{10}Ti_1V_1$-phase. The latter is promising because of the high Ce-content while obtainable $H_{c,max}$ are considerably high. During the process, different parameters have been employed and the material has been characterized for all relevant stages. Although the presence of a liquid phase is not absolutely necessary for the analogous production of textured, nanocrystalline Nd-Fe-B-magnets, it is required to obtain crack-free products [78, 82]. In the material system of interest, RE_1Fe_2 (see Table 4.3) could potentially account for liquid components. For (globally) equal amounts of Ce and Sm, that phase has, however, shown to be preferentially Ce-rich, causing certain problems (see Figure 4.10). Required process temperatures would be approximately 100 °C above that, specified for the present experiments (800 °C). For these reasons, the specially made ribbon material has an explicit content of 0.5 at.% Ga (see Table 3.3). This additional element is supposed to form RE_3Ga_1 whose Ce-rich representatives contribute to a liquid phase during the hot-pressing. Indeed, differential scanning calorimetry (DSC) indicates a weak signal slightly above 500 °C for the as-spun ribbon material. Furthermore, Ga is known to increase H_c, modificate the grain boundary phase of Nd-Fe-B and promote the hot-forming properties so that minor additions are supposed to improve the processability [17, 63, 81, 161, 162].

Hot-pressed magnet

The starting ribbon material has proven to be promising for the production of bulk magnets via hot-pressing. Relevant parameters are given in Section 3.1. The targeted processing temperature is comparable to that, typically used for Nd-Fe-B. Figure 4.24 presents microsections of the obtained hot-pressed magnet and EDX-maps for the involved elements of the dense ($> 0.98 \cdot \rho_{XRD}$, see Table 4.5) product. The images, obtained parallel to the pressing direction, are representative for the magnet volume. For low magnifications, the former ribbon pieces can still be identified. The latter are separated from each other by more or less large areas of bright phases. Perpendicular microsections show the result of the axial force application in such a way that the larger areas of RE-rich phases appear compressed and in a stacked manner. This originates from the fact that the platelet-shaped pieces preferentially lie on their flat sides.

A closer investigation of the bright phases at particularly large spots confirms the presence of the intended RE_3Ga_1 (Ce/Sm=2:1). Furthermore, RE_1Fe_2 (Ce/Sm=5:1) can be found close by. In principle, that phase is reported to be stable throughout the whole temperature range of the process [200]. Both of the bright secondary phases have considerable Ce-contents and occur on large as well as short lengthscales (same elemental contrast) as non-continuous areas on the former ribbon surfaces. Despite rather smooth interfaces with the remaining ribbon volume, they are not continuous but contain dark particles or are separated by the direct contact of former ribbons where predominantly the hard-magnetic phase is present.

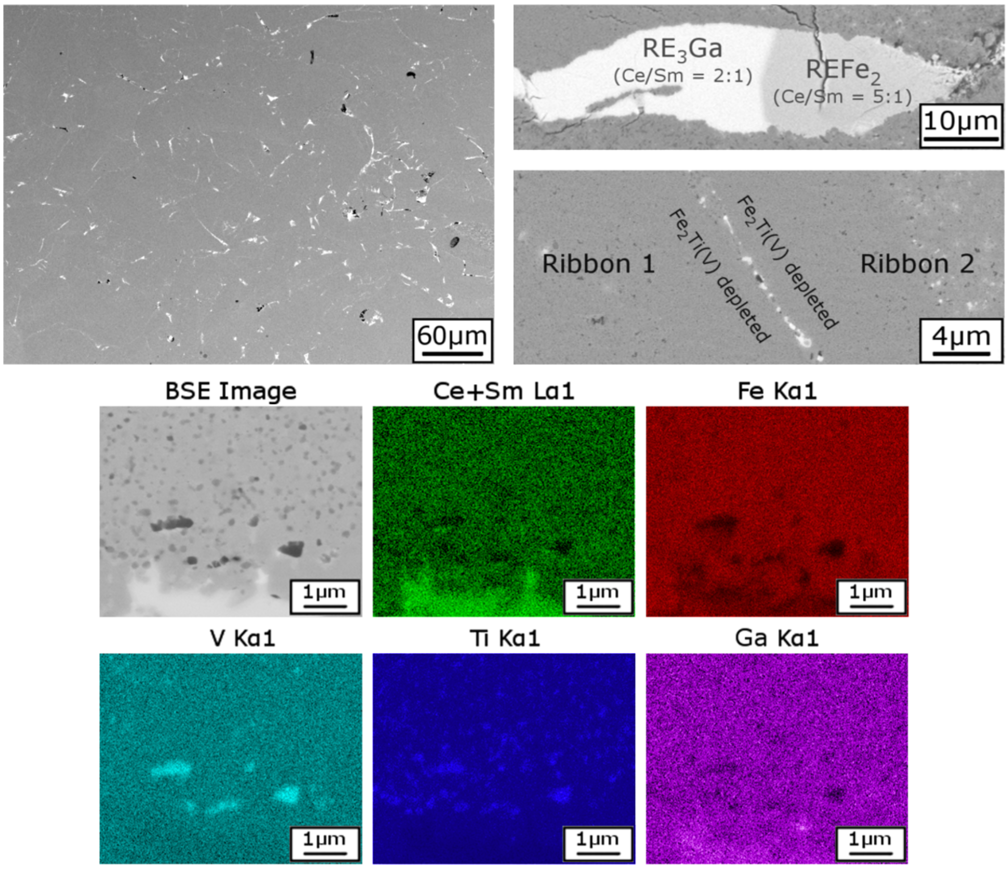

Figure 4.24: Micrographs of the hot-pressed magnet with present phases in the bulk volume and at the ribbon boundaries (top). Individual EDX-maps for the involved elements in the ribbon interior are also provided. The bright phase at their lower end is situated at a ribbon boundary (bottom).

Independent of the observed direction, the principal bulk volume shows the same characteristics (and relevant lengthscales) as the as-spun ribbons. As such, it also resembles the associated, annealed powder in Figure 4.18. The (Ga-containing) 1:12-phase forms the matrix which homogeneously contains darker particles. These show different grey contrasts and are, in agreement with the presented results, presumably assignable to Fe_2Ti_1(V). The element maps in Figure 4.24 support this result and do further pronounce the variance regarding the Ti- and V-content. Consistently, RE and Ga show strong signals within the bright phase and are not observed in the discussed secondary phase. The described Fe_2Ti_1(V)-particles, close to (or within) the ribbon boundaries, are especially dark and large. At the same time the usual greyish particles are depleted in this region. While the size of these abnormal, large particles can be explained by enhanced diffusivity in the boundary, where also liquid phases are believed to occur, their contrast can be attributed to slight amounts of impurity B. The latter is particularly found in the stated, especially V-rich, particles and supposed to originate from the crucible coating where the primary alloy has been produced in. A negligible content of the light element B has also been confirmed by ICP-OES.

Figure 4.25 presents the magnetic characteristics of the utilized ribbon material in the as-spun and annealed state compared to the response of the hot-pressed magnet. Consistent with the results from Figure 4.22, the coercivity of the Ga-containing melt-spun ribbons can significantly be tuned by a short heat treatment. The exemplary annealing which corresponds in time and temperature to the conditions of the hot-pressing process, leads to a doubling of H_c. A comprehensive compilation of the coercivities for annealed Ga-containing ribbons is given in Figure A.6 (see appendix). Accordingly, the hot-pressed magnet exhibits a considerable coercive field strength of about 425 kA/m after processing. This emphasizes the method's potential to maintain and realize strong coercivity of 1:12-phases in the bulk state. In this context, literature indicates that sintering falls short [17, 152] (compare Section 2.3.2). It is believed that H_c can further be optimized by variations of the hot-pressing process.

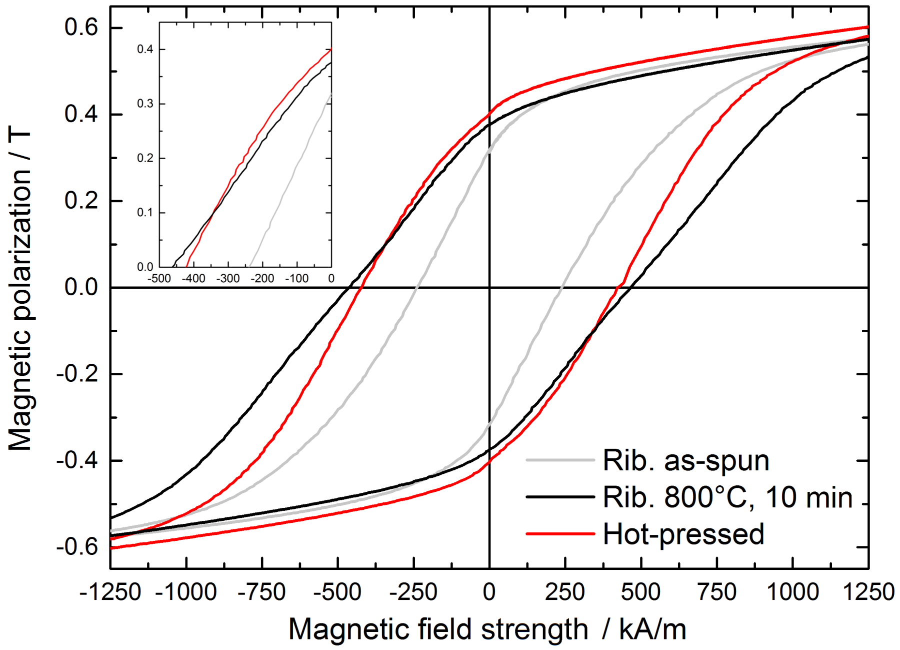

Figure 4.25: Full hysteresis loop (PPMS) of the hot-pressed magnet compared to those of the as-spun and annealed ribbon material. The inset shows a magnified section of the demagnetization curves.

Polarization values on the ordinate are calculated from the PPMS-raw data using the exact masses and the estimated density ρ_{XRD}. Neighboring phases and grain boundaries are not taken into account. The presented measurements show that the application of heat also improves the remanence of the nanostructure. The hot-pressed magnet retains with 0.4 T roughly 40 % of its saturation value (J_s=0.95 T, see Table 4.6), assuming that the latter is not significantly altered by the small Ga-content in the material. Due to the isotropic nature of the produced magnet, this is very close to the predictable maximum of $J_r = 0.5 \cdot J_s$. The measured maximum energy product of the hot-pressed magnet is roughly 25 kJ/m^3. Despite the need to improve the rectangularity of the demagnetization curve, this value amounts to more than 55 % of the expectable $(BH)_{max}$. Compared to a fully anisotropic magnet, the present maximum energy product equals to 1/7 $\cdot$ $(BH)_{max,theo}$. It can be concluded that hot-pressing successfully transfers the observed extrinsic properties of the nanocrystalline material to the bulk state. The well-founded choice of parameters yields a bulk magnet with reasonable properties already in early attempts.

Die-upset magnet

So far, a relatively low absolute remanence has been measured for the hot-pressed 1:12-magnet. Reconsidering the processing of anisotropic, nanocrystalline Nd-Fe-B-magnets (see Section 2.1.1), it is worthwhile to understand the hot-pressed sample as a precursor and to further investigate a possible texturing. Die-upsetting has been tested at rates ranging from $0.001\,\mathrm{s}^{-1}$ over $0.002\,\mathrm{s}^{-1}$ to $0.01\,\mathrm{s}^{-1}$ (see Section 3.1) of which especially the last is characteristic for typically used values in the case of Nd-Fe-B [61, 78, 82, 217]. The corresponding experiments were successful and did not be accompanied by any problems that would go beyond the aspects mentioned below. The sample surfaces are rather smooth with only few radial cracks in the outer zone (compare Figure 3.2).

Figure 4.26 shows identically prepared microsections of the samples which have been processed with lowest and highest deformation rate, respectively. The secondary electron images allow to compare surface topologies. Especially the sample, which has been die-upset with a rate of $\dot{\varphi} = 0.01\,\mathrm{s}^{-1}$, shows a conspicuously bumpy finish that is associated with residual stresses. This also agrees with the fact that the press approached its power limit multiple times during the deformation. However, the sample did not show severe cracks or peculiarities except a minor porosity which has not been noticed for the slowly deformed counterpart. In general, further features of the die-upset samples resemble the observed results of the hot-pressed magnet in Figure 4.24.

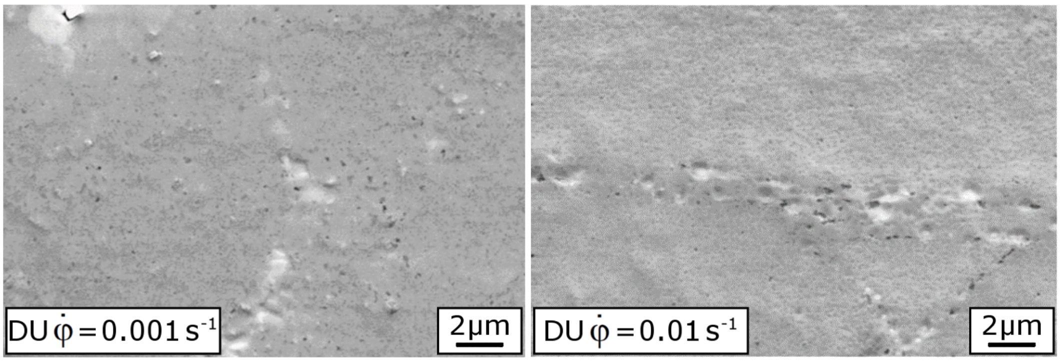

Figure 4.26: Secondary electron images of the magnets die-upset with $\dot{\varphi} = 0.001\,\mathrm{s}^{-1}$ (left) and $\dot{\varphi} = 0.01\,\mathrm{s}^{-1}$ (right). The samples were similarly prepared to meet the requirements for EBSD-analysis.

XRD confirms the visual observation that the average $\mathrm{Fe_2Ti_1(V)}$ particle size ($\approx 150\,\mathrm{nm}$) and number is not significantly affected from the ribbons' as-spun state towards the die-upset magnet. High magnifications of the latter do not allow the further assessment of the main phase grains since especially no bright phases can be seen to separate the individual grains. Therefore, the die-upset magnet does not reveal eventual differences compared to the hot-pressed pendant.

Regarding the objective of die-upsetting to induce a texture, it is especially important to visualize the grains and identify their orientation with respect to the macroscopic direction of applied force. Since the prepared microsections have shown to be unsuitable for proper EBSD-mapping (distorted images) the corresponding analysis has been performed by TKD on specially prepared lamellas. This allows for better spatial resolution and more relaxed sample surfaces.
Figure 4.27 shows the detailed microstructure of the sample which has been die-upset with the slowest rate (0.001 s^{-1}). The underlying lamella is representative for an observation of the microstructure parallel to the deformation direction. Besides the small SEM-image of the investigated area, the TKD-data is split in order to account for the two main crystalline phases, essentially being present in the bulk volume ($Ce_{0.5}Sm_{0.5}Fe_{10}Ti_1V_1$(Ga) and Fe_2Ti_1(V)). Based on the provided crystal structures (and related parameters), previously derived by XRD- and ND-measurements, it is possible to assign the recorded Kikuchi-patterns to the respective grains. The 1:12-grains usually have sizes of 200 nm to 300 nm. The successive increase of the crystallite size ($\leq$ grain size) from about 30 nm (as-spun ribbons) over 50 nm (hot-pressed magnet) to roughly 65 nm (die-upset magnet), determined by XRD-refinements, confirms the slight growth of the grains during the subsequent exposures to heat.

The individual distribution of Fe_2Ti_1(V) in the generated TKD-maps differs from the one in the top view (SEM) of the lamella. This in accordance with literature reports and can be attributed to the fact that diffraction data corresponds to the bottom side of the lamella (with thickness greater than average grain size) where electrons leave the irradiated material [218].

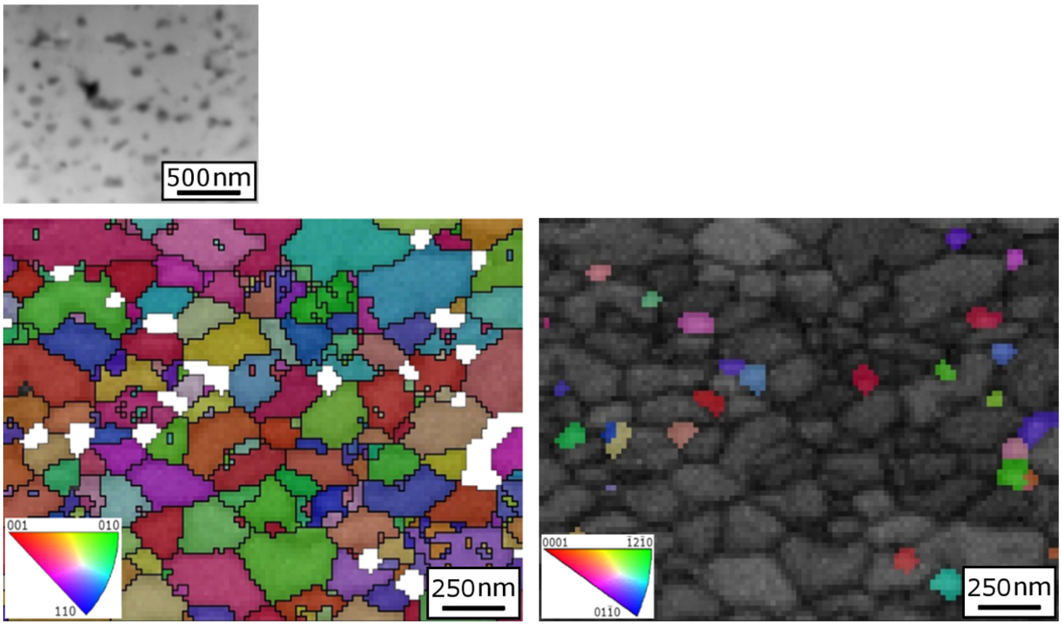

Figure 4.27: Images based on the TKD-data recorded for the slowly die-upset sample ($\dot{\varphi}$ = 0.001 s^{-1}) parallel to the deformation direction. Stored patterns are translated to orientational information for the 1:12-matrix phase (left) and the Fe_2Ti_1(V)-particles (right).

Coloring of the inverse pole figure refers to the z-component of the tetragonal 1:12-phase (hexagonal Fe_2Ti_1(V)-phase) since it is desirable that especially the hard-magnetic grains are preferentially aligned with respect to that axis after die-upsetting. Based on the presented results, random orientations of the corresponding grains indicate that this is not the fact and, thus, no texturing could be achieved. Moreover, no preferred orientation has been established for the

Fe_2Ti_1(V)-particles, which have not notably changed throughout the processing. Presumably, there is also no significant relationship to adjacent particles of different phases.

An equivalent assessment for the magnet, which has been die-upset with the considerably faster deformation rate of $0.01\,\mathrm{s}^{-1}$, shows that the presented findings are independent of $\dot{\varphi}$. With respect to a mechanistic point of view, it is important to evaluate the shape of the magnet's grains after die-upsetting. For this purpose the microstructure has been analyzed parallel and also perpendicular to the applied force. Accordingly, two lamellas have been prepared. Figure 4.28 illustrates the considered SEM-sections of both, together with qualitative TKD-maps as well as colored ones which reveal the orientations of the single grains. From the comparison, no systematic differences can be concluded. The equi-sized grains are randomly orientated as also observed for the slowly-deformed counterpart. Merging the results of TKD-analyses parallel and perpendicular to the applied stress, it is concluded that grains stay predominantly globular without noticeable effects of the deformation. This excludes the appearance of any effects that would come along with a relevant shape anisotropy. Due to the discussed stresses (compare Figure 4.26), indexing of the grains is slightly more defective than compared with the pattern in Figure 4.27. The speckled coloring of grains is due to pseudo-symmetry [219].

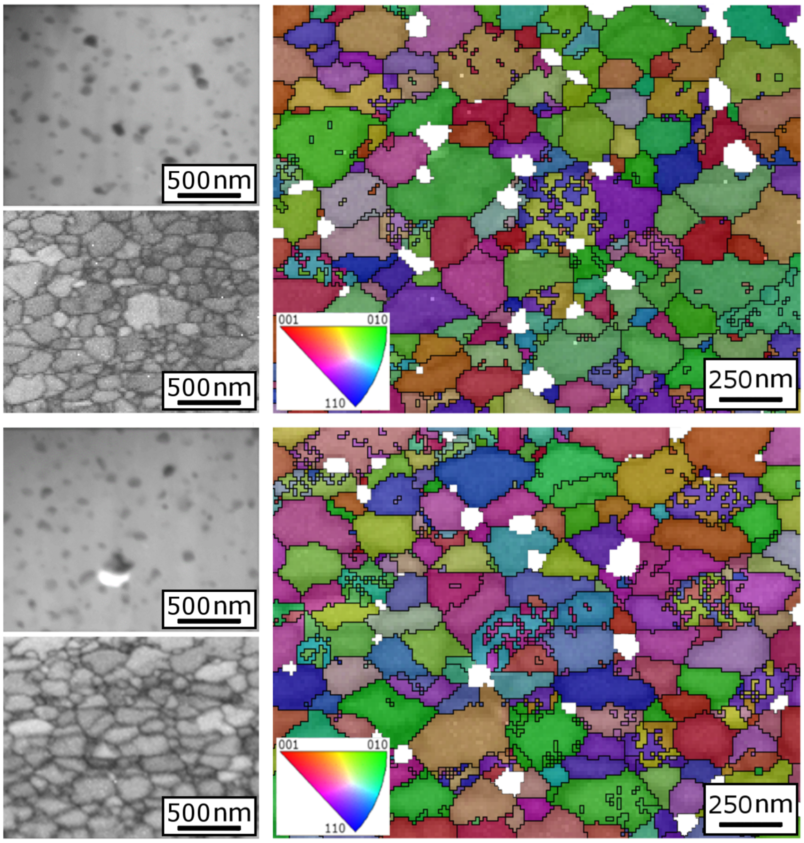

Figure 4.28: Images based on the TKD-data recorded for the rapidly die-upset sample ($\dot{\varphi} = 0.01\,\mathrm{s}^{-1}$). Orientational information for the 1:12-matrix phase are provided parallel (top) and perpendicular (bottom) to the deformation direction.

The prevailing independence of the microstructure throughout the different processing steps is largely supported by the respective X-ray diffractograms. The patterns in Figure 4.29 also reflect the similarity of microsections, obtained parallel and perpendicular to the deformation direction. In order to judge this, cubes have been prepared from the cylindrical magnets. Reflections of Fe_2Ti_1(V) are throughout observed with low intensities and as only appreciable secondary phase besides the hard-magnetic main component. No additional phases, especially Ga-based, can be identified.

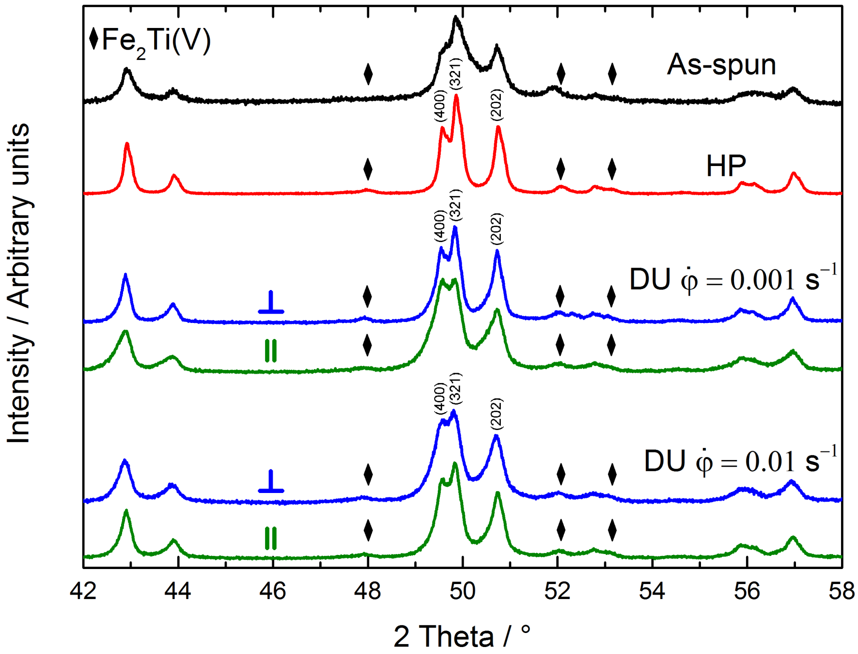

Figure 4.29: Comparison of XRD-patterns for the as-spun ribbon material as well as hot-pressed and die-upset magnets. The latter have been analyzed parallel and perpendicular to the deformation direction. The triplet reflections which emerge from the (400)-, (321)- and (202)-lattice planes are indicated.

The detailed investigation shows that bulk magnets exhibit more defined reflections than ribbons in the as-spun state. This is due to the previously stated increase of grain size after the heat-assisted processing steps. The representatives produced at different $\dot{\varphi}$ do not significantly differ among each other. Furthermore, diffractograms of the die-upset magnets are independent of whether surfaces parallel or perpendicular to the deformation direction are investigated. This pronounces the isotropic character which is contradictory to a successful texturing. It is noteworthy that all diffractograms from die-upset samples tend to show an elevated intensity of the (400)-reflection and a lowered intensity for the (202)-reflection (triplet around 50 °2θ). With the given unit cell and the previously presented results, that can only be explained by a statistically higher amount of (100)-like planes. This speaks for a slightly preferred growth of the grains parallel to the c-axis for the prevailing conditions. Considering the TKD-maps of Figure 4.27 and Figure 4.28 again, it seems that particles with out-of-plane c-axes (purely red particles) are indeed smaller than the average particle. Additionally, Figure A.7 shows an EBSD-image of a ribbon that has been annealed for 150 h at 1000 °C (see appendix). This was meant to possibly yield a whisker-like image, indicating different growth velocities along the a- and c-axis, respectively. Despite the small size of the section, red particles appear again comparatively small. All indices suggest a weakly pronounced effect which does not contribute to an effective texture, though.

Complementary to Figure 4.25, hysteresis loops of the die-upset magnets are presented in Figure 4.30. The measurement of the hot-pressed precursor is added for comparison. The measurements parallel to the applied force (green) suggest a decrease of J_r after die-upsetting. This, and especially the absence of a desired increase, is in accordance with the previously presented results. Coercive field strengths are comparable to the value for the hot-pressed magnet. They tend to increase slightly from approximately 360 kA/m to 475 kA/m as the deformation rate is raised. As a result, the respective $(BH)_{max}$ are reduced by up to 5 kJ/m^3.

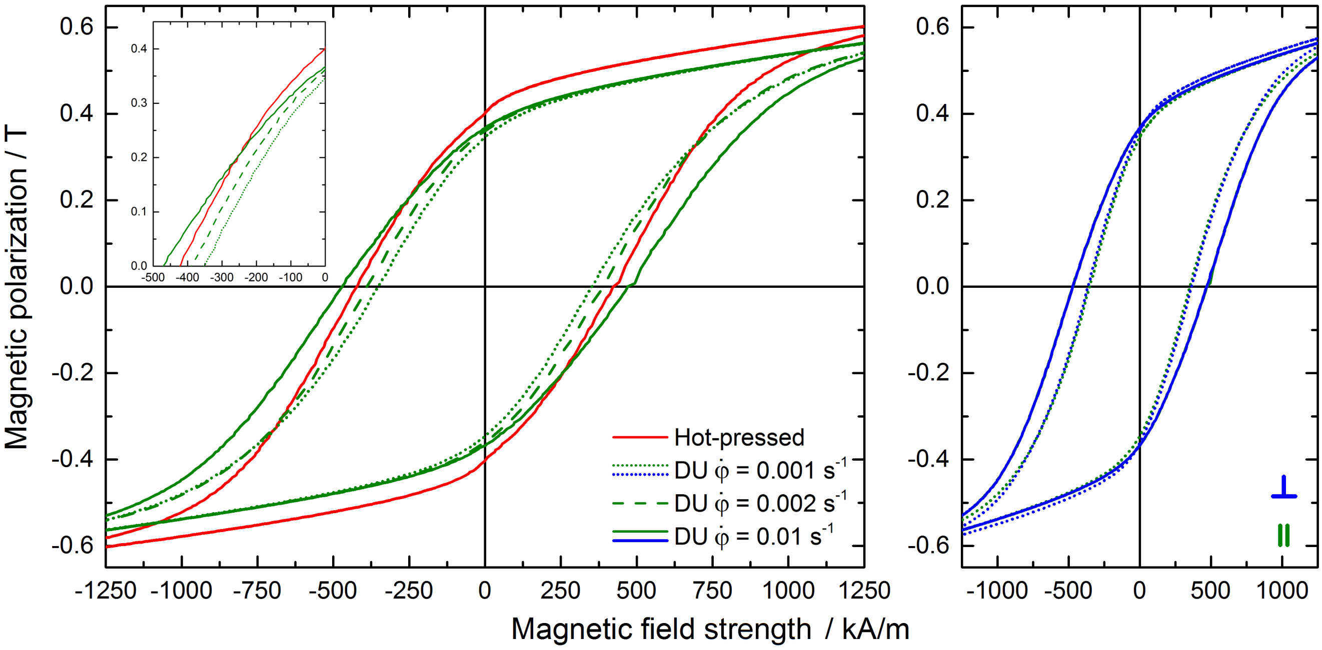

Figure 4.30: Magnetic characterization of the die-upset magnets (hot-pressed precursor included). The inset shows a magnified section of the demagnetization curves (left). A separate plot compares hystereses parallel and perpendicular to the deformation direction (right).

The underlying sample cubes have also been measured perpendicular to the deformation direction and compared in a separate plot with the corresponding measurements parallel to the applied force. There are definitely no differences for the presented samples. The representatives with $\dot{\varphi} = 0.001\,\mathrm{s}^{-1}$ and $\dot{\varphi} = 0.01\,\mathrm{s}^{-1}$ have identical hystereses.

All findings unanimously indicate that, for the investigated range of parameters, it is not possible to texturize the nanocrystalline material by die-upsetting. Still, hot-pressed and die-upset ($\dot{\varphi} = 0.01$) representatives have been characterized regarding their temperature stability. For both magnets, Figure 4.31 shows the developments of B_r and H_c with increasing temperature. The associated coefficients derived from the consecutive measurements are also presented (see also Equation 3.1, Equation 3.2 and Table A.3 in the appendix). Like for the intensively milled and annealed powders, α and β are in a range which is typical for Nd-Fe-B. Both, remanence and coercivity show a better stability with elevated temperatures for the hot-pressed magnet. The latter, thus, excels the apparently weaker performance with regard to β, determined for the powder sample with similar contents of both RE.

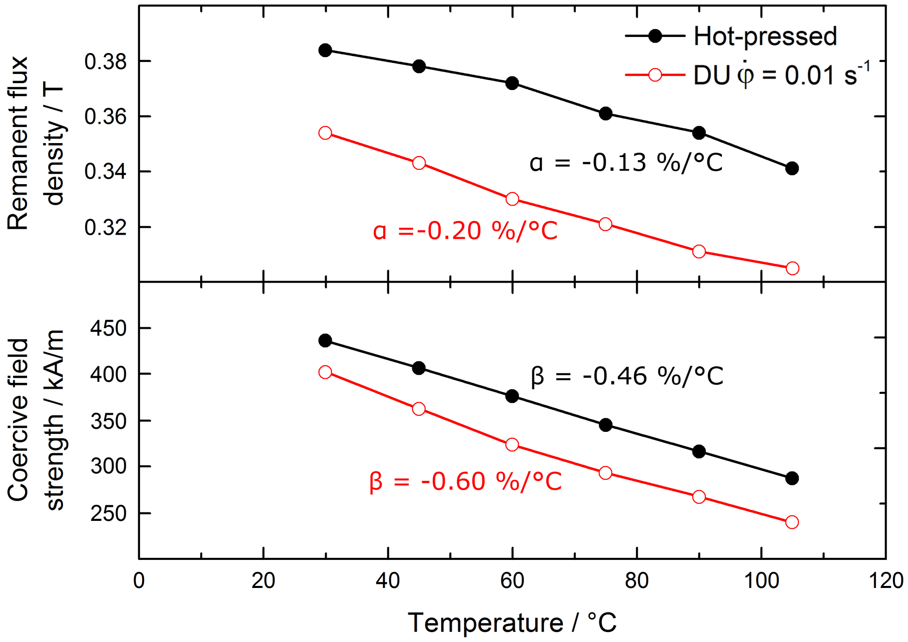

Figure 4.31: Consecutive measurements of the hot-pressed and die-upset ($\dot{\varphi} = 0.01\,\mathrm{s}^{-1}$) magnet for the determination of the temperature coefficients α and β. The temperature was equilibrated for up to 30 min before each measurement.

Magnetization mechanism

For a complete picture of the magnetic response of the bulk magnets, initial magnetization curves have been recorded and compared to respective measurements of the utilized ribbon material in the as-spun and annealed state. Due to nanocrystallinity and predominantly globular grains, fine particle processes (see Section 2.1.2) are assumed. The resulting measurements are presented in Figure 4.32. For the die-upset samples, the initial magnetization curves have been recorded parallel to the deformation direction. Essentially, the initial susceptibilities are throughout very similar.

The very early regime of reversible domain wall movements ends already below field strengths of 50 kA/m. This can be explained by the presence of very few domain walls in the nanocrystalline grains which are not considerably larger than the single domain particle size ($\geq$ 100 nm) approximated by Equation 2.5 with $K_1 = 4.3\,\mathrm{MJ/m^3}$ and $A = 50\,\mathrm{pJ/m}$ [92, 220]. At similar field strengths ($\approx$ 250 kA/m) the regime of irreversible domain wall movement is left and the increasing orientation of magnetic dipoles with the external field sets in. Limiting cases are the annealed ribbons, which are meant to be comparable with regard to the experienced heat treatment, and the slowly die-upset magnets.

At this point it should be noted that the exemplary fabrication of a hot-pressed magnet from understoichiometric, Ga-free $Ce_{0.5}Sm_{0.5}Fe_{10}Ti_1V_1$-melt-spun ribbons has also been successful without any procedural differences or optical peculiarities. However, no experiments regarding the die-upsetting were conducted. The magnetic characterization is given in Figure A.8 (see appendix). The reduced H_c of roughly 285 kA/m turns out as the main difference. This is presumed to be a result of the understoichiometric RE-content. XRD-patterns of the as-spun and annealed ribbon material, as well as the produced hot-pressed magnet, are essentially equal to

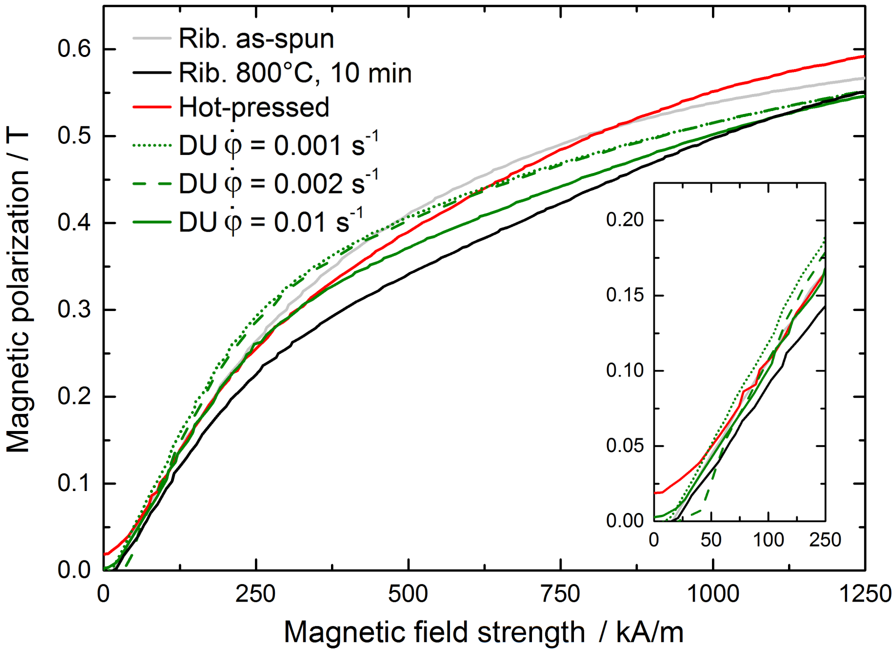

Figure 4.32: Initial magnetization curves of as-spun and annealed ribbon material (Ga-containing) as well as the hot-pressed and die-upset magnets produced from it. The inset shows a magnified section close to the origin.

those of the Ga-containing material. The microstructure differs only by the absence of RE_3Ga_1. Due to the fact that the RE-content of the Ga-containing material is not exceedingly overstoichiometric, the principal microstructure (see Figure 4.24, Figure 4.27 and Figure 4.28) does not reveal the role of a RE-surplus or further confirm the tendency of the associated bright phases to cover main phase interfaces as suggested from Figure 4.18.

Evaluation of texturability

Die-upsetting of hot-pressed $Ce_{0.5}Sm_{0.5}Fe_{10}Ti_1V_1$ precursors (Ga-containing) is not accompanied by the benefit of a raised J_r. This requests the detailed assessment of the material-specific properties which are typically presumed to be decisive to texturize Nd-Fe-B (see Section 2.1.1). The experimental results from above have shown that the grains of the 1:12-phase do not strictly grow isotropically. There is a tendency for an increased growth velocity parallel to the crystallographic c-axis which is inverse to the characteristics of the $Nd_2Fe_{14}B_1$-unit cell and furthermore disadvantageous regarding an alignment of the grains' magnetically easy axes. For the presented process parameters, the grains of the die-upset magnet remain, however, predominantly globular. This does not suggest a considerable shape anisotropy for the individual grains.

With the predicted decrease of saturation polarization from 1.5 T for $Sm_1Fe_{11}Ti_1$ to 1.2 T for $Sm_1Fe_{10}Ti_1V_1$ (1.9 T for Sm_1Fe_{12}), DFT-simulations reproduce the experimentally determined J_s-discrepancy between the V-free and -containing series while also approximating the value for $Sm_1Fe_{11}Ti_1$ at absolute zero quite well [148]. The reported finding of maximum Fe-moments on 8i-sites is also extractable. Figure A.1 shows the underlying unit cells (see appendix). The calculated elastic constants C_{11}, C_{22} and C_{33} are presented in Table 4.7 together with a comparison to calculations for Nd-Fe-B [221]. The broken symmetry of the unit cells (due to the presence of Ti and V) does necessarily cause different raw values for C_{11} (a-axis) and C_{22} (b-axis). These define upper and lower limits which are assumed to average for a real crystallite. Besides the mean values, the latter are also presented in the table.

Table 4.7: Selected elastic constants of the elasticity tensor for the calculated unit cells compared with reported data for Nd-Fe-B [221]. Values are partly averaged to account for the actual indistinguishability of C_{11} and C_{22}. The numbers in brackets indicate the raw values from the DFT-simulation.

Phase	C_{11} / GPa	C_{22} / GPa	C_{33} / GPa
Sm_1Fe_{12}	225	225	251
$Sm_1Fe_{11}Ti_1$	218 (227)	218 (210)	224
$Sm_1Fe_{10}Ti_1V_1$	237 (231)	237 (244)	258
$Nd_2Fe_{14}B_1$	234	234	228

For Sm_1Fe_{12}, the magnitude of C_{33} (c-axis) is elevated with respect to the corresponding elasticity constants for the a-axes (basal plane). In the same way, the averaged out-of-plane elasticities of $Sm_1Fe_{11}Ti_1$ and $Sm_1Fe_{10}Ti_1V_1$ exceed their in-plane analogs by up to 8 % which is especially pronounced for the V-containing phase. With this outcome from the simulations, the $Ce_{0.5}Sm_{0.5}Fe_{10}Ti_1V_1$-phase is concluded to behave qualitatively inverse to Nd-Fe-B.

A comparison of the present material with Nd-Fe-B in terms of an active solution precipitation mechanism, being typical for the latter, could not be made in this work. Even though it is verified that a liquid phase (RE_3Ga_1) is present in the material, possibly facilitating the die-upsetting, no RE-rich phase between the single 1:12-grains was definitely proven. This phase and the eventually associated solution precipitation mechanism, however, would only promote the material transport and not allow for the formation of a texture because the more important factors do not apply.

In principle, the presumably raised growth parallel to the c-axis would still permit an obtainable remanence enhancement as a result of a texture. The recently discussed anisotropy of the elastic constants constitutes a problem, though. Thus, the magnetically easy axes would orient radially in the plane of the flat cylinder (die-upset magnet) and reduce the occurrence of grains with easy axes parallel to the deformation direction. This would suggest a perceivable difference parallel and perpendicular to the deformation direction. At best, EBSD or TKD would reveal an increased density of red grains (c-axis parallel to the viewing direction) which are smaller on average. However, this is, in the scope of the present results (see Figure 4.28), not confirmed and does not seem to be the case. For a proof, statistically larger areas would need to be analyzed. Independent of any (presumably low) potential, the performed experiments fail to find any remanence enhancement. Therefore, no texture originates for reasonable process parameters.

4.2.5 Closing evaluation

The substitution of Fe for V in $RE_1Fe_{11}Ti_1$ raises especially the significance of Ce-containing representatives. These usually exhibit low coercive field strengths. For all Ce/Sm ratios, the replacement of high-moment Fe causes a similar reduction of the saturation polarization by 0.25 T to approximately 0.9 T. Curie temperatures remain unchanged and increase for both series linearly with the Sm-content. Achievable coercivities for V-containing, nanocrystalline samples are considerably high for $x \geq 0.5$. The presence of V is found to speed up the crystallization, while the respective phase tolerates larger particle sizes.

Since it is possible to achieve promising coercivities for a relatively high Ce-content, $Ce_{0.5}Sm_{0.5}Fe_{10}Ti_1V_1$ turns out as major trade-off material. For comparability with the established manufacturing process of nanocrystalline bulk magnets based on the $Nd_2Fe_{14}B_1$-phase, a corresponding, Ga-containing ribbon material has been hot-pressed. The sudden proximity of the resultant properties to expectable values shows the transferability of the examined properties to a demonstrator magnet. Die-upsetting, however, fails to induce a texture and further raise the remanent polarization as well as the maximum energy product. This is attributed to the fact that decisive factors, for the processing of Nd-Fe-B, have shown to be not fulfilled.

4.3 Kerr microscopy

4.3.1 Qualitative Kerr microscopy

For the closely investigated Th_1Mn_{12}-type phases of the present work, Kerr microscopy has been performed in order to track changes of the domain patterns that come along with varied compositions. In this context it has been noticed that the focal plane, in which Kerr-images are clearly displayed, differs from the one where surface features, like pores or tiny cracks, are usually observed as a sharp image. To record the individual pictures from the following compilations, several arc-melted samples have been freshly prepared and not sputter-coated. The aim was to properly display the patterns of closure domains which indicate that the easy magnetization axes point out of plane.

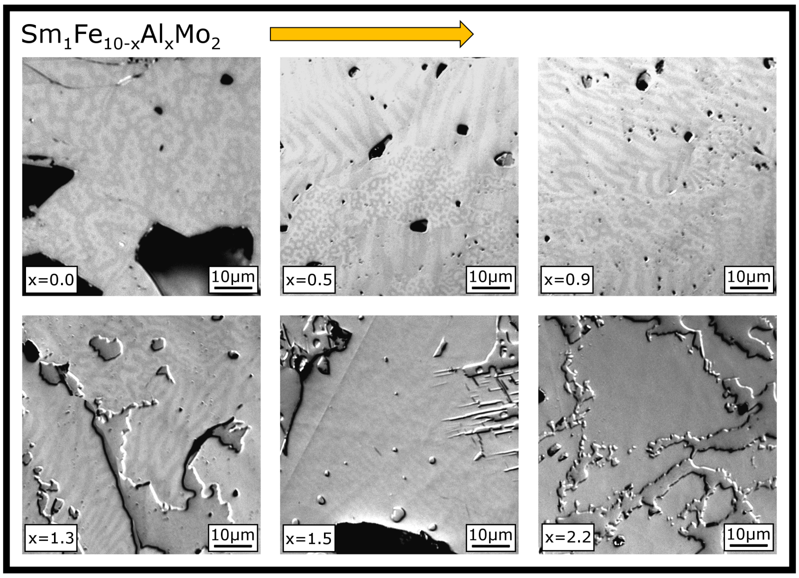

Figure 4.33: Domain patterns of $Sm_1Fe_{10-x}Al_xMo_2$-samples with different Al-content. For better visibility, contrast and brightness are (consistently) adjusted.

The samples presented in Figure 4.33 contain mostly the $Sm_1Fe_{10-x}Al_xMo_2$-phase. Eventual secondary phases do not exhibit domain structures that may lead to confusion with the hard-magnetic phase. Kerr-patterns of the latter show a decreasing contrast with increasing Al-content. For x=1.5 domains can hardly be identified. With even higher Al-contents the phase does no longer show a perceivable contrast which matches the drop of T_C below RT (see Figure 4.5).

From the polarized light images of $Ce_{1-x}Sm_xFe_{11}Ti_1$- and $Ce_{1-x}Sm_xFe_{10}Ti_1V_1$, presented in Figure 4.34, it is possible to determine the influence of successively altered RE-ratios on the domain pattern. This influence can furthermore be compared to the presence and absence of V. For both series, the contrast of the domain patterns becomes less intense as the Ce-content is raised. In addition, the features of the patterns become clearly smaller. These observations even tend to hold true for different phases like $RE_2Fe_{14}B_1$ as well as the Co-based RE_1Co_5 (see Figure A.9 in the appendix).

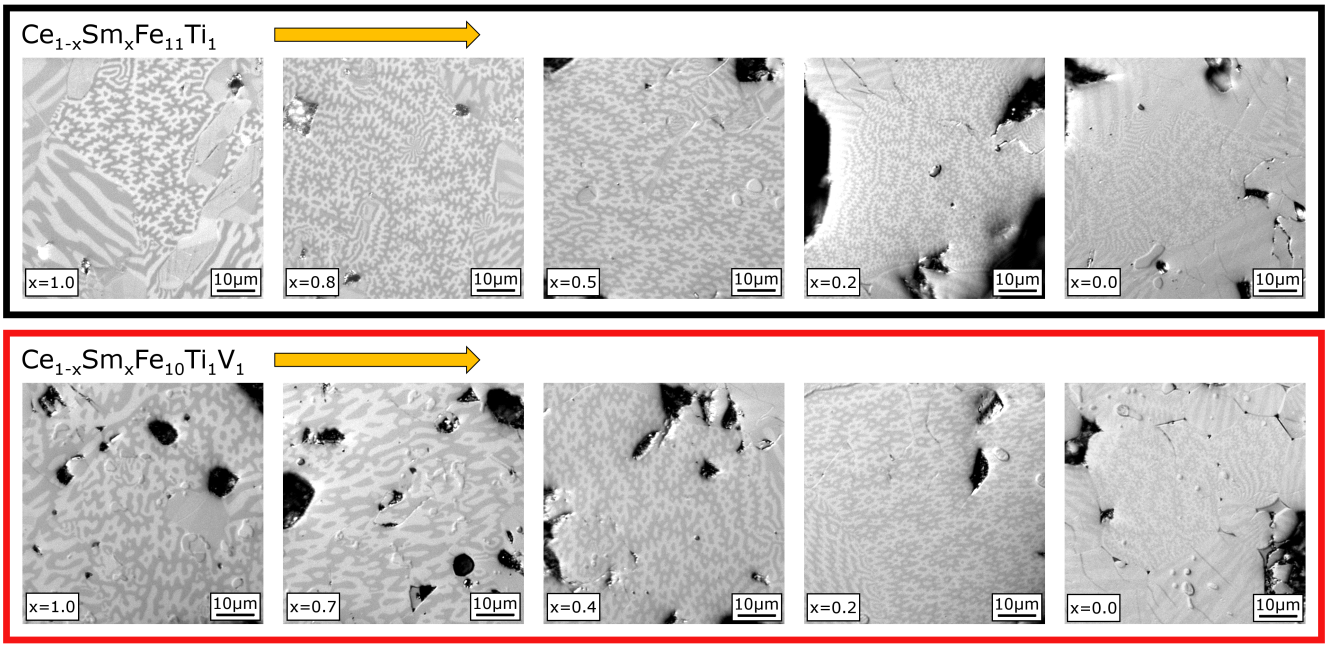

Figure 4.34: Domain patterns of $Ce_{1-x}Sm_xFe_{11}Ti_1$- and $Ce_{1-x}Sm_xFe_{10}Ti_1V_1$-samples with different RE-ratio. For better visibility, contrast and brightness are (consistently) adjusted.

A qualitative effect of V, however, cannot be derived that simple, which is why a corresponding evaluation is addressed in the quantitative part of the analysis.

4.3.2 Quantitative Kerr microscopy

Prior investigations of samples from the material system Ce-Sm-Fe-Ti-V have demonstrably shown that the respective J_S within a specific series (V-free or -containing) are very similar. However, the Kerr-contrasts decrease incrementally with increasing Ce-content. Therefore, the corresponding domain contrasts are assessed quantitatively. Values in the plot of contrast over J_S have been statistically determined as described in the experimental section (see Section 3.2).

Essentially, the individual phases in Figure 4.35 define two parallel stripes which are separated by the discussed J_S-difference of roughly 0.25 T, depending on the presence of V (V collectively reduces J_S). Starting from the consideration of a single series, it can be noticed that the scattering of individual domain contrasts is quite large. The analysis confirms the qualitative dependency on the present RE-ratio, though. Estimating the saturation polarization for one of the five compositions (within a series) based on its domain contrast, would offer eligible values that can vary by almost 0.1 T. Within that range the remaining J_S are not even consecutively dependent on the RE-ratio. In addition, the contrasts of the V-free and -containing series cover the same range. The apparent sensitivity of Kerr microscopy, yielding a dependency from RE-content, is therefore not capable to resolve differences between $RE_1Fe_{11}Ti_1$ and $RE_1Fe_{10}Ti_1V_1$. Contrast determinations would therefore not necessarily make differences between phases that distinguish by 0.3 T in terms of J_S. Uncertainties of this magnitude have enormous consequences on $(BH)_{max,theo}$ and therefore on the relevance for practical applications.

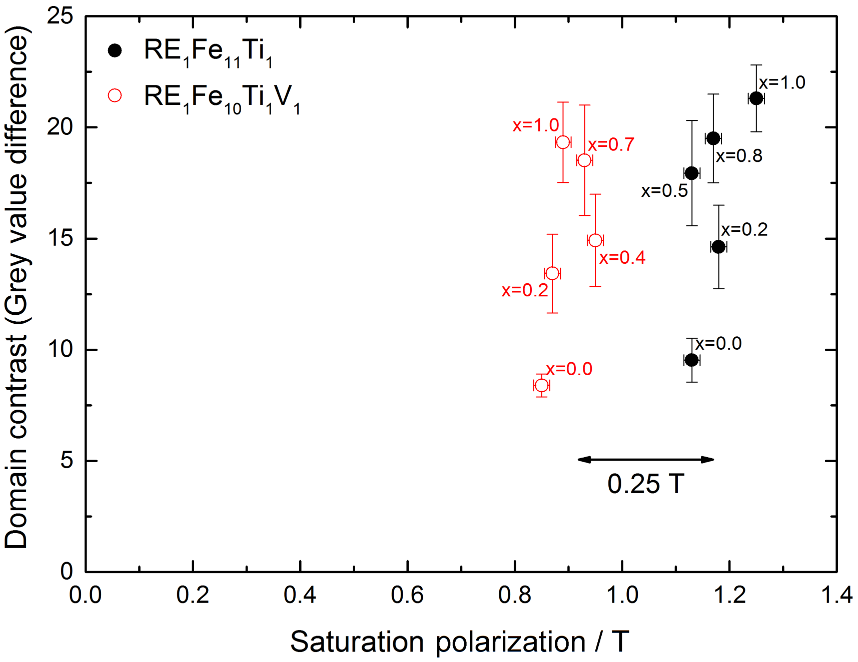

Figure 4.35: Observed domain contrasts for the $\mathrm{Ce_{1-x}Sm_xFe_{11}Ti_1}$- and $\mathrm{Ce_{1-x}Sm_xFe_{10}Ti_1V_1}$-phase series over their measured saturation polarizations.

In order to complete the observations, a comprehensive analysis of further domain contrasts is added. In this context, prominent ferromagnetic phases with mostly well-documented J_S have been specially produced and evaluated. This shall answer the question whether it is possible to determine intrinsic magnetic properties from close investigations of domain features. The inclusion of Fe- as well as Co-based phases is supposed to sum up the study and show if tendencies for very different material classes can be observed. The domain patterns of the different phases are very diverse, have different appearances and are especially pronounced for the representatives with considerable saturation polarization (see Figure A.9 in the appendix). Figure 4.36 presents the domain contrasts of most observed phases over their individual saturation polarizations. Many phases are positioned based on their specified literature values for J_S [10, 13, 131, 137, 222–224]. For phases whose J_S have been measured in this work, the respective values are comprised within the uncertainty bars. The exact location of the phases in the plot is blurred by the scattering of literature values and also the variance of the determined contrast.

For the separate consideration of the Mo-stabilized 1:12-phase in a plot like Figure 4.35, it would be desirable to have the corresponding magnetic measurements for a larger set of samples, being variant in terms of the Al-content. In addition to the previous, qualitative statements from the considerations of Figure 4.33, the $\mathrm{Sm_1Fe_{10-x}Al_xMo_2}$-phases with x=0.0 and x=0.8 are anyway included in the following discussions. For these compositions, saturation polarizations have been measured (see Figure 4.4) and evaluable domain patterns exist. However, their determined contrasts do not differ significantly as the Al-content is accordingly increased. Even though the decrease of J_S by 0.14 T correlates with a slightly lowered contrast, it is especially striking that a significant J_S can still be measured for $x \geq 2.0$. For that Al-content, the phase shows practically no more contrast (see Figure 4.4).

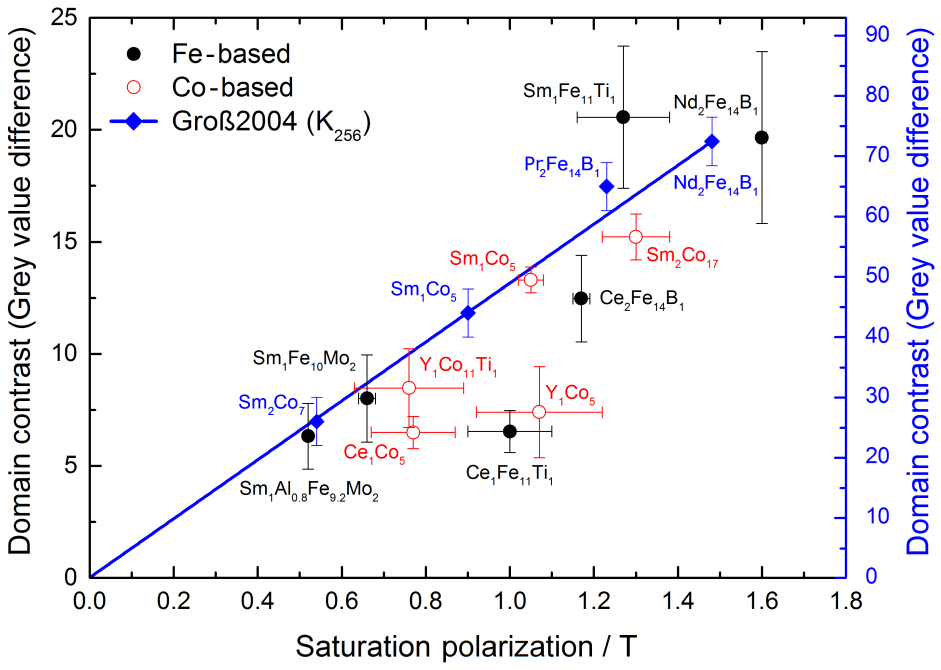

Figure 4.36: Observed domain contrast of most investigated phases over their individual saturation polarizations measured in this work or taken from literature [10, 13, 131, 137, 222–224]. Results from the motivating literature report are also shown together with the claimed calibration from fitting [40].

Figure 4.36 jointly illustrates the determined domain contrasts of the samples from this work over their respective saturation polarizations. For comparison, the results of the motivating literature report are given on a second contrast axis. It is cropped and scaled based on $Nd_2Fe_{14}B_1$ since associated absolute values are higher [40].

With J_S-values ranging roughly from 0.5 T to 1.6 T, the exhibited average contrasts of Fe- and Co-rich phases from this work reproduce, in a first approximation, the postulated dependency. There are especially differences between materials with very high and very low J_S. Nevertheless, the statistically quantified domain contrasts (according to Figure 3.4) scatter strongly as already discussed before. Any linear extrapolation of the data should comprise the origin to represent a physically meaningful dependence of contrast on J_S. Thus, phases with vanishing contrast finally yield zero J_S. Accounting for the location of most of the individual data points (this work), such a line would be too broad. The good approximation of the reproduced literature data by a linear fit is due to the very limited number of analyzed phases. Furthermore, these have extremely different J_S and are exceptional representatives among the ferromagnetic materials.

Relative positions (compared to the $Nd_2Fe_{14}B_1$-reference) of phases occurring in both assessments are similar. This can be explained by the observation that differences of averaged contrasts remain more or less similar even when microscope adjustments are slightly changed. Determined absolute contrasts, however, can be very different and are not necessarily reproducible.

It holds true that especially phases with $J_S \leq 1.2$ T yield very similar contrasts even though absolute saturation polarizations are very different. This has also been discussed for the $RE_1Fe_{10}Ti_1V_1$-series before, which has not been part of the batch analysis on which Figure 4.36 is based, though. Furthermore, uncertainties from contrast investigations for any phases with

moderate or low J_s are too large for differentiations. A good resolution for phases in this area would be key prerequisite to reliably replace extensive measurements for new phases, as these presumably fall into this area.
In its entirety, the merged data of the produced samples does therefore not provide a suitable set from which predictions regarding absolute saturation polarizations are possible based on simple contrast evaluations. The comparison of Fe- and Co-rich phases does not give rise for differentiations and previous argumentations are the same independent of their joint or separate treatment. This is in contradiction to literature reports [37, 38].

The quantification of K_1 by magnetic measurements is especially challenging, which is why the replacement of such experiments by an evaluation of domain patterns is favorable. However, the insertion of averaged domain widths in an explicit version of Equation 2.11 requires that J_s has been determined reliably beforehand. Provided that the corresponding values are well-established, the widths of stripe domains have been assessed exemplarily for several Fe- and Co-based phases. Compared to closure domains, stripe domains allow, in general, more accurate determinations and yield absolute values which are larger. Nevertheless, the phases exhibit also very similar average widths of 2 μm to 5 μm which have standard deviations of up to 25 %. The only exception is Sm_1Co_5 with significantly larger domain widths that scatter in a similar manner, though. The possibility to assign pure stripe character to a domain is questionable.

The fact that J_s is supposed to originate likewise from a previous evaluation of Kerr-patterns (contrast), precludes the further usage of Equation 2.11. The discussed uncertainties regarding the determination of saturation polarization would enter with exponent 4 so that a final value of K_1 builds significantly on the quality of J_s. Thus, the consideration of averaged domain widths does not lead to reasonable estimations. There is no relation giving rise to a plot of domain width over K_1.

4.3.3 Closing evaluation

Contrary to the initial motivation, multiple analyses could show that the quantification of intrinsic magnetic properties via Kerr microscopy is not suitable. This simplified measuring technique is mostly thought to be applied to phases with moderate saturation polarizations. For those, the typically observed uncertainties are especially restricting. A subsequent calculation, including the derived saturation polarizations and measured domain widths, for the determination of the anisotropy constant is not promising.

In this work, the approach to estimate intrinsic magnetic properties from domain patterns followed essentially the principles of the basic literature reports [37–40]. Differences leading to contrary results are important and shall therefore be summarized.
Special focus was set on the domain contrasts (regarding J_s). In this regard, it turns out that the (desired) calibration line can be established differently depending on the tested samples. In the referred publications these are predominantly exceptional representatives (RE_1Co_5 and $RE_2Fe_{14}B_1$) with properties that are likely to excel those realistically expected for new phases. Even for these exceptional representatives, the indicated uncertainties are notable and

J_s-scatterings are not sufficiently considered. Where a Th_1Mn_{12}-phase ($Ce_1Fe_{11-x}Co_xTi_1$) is treated, there are no details regarding the utilized calibration and uncertainties. Based on the reported data, it seems not justified to treat Fe and Co separately. Moreover, new Fe-based phases often involve Co-substitutions.
The present domain width analysis (regarding K_1) by hand cannot be compared to the automatic processing in the mentioned literature reports. These present several models for the translation of measured domain widths via domain wall energies into anisotropy constants, necessarily assuming an exchange constant. The estimation of the anisotropy constant K_1 has only be comprehensibly tested for a well-known phase which is $Nd_2Fe_{14}B_1$.

Besides the local polarization, the individual chemistry of a phase is identified as crucial parameter for the observable domain contrast. There is, however, a tendency towards high-contrast patterns for phases with high saturation polarizations. Additionally, relative positions of phases, in a plot of domain contrast over saturation polarizations, are well reproducible. Consequently, polarized light microscopy remains justified as a qualitative tool - not least because it proves uniaxial anisotropy.

5 Conclusions and Outlook

Analyzed ferromagnetic phases (including material systems)

Motivated by the search for new permanent magnet materials, the impact of compositional changes has been extensively studied for different ferromagnetic Th_1Mn_{12}-type phases. Since the main characteristics of their ternary prototype phases are sufficiently well-known, the main focus was set on further developments by the targeted addition of dopant elements. Concrete evaluations of $Sm_1Fe_{10-x}Al_xMo_2$ and $Ce_{1-x}Sm_xFe_{11}Ti_1$ (& V-containing representative) regarding in- and extrinsic magnetic properties as well as solubility ranges and equilibrium phases could be made.

For different sample compositions, $Sm_1Fe_{10-x}Al_xMo_2$ has been found in equilibrium with α-Fe(Mo, Al), $(Fe, Al)_7(Mo, Al)_6$, $Sm_1(Fe, Al)_2$ and the 2:17-phase. Accompanied by a continuous increase of lattice constants, up to 50 at.% of the Fe in $Sm_1Fe_{10}Mo_2$ can be substituted by Al. Higher Al-contents lead to the preferred formation of a Mo-lean phase. The dopant element occupies crystallographic 8i- and 8j-sites in a ratio of 1:2. The successive increase of Al-content is accompanied by a decrease in high-field polarization from an initial value of 0.66 T. In a first approximation, this magnitude can be attributed to the fact that four Mo-atoms (per unit cell) are required for the stabilization of the phase. The maximum Curie temperature can be quantified to about 130 °C and is reached for 3.8 at.% Al (x=0.5). Coercive field strengths of intensively milled and annealed powders decrease for the analyzed stoichiometries from 153 kA/m, for the prototype phase, to values below 35 kA/m for x=2.0. For substantial Al-contents, recrystallization is found to occur much slower.

The $Ce_{1-x}Sm_xFe_{11}Ti_1$-phase has been analyzed especially with a focus on the influence of V-doping. For the considered temperature of 1000 °C, the existence range comprises stoichiometries between the well-reported $RE_1Fe_{10}V_2$ (RE=Ce) and $RE_1Fe_{11}Ti_1$. The opposed stoichiometries, $RE_1Fe_{10}Ti_2$ and $RE_1Fe_{11}V_1$, are avoided. Prominent neighboring phases are α-Fe(Ti, V), RE_1Fe_2, Fe_2Ti_1(V) and the 2:17-phase. Measurements on V-free single phase samples yield a high-field polarization of approximately 1.2 T which decreases by about 0.25 T when V is present. The simultaneous refinement of X-ray- and neutron diffraction patterns finds that Ti and V prefer 8i-sites, where the replacement of high-moment Fe causes the observed reduction in saturation polarization. The lattice constants increase with the Sm-content, whereas the V-substitution reduces **a** and **c** for the whole range of RE-ratios. Curie temperature increases likewise as the phase gets richer in Sm. Maximum values of roughly 300 °C have been obtained independent of the presence of V, while the coercivity of intensively milled and annealed powders benefits significantly from the latter element. This is reproduced for nanocrystalline, melt-spun material. The observed effect has been found to be extrinsic and more pronounced for Sm-rich phases than for Ce-rich representatives. Further, the crystallization speed is promoted by the presence of V. The considerable reduction of the maximum coercivities close to x=0.5 cannot be correlated with the linear trend of the respective anisotropy fields, which are furthermore independent of the presence of V. The actual RE-contents of the nanocrystalline powders play a significant role regarding their possible coercive field strengths. Minimum RE-contents are associated with the equilibrium phase compositions whereas surpluses do not allow for further enhancements. The promising magnetic properties of the nanocrystalline material

(≥600 kA/m for a material with Ce/Sm = 1:1) could successfully be transferred to the bulk state via hot-pressing of $Ce_{0.5}Sm_{0.5}Fe_{10}Ti_1V_1$(Ga)-melt-spun ribbons. The maximum energy product of the final magnet is 25 kJ/m^3. Due to its isotropic nature, this amounts to more than 55 % of the expectable value. Microstructural analysis finds RE_3Ga_1 (liquid during processing) and RE_1Fe_2 on ribbon boundaries. The main volume is composed of the main phase with Fe_2Ti_1(V) (variant in composition) as finely distributed secondary phase, which is depleted close to the ribbon boundaries. Magnetic measurements and structural investigations indicate that a subsequent die-upsetting step with different deformation rates could not succeed in inducing a texture and increasing remanence. Qualitative density functional theory-simulations suppose averaged out-of-plane elasticities for the V-free and -containing unit cells (Sm-based) which exceed the associated in-plane values by 8 %. Together with the experimentally observed tendency of accelerated out-of-plane growth, two decisive factors are inverse to the system Nd-Fe-B.

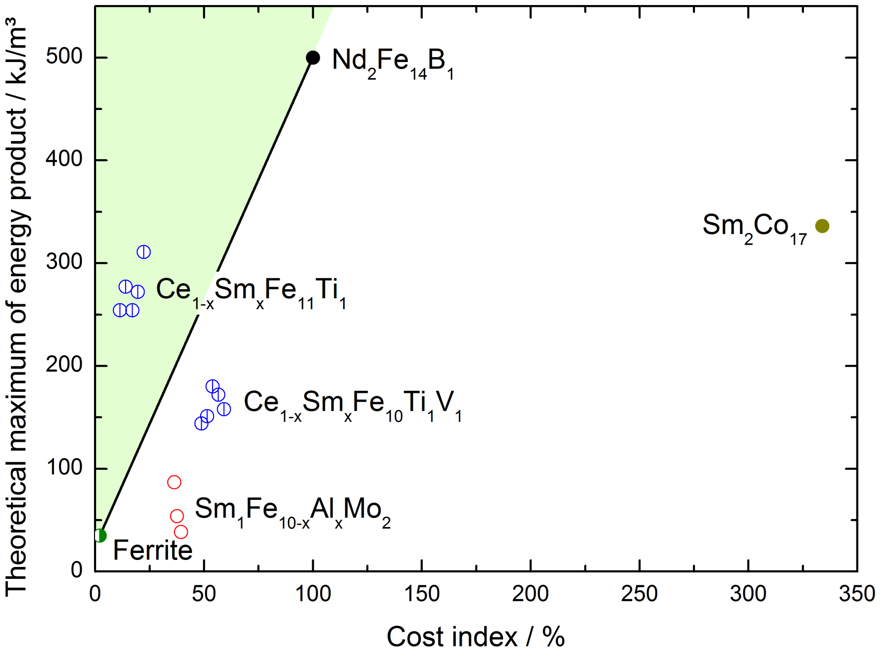

Figure 5.1: Potential of the analyzed Th_1Mn_{12}-phases based on their individual $(BH)_{max,theo}$ and cost indices regarding only material prices. $Nd_2Fe_{14}B_1$ is taken as a reference and the resulting target area is highlighted (green). All prices are taken from the web presences of London Metal Exchange and Metal Pages on 06.03.2018. Despite pure metals for the remaining elements, the following products have been considered for B, Ti and V: Fe-B (18 wt.% B), Fe-Ti (70 wt.% Ti), Fe-V (78 wt.% V). Ferrite prices have been globally assumed as 2 €/kg.

Primarily, the phases have been analyzed regarding the requirements for an intermediate material between ferrites and sophisticated Nd-Fe-B-magnets. To rate their suitability from this point of view, pricing needs to be additionally addressed. For a first reflection, Figure 5.1 depicts the individual, theoretical energy products over the pure material prices, neglecting manufacturing costs. Prices are characteristic for the time that the present work has been completed. The $Nd_2Fe_{14}B_1$-phase has been taken as a reference on the abscissa and set to 100 %. For meaningful argumentations, the coercive field strength also needs to be taken into account. If it is much greater compared to ferrites, Figure 5.1 matters directly and the material should be well within the target area because its adaptation for existing applications will likely involve further modifications. For example, a permanent magnet synchronous machine (with given power) will increase in size if the remanent polarization decreases. The costs, associated with additional Cu-windings and a larger housing, need to be compensated. However, if the coercivity roughly coincides with ferrites, costs should also do so while the saturation polarization will be decisive. In this case, RE-based phases cannot be competitive, though.

The plot shows that only the V-free $Ce_{1-x}Sm_xFe_{11}Ti_1$-phases are able to enter the target area (green). However, especially the coercivities of Ce-rich representatives are low compared with the associated V-containing series. Despite an explicitly favorable position in the diagram, this fact will cause actual energy products to be very low, thus reducing the level of interest. Furthermore, the too weak resistance against demagnetizing fields generally excludes the use of a material in applications where Nd-Fe-B or ferrites are employed. The $Ce_{1-x}Sm_xFe_{10}Ti_1V_1$-phases suffer from a decrease of the saturation polarization which comes along with the demand for V. A Ga-content of 0.5 at.%, which was used for the bulk magnets, further raises the corresponding cost indices by 3 %. Nevertheless, $Ce_{0.5}Sm_{0.5}Fe_{10}Ti_1V_1$ potentially approaches the indicated position close to the target area if texturing would be possible. Falling V-prices (quadrupled since 2017) might even compensate parts of the costs which come along with the complex manufacturing. Coercivities of about 425 kA/m are reasonable, even if tendencies towards 1000 kA/m are more favorable. With its Curie temperature, the 1:12-phase-based bulk material is suitable for applications at RT, just as prototype Nd-Fe-B-magnets. At elevated temperatures, however, the higher Curie temperature of Nd-Fe-B is determinant since the temperature coefficients (remanence and coercivity) are similar for both materials. Therefore, the $Ce_{0.5}Sm_{0.5}Fe_{10}Ti_1V_1$-phase may also be considered for bonded magnets.

The significance of Al-containing $Sm_1Fe_{10}Mo_2$-derivates for future applications is strongly reduced by the fact that respective saturation polarizations, and consequently also their energy products, are throughout quite low. Despite cost indices which fail to enter the target area, associated Curie temperatures and coercive field strengths (approximately comparable to ferrites) are too low. Furthermore, the manufacturability by established means is not given for these phases because the set of observed neighboring phases lacks a potential candidate being liquid at usual process temperatures. Thus, $Sm_1Fe_{10-x}Al_xMo_2$ falls short in terms of a replacement candidate for established hard-magnetic materials. With properties close to those of commercial ferrites, the need for Sm and Mo further reduces prospects.

Despite the achieved progress, some causal relationships remain to be elucidated in order to make future research more effective. For the system Sm-Fe-Mo-Al, this means the clarification of the increasing Curie temperature at low Al-content and the understanding of how this additional element affects the anisotropy field strength and coercivity.

In case of the more promising system Ce-Sm-Fe-Ti-V(Ga), the analysis has already gone quite far. The replacement of scarce or otherwise problematic RE (Sm) by those being less critical (Ce), has shown to be possible. Associated negative effects, however, need to be faced accordingly. Substitutions in well-known, easily forming phases are promising, even though interactions or influences like the one of V in $Ce_{1-x}Sm_xFe_{10}Ti_1V_1$ may be unpredictable. Further attention should be set on the bulk magnet production where more parameters are to be tested and especially variations of the die-upsetting step considered. In order to make use of the grains' preferential growth parallel to the c-axis, texturing needs to be enabled. Possibly, RE-surpluses

or even the transfer to a poly-element system need to be assessed. At the same time, reasonable limits of the tested parameters need to be preserved.
In addition, the extrinsic influence of V should be investigated in more detail. For this, detailed microstructural investigations, preferably including transmission electron microscopy at grain boundaries, are recommended. An optimization of the composition of the melt-spun ribbons might increasingly suppress the formation of Fe_2Ti_1(V) and increase the percentage of the 1:12-phase. Another interesting approach might be to consider $Ce_{0.5}Sm_{0.5}Fe_{11}Ti_{0.5}V_{0.5}$ and its associated series. This promises a potential increase of the saturation polarization and the energy product. Finally, it would be interesting to produce single crystals in order to consolidate the intrinsic magnetic properties and also the elastic constants.

Kerr microscopy

Based on the results, Kerr microscopy can be rated as a rapid evaluation method for the potential of new magnet materials. It turns out that quantitative estimations of intrinsic magnetic properties cannot be reliably derived by the analysis of domain patterns. For the presented procedure (and specified equipment), the method fails because determinable contrasts of phases with moderate saturation polarization are very similar. Especially critical are the uncertainties which arise for statistically relevant analyses. Starting point for the determination of the respective saturation polarization of an unknown phase is its relative domain contrast among multiple confirmed data points (of phases with well-known properties). For that purpose these data points need to be extrapolated through the origin. The width of such a fit precludes, however, to resolve differences below 0.3 T among different phases. That would definitely be required for significant quantifications. Furthermore, it is striking that the chemistry of phases with similar saturation polarizations contributes to the observable domain contrast. Therefore, it is doubtable whether Equation 2.10 actually allows to conclude the proportionality between domain contrast and saturation polarization. It cannot be guaranteed for sure that only the polar Kerr effect contributes to the observable contrast. Moreover, it is unclear how the direct dependence of the rotation of the polarization plane on the sample magnetization is changed by the analyzer or the interpretation by the camera (brightness and contrast). Even after equal preparation steps, the samples can have different surface qualities and stress states. These have shown to influence the Kerr-pattern but are not closer unraveled in this work [225, 226].

Even though Kerr microscopy does not replace conventional magnetic measurements, it remains an interesting method to identify phases with good prospects. The domain patterns, observed with polarized light, allow to qualitatively classify the anisotropy of a material with regard to uniaxiality. The method permits to quickly detect the presence of substantial polarization. Therefore, it is still suggested to include the assessed technique for the search of new permanent-magnetic phases. It is particularly useful for the fast screening of multiple samples.

For further statements on the Kerr method, it is worth to reconsider domain patterns in terms of all influencing factors. The respective contributions of the latter should be assessed with more advanced methods including special light sources (e.g. laser) for even better defined conditions and geometries. Impacts of the state and constitution of the sample have to be clarified to the highest extent in order to work out recommendations regarding the method's application.

Recommended procedure for the assessment of new phases

Especially the production of single phase samples (determination of intrinsic properties) and the realization of a demonstrator magnet have revealed peculiar challenges. When searching for an extension to the existing permanent-magnetic materials, it is important to proceed in the right direction and not to lose sight of the effort. In principle, the determination of intrinsic magnetic properties tends to be less extensive. However, extrinsic properties may be complex to elucidate and the fabrication of a demonstrator series (or an exemplary industrialization) typically requires a high invest.
Ab-initio approaches need a sufficient description of fundamental quantities that are difficult to access. Though increasingly used, the information content of simulations or their validity regarding real applications (temperature) remains questionable. Thus, even after extensive calculations questions may remain unanswered. Consequently, the extensive experimental route is only partially replaceable. From an application point of view, certain measures can be deduced in order to support the search for new candidates or to evaluate presented ones. Depending on priorities and available resources, the consecutive steps of Figure 5.2 are recommended.

First of all, step A recommends to theoretically deal with the phase of interest. It is advisable to search for analogies to known systems and, if necessary, to evaluate the criticality, availability and workability of the involved elements, taking into account the proposed composition. The systematic arrangement of the elements in the periodic table is a suitable basis for the rapid assessment for possible alternatives. It is helpful to consult experts regarding the classification of the constituents' individual properties (hardness, sensitivity to oxidation, vapor pressure) and their natural occurrence (usage of Fe-V instead of purified V). Thus, basic theories can be evaluated in terms of consistency and consequences (e.g. the impact of Fe-replacements on the saturation polarization and the energy product). However, the actual saturation polarization is not only determined by the number of non-Fe-atoms in the unit cell. This can be learned from the comparison of the corresponding values for $Sm_1Fe_{10}Mo_2$ and $Sm_1Fe_{10}Ti_1V_1$.

If first results regarding the magnetism of the phase are available, then it can directly be moved on to step C. If not, step B recommends contrast determinations using polarized light microscopy. Despite the final rating of this approach in the present work, this can be profitable because particularly good contrasts and proper patterns generally indicate a high potential of the phase. Manufacturability is indirectly assessed as well. If, for example, no annealing is required to form the phase, or if large amounts are easily achieved for suitable compositions (self assembly), this is indicative for a high stability.

Step C proposes a measurement of the Curie temperature. Regarding applications where the generation of heat cannot be excluded (motors), this quantity will definitely be decisive. Even on non-single phase samples it can be quickly determined with relatively simple means.

The exclusive presence of the main phase is required to quantify the saturation polarization. The determination of the latter quantity is suggested as step D since it allows to calculate the theoretical energy product for further considerations. In fact, it is unlikely to actually reach this value because it takes years to approach even a high percentage of it.

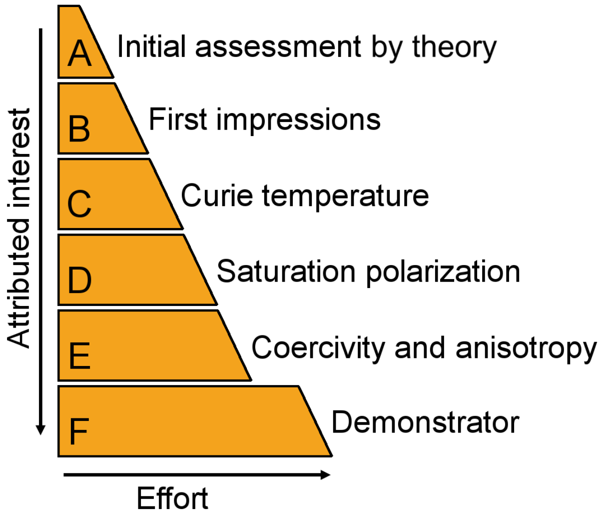

Figure 5.2: Recommended steps for a procedure to further develop and assess new phases to be used as permanent magnets.

Step E aims at the anisotropy field strength, which is most difficult to determine among the intrinsic properties and allows only limited statements regarding actual applications. Ideally the measurement of the anisotropy field strength (and saturation magnetization) requires a single crystal. Good processability is required to achieve a smart microstructure and to make use of the present anisotropy. Possibly, many further thoughts are necessary (e.g. use of secondary phase). Therefore, it makes sense to rather measure coercivities which can be realized in actual samples. This opens a large field because the estimation of maximum coercivities via intensive milling or melt-spinning (with subsequent annealings) is in fact suitable, but also very time-consuming. Few attempts with reasonable annealing conditions (900 °C) can still be advisable. Should considerable values (e.g. ≥300 kA/m) be reached without optimizations, further effort can be worthwhile. In general, it is also suggested to consider the temperature dependence of decisive quantities. Concerning the coercive field strengths, this can be done by determining the respective coefficient.

If interest in the phase persists, step F intends to manufacture a demonstrator as soon as possible when a complete picture of the potential and the inherent characteristics of the phase are available. More features and difficulties (also regarding processing, densification and texturing) might show up then. However, it will also be possible to judge the prospect of the project with reasonable effort and tell whether simple and established means can lead to the desired result. Due to the well-known lack of direct transferability, painstakingly determined intrinsic values remain numbers with limited significance. Of central interest for a targeted industrialization are the extrinsic characteristics that can demonstrably be achieved in real applications. This emphasizes why the maximum energy product and the shape of demagnetization curves have become key indicators.

References

[1] S. Sugimoto. Current status and recent topics of rare-earth permanent magnets. *Journal of Physics D: Applied Physics*, 44(6):064001, 2011.

[2] O. Gutfleisch, M. A. Willard, E. Brück, C. H. Chen, S. G. Sankar, and J. P. Liu. Magnetic materials and devices for the 21st century: Stronger, lighter, and more energy efficient. *Advanced materials*, 23(7):821–842, 2011.

[3] S. Hirosawa. Development of industrial nanocomposite permanent magnets: A review. *Transactions of the Magnetics Society of Japan*, 4:101–112, 2004.

[4] J. M. D. Coey. Hard Magnetic Materials: A Perspective. *IEEE Transactions on Magnetics*, 47(12):4671–4681, 2011.

[5] L. Chang, T. R. Eastham, and G. E. Dawson. In-situ magnetization of NdFeB magnets for permanent magnet machines. *IEEE Transactions on Magnetics*, 27(5):4355–4359, 1991.

[6] R. Krishnan. *Permanent Magnet Synchronous and Brushless DC Motor Drives*. CRC press, 2009.

[7] L. Zhong, M. F. Rahman, W. Y. Hu, and K. W. Lim. Analysis of direct torque control in permanent magnet synchronous motor drives. *IEEE Transactions on Power Electronics*, 12(3):528–536, 1997.

[8] R. Fischer and H. Kronmüller. The role of grain boundaries in nanoscaled high-performance permanent magnets. *Journal of Magnetism and Magnetic Materials*, 184(2):166–172, 1998.

[9] K. Hono and H. Sepehri-Amin. Strategy for high-coercivity Nd-Fe-B magnets. *Scripta Materialia*, 67(6):530–535, 2012.

[10] J. F. Herbst. $R_2Fe_{14}B$ materials: Intrinsic properties and technological aspects. *Reviews of Modern Physics*, 63(4):819–898, 1991.

[11] R. Skomski and D. J. Sellmyer. Anisotropy of rare-earth magnets. *Journal of Rare Earths*, 27(4):675–679, 2009.

[12] K. T. Park. Effect of metal-coating and consecutive heat treatment on coercivity of thin Nd – Fe – B sintered magnets. In *Proceedings of the 16th International Workshop on Rare Earth Magnets and Their Applications*, 2000.

[13] J. M. D. Coey. Permanent magnets: Plugging the gap. *Scripta Materialia*, 67(6):524–529, 2012.

[14] M. Sagawa, S. Fujimura, N. Togawa, H. Yamamoto, and Y. Matsuura. New material for permanent magnets on a base of Nd and Fe. *Journal of Applied Physics*, 55(6):2083–2087, 1984.

[15] G. C. Hadjipanayis, R. C. Hazelton, and K. R. Lawless. New iron-rare-earth based permanent magnet materials. *Applied Physics Letters*, 43(8):797–799, 1983.

[16] H. Kronmüller, R. Fischer, M. Seeger, and A. Zern. Micromagnetism and microstructure of hard magnetic materials. *Journal of Physics D: Applied Physics*, 29(9):2274–2283, 1996.

[17] Y. Wang, G. C. Hadjipanayis, A. Kim, N. C. Liu, and D. J. Sellmyer. Magnetic and structural studies in Sm-Fe-Ti magnets. *Journal of Applied Physics*, 67(9):4954–4956, 1990.

[18] W. Tang, Y. Zhang, D. Goll, G. C. Hadjipanayis, and H. Kronmüller. New $\mathrm{Sm(Co, Fe, Cu, Zr)_z}$ magnets with better temperature stability. *Journal of Magnetism and Magnetic Materials*, 226–230(0):1365–1366, 2001.

[19] C. B. Cizmas, C. Djega-Mariadassou, and L. Bessais. Influence of Si substitution on the structure and magnetic properties of $\mathrm{YFe_{11-x}Si_xTi}$ ($x \leq 2$). *Journal of Magnetism and Magnetic Materials*, 242:823–825, 2002.

[20] Z. Y. Ren, D. H. L. Ng, and S. Y. Dai. Structural and magnetic properties of $\mathrm{Sm_2Fe_{16}MAl_2}$/(M = Mn, Mo, Ni) and their carbides. *IEEE Transactions on Magnetics*, 36(5):3330–3332, 2000.

[21] J. M. D. Coey. *Rare-earth Iron Permanent Magnets*. Oxford University Press, 1996.

[22] X. C. Kou, R. Grössinger, G. Wiesinger, J. P. Liu, F. R. De Boer, I. Kleinschroth, and H. Kronmüller. Intrinsic magnetic properties of $\mathrm{RFe_{10}Mo_2}$ compounds (R = Y, Pr, Nd, Sm, Gd, Tb, Dy, Ho, Er or Tm). *Physical Review B*, 51(13):8254–8265, 1995.

[23] A. M. Gabay and G. C. Hadjipanayis. $\mathrm{ThMn_{12}}$-type structure and uniaxial magnetic anisotropy in $\mathrm{ZrFe_{10}Si_2}$ and $\mathrm{Zr_{1-x}Ce_xFe_{10}Si_2}$ alloys. *Journal of Alloys and Compounds*, 657:133–137, 2016.

[24] K. H. J. Buschow. Permanent magnet materials based on tetragonal rare earth compounds of the type $\mathrm{RFe_{12-x}M_x}$. *Journal of Magnetism and Magnetic Materials*, 100(1–3):79–89, 1991.

[25] G. C. Hadjipanayis. A search for new Fe-rich phases for the development of permanent magnets. In I. V. Mitchell, J. M. D. Coey, D. Givord, I. R. Harris, and R. Hanitsch, editors, *Concerted European Action on Magnets (CEAM)*, pages 122–129. Springer Netherlands, 1989.

[26] J. Strzeszewski, Y. Z. Wang, E. W. Singleton, and G. C. Hadjipanayis. High coercivity in $\mathrm{Sm(FeT)_{12}}$ type magnets. *IEEE Transactions on Magnetics*, 25(5):3309–3311, 1989.

[27] A. M. Gabay, A. Martín-Cid, J. M. Barandiaran, D. Salazar, and G. C. Hadjipanayis. Low-cost $\mathrm{Ce_{1-x}Sm_x(Fe, Co, Ti)_{12}}$ alloys for permanent magnets. *AIP Advances*, 6(5):056015, 2016.

[28] H. Wüst, L. Bommer, A. M. Huber, D. Goll, T. Weissgärber, and B. Kieback. Preparation of nanocrystalline $\mathrm{Ce_{1-x}Sm_x(Fe, Co)_{11}Ti}$ by melt spinning and mechanical alloying. *Journal of Magnetism and Magnetic Materials*, 428:194–197, 2017.

[29] A. M. Gabay and G. C. Hadjipanayis. Recent developments in $\mathrm{RFe_{12}}$-type compounds for permanent magnets. *Scripta Materialia*, 154:284–288, 2018.

[30] A. Martín-Cid, A. M. Gabay, D. Salazar, J. M. Barandiaran, and G. C. Hadjipanayis. Tetragonal Ce-based Ce-Sm$(\mathrm{Fe}, \mathrm{Co}, \mathrm{Ti})_{12}$ alloys for permanent magnets. *Physica Status Solidi (c)*, 13(10–12):962–964, 2016.

[31] A. Martín-Cid, D. Salazar, A. M. Schönhöbel, J. S. Garitaonandia, J. M. Barandiaran, and G. C. Hadjipanayis. Magnetic properties and phase stability of tetragonal $\mathrm{Ce_{1-x}Sm_xFe_9Co_2Ti}$ 1:12 phase for permanent magnets. *Journal of Alloys and Compounds*, 749:640–644, 2018.

[32] C. Zhou and F. E. Pinkerton. Magnetic properties of Ce-Nd-Fe-Mo alloys and their nitrides. *Journal of Magnetism and Magnetic Materials*, 369:127–131, 2014.

[33] G. P. Hatch. Critical rare earths - Global supply & demand projections and the leading contenders for new sources of supply. *Technology Metals Research*, 2011.

[34] Y. Kato, K. Fujinaga, K. Nakamura, Y. Takaya, K. Kitamura, J. Ohta, R. Toda, T. Nakashima, and H. Iwamori. Deep-sea mud in the pacific ocean as a potential resource for rare-earth elements. *Nature Geoscience*, 4(8):535–539, 2011.

[35] D. Goll, R. Löffler, D. Hohs, and G. Schneider. Reaction sintering as a high-throughput approach for magnetic materials development. *Scripta Materialia*, 146:355–361, 2018.

[36] S. Ener, J. Kroder, K. P. Skokov, and O. Gutfleisch. The search for room temperature tetragonal phases of $\mathrm{Fe-Mn-Ga}$: A reactive crucible melting approach. *Journal of Alloys and Compounds*, 683:198–204, 2016.

[37] D. Goll, R. Löffler, J. Herbst, R. Karimi, and G. Schneider. High-throughput search for new permanent magnet materials. *Journal of Physics: Condensed Matter*, 26(6):064208, 2014.

[38] D. Goll, R. Löffler, J. Herbst, R. Karimi, U. Pflanz, R. Stein, and G. Schneider. High-throughput methods for searching new permanent magnet materials. *IEEE Transactions on Magnetics*, 50(11):1–7, 2014.

[39] R. Löffler, D. Goll, J. Herbst, and G. Schneider. Determination of the intrinsic properties of hard magnetic phases from their domain structure as a function of temperature. In *IEEE International Magnetics Conference 2014*, 2014.

[40] F. Groß. *Search for new permanent magnetic phases by the reaction crucible analysis and development of new high throughput methods*. PhD thesis, University of Birmingham, 2004.

[41] V. Raghavan. The Fe-Ti-V (iron-titanium-vanadium) system. In *Phase Diagrams of Ternary Iron Alloys*, pages 73–84. ASM International, Indian Institute of Metals, 1987.

[42] V. Raghavan. The Al-Fe-Sm (aluminium-iron-samarium) system. In *Phase Diagrams of Ternary Iron Alloys*, pages 178–182. ASM International, Indian Institute of Metals, 1992.

[43] V. Raghavan. The Al-Fe-Mo (aluminium-iron-molybdenum) system. In *Phase Diagrams of Ternary Iron Alloys*, pages 135–141. ASM International, Indian Institute of Metals, 1992.

[44] M. Anagnostou, C. Christides, and D. Niarchos. Nitrogenation of the $RFe_{10}Mo_2$ (R = rare earth) compounds with $ThMn_{12}$ type structure. *Solid state communications*, 78(8):681–684, 1991.

[45] S. Khazzan, N. Mliki, and L. Bessais. Structure and magnetic properties of nanocrystalline $Sm_{1-s}(Fe,Mo)_{5+2s}$. *Journal of Applied Physics*, 105(10):103904, 2009.

[46] J. Hu, Y. Wang, R. Zhao, T. Ning, Z. Wang, and X. Yang. Structure and magnetocrystalline anisotropy of $SmMo_2Fe_{10}$ alloy. *Solid State Communications*, 70(11):983–985, 1989.

[47] Z. Wang and R. A. Dunlap. Effects of Al substitutions on the magnetic anisotropy of Sm_2Fe_{17} compounds. *Journal of Physics: Condensed Matter*, 5(15):2407–2414, 1993.

[48] Z. Cheng, B. Shen, Q. Yan, H. Guo, D. Chen, C. Gou, K. Sun, F. R. De Boer, and K. H. J. Buschow. Structure, exchange interactions and magnetic phase transition of $Er_2Fe_{17-x}Al_x$ intermetallic compounds. *Physical Review B*, 57(22):14299, 1998.

[49] A. Teresiak, M. Kubis, N. Mattern, K. H. Müller, and B. Wolf. Crystal structure of $Sm_2Fe_{17-y}M_y$ compounds with M = Al, Si, Ga. *Journal of Alloys and Compounds*, 319(1):168–173, 2001.

[50] T. Yanson, M. Manyako, O. Bodak, R. Cerny, and K. Yvon. Effect of aluminum substitution and rare-earth content on the structure of $R_2(Fe_{1-x}Al_x)_{17}$ (R = Tb, Dy, Ho, Er) phases. *Journal of Alloys and Compounds*, 320(1):108–113, 2001.

[51] X. F. Liu, J. Y. Lv, Z. B. Hu, S. B. Han, D. F. Chen, Y. J. Xue, J. H. Li, R. Kiyanagi, J. S. Fieramosca, and S. Short. Effects of the substitution of Al for Fe on phase transition, crystal structures, and magnetic properties of $Nd_3(Fe,Ti)_{29}$-type intermetallics. *Journal of Applied Physics*, 100(10):103910, 2006.

[52] J. M. D. Coey. *Magnetism and Magnetic Materials*. Cambridge University Press, 2010.

[53] B. D. Cullity and C. D. Graham. *Introduction to Magnetic Materials*. John Wiley & Sons, 2011.

[54] R. C. O'Handley. *Modern Magnetic Materials: Principles and Applications*. Wiley, 2000.

[55] L. Zhou, M. K. Miller, P. Lu, L. Ke, R. Skomski, H. Dillon, Q. Xing, A. Palasyuk, M. R. McCartney, D. J. Smith, S. Constantinides, R. W. McCallum, I. E. Anderson, V. Antropov, and M. J. Kramer. Architecture and magnetism of AlNiCo. *Acta Materialia*, 74:224–233, 2014.

[56] L. Zhou, W. Guo, J. D. Poplawsky, L. Ke, W. Tang, I. E. Anderson, and M. J. Kramer. On spinodal decomposition in AlNiCo - A transmission electron microscopy and atom probe tomography study. *Acta Materialia*, 153:15–22, 2018.

[57] W. F. Brown Jr. Virtues and weaknesses of the domain concept. *Reviews of Modern Physics*, 17(1):15–19, 1945.

[58] K. P. Skokov and O. Gutfleisch. Heavy rare earth free, free rare earth and rare earth free magnets-Vision and reality. *Scripta Materialia*, 154:289–294, 2018.

[59] K. J. Strnat. The recent development of permanent magnet materials containing rare earth metals. *IEEE Transactions on Magnetics*, 6(2):182–190, 1970.

[60] L. Schultz, K. Schnitzke, and J. Wecker. Preparation and properties of mechanically alloyed rare earth permanent magnets. *Journal of Magnetism and Magnetic Materials*, 80(1):115–118, 1989.

[61] D. Brown, B. Ma, and Z. Chen. Developments in the processing and properties of NdFeB-type permanent magnets. *Journal of Magnetism and Magnetic Materials*, 248(3):432–440, 2002.

[62] O. Gutfleisch. Controlling the properties of high energy density permanent magnetic materials by different processing routes. *Journal of Physics D: Applied Physics*, 33(17):R157, 2000.

[63] A. Kirchner, D. Hinz, V. Panchanathan, O. Gutfleisch, K. H. Müller, and L. Schultz. Improved hot workability and magnetic properties in NdFeCoGaB hot deformed magnets. *IEEE Transactions on Magnetics*, 36(5):3288–3290, 2000.

[64] J. H. Vincent and M. D. Wyborn. The production of NdFeB magnets by the rapid solidification processing route. pages 563–576. Springer Netherlands, 1989.

[65] A. Bollero, B. Gebel, O. Gutfleisch, K. H. Müller, L. Schultz, P. J. McGuiness, G. Drazic, and S. Kobe. NdDyFeBZr high-coercivity powders prepared by intensive milling and the HDDR process. *Journal of Alloys and Compounds*, 315(1–2):243–250, 2001.

[66] C. Suryanarayana. Mechanical alloying and milling. *Progress in Materials Science*, 46(1–2):1–184, 2001.

[67] M. Sagawa, S. Fujimura, H. Yamamoto, Y. Matsuura, and K. Hiraga. Permanent magnet materials based on the rare earth-iron-boron tetragonal compounds. *IEEE Transactions on Magnetics*, 20(5):1584–1589, 1984.

[68] H. Sepehri-Amin, Y. Une, T. Ohkubo, K. Hono, and M. Sagawa. Microstructure of fine-grained $Nd-Fe-B$ sintered magnets with high coercivity. *Scripta Materialia*, 65(5):396–399, 2011.

[69] G. Schneider, E. T. Henig, G. Petzow, and F. P. Missell. Microstructure of sintered Fe-Nd-B magnets. *Zeitschrift für Metallkunde*, 81(5):322–329, 1990.

[70] A. Malfliet, G. Cacciamani, N. Lebrun, and P. Rogl. Boron - iron - neodymium. In *Iron Systems, Part 1*, pages 482–511. Springer, 2008.

[71] R. M. German, P. Suri, and S. J. Park. Review: Liquid phase sintering. *Journal of Materials Science*, 44(1):1–39, 2009.

[72] W. Fernengel, A. Lehnert, M. Katter, W. Rodewald, and B. Wall. Examination of the degree of alignment in sintered Nd-Fe-B magnets by measurements of the remanent polarizations. *Journal of Magnetism and Magnetic Materials*, 157:19–20, 1996.

[73] W. Rodewald, M. Katter, B. Wall, R. Blank, G. W. Reppel, and H. D. Zilg. Dependence of the coercivity H_{cJ} of high energy Nd-Fe-B magnets on the alignment coefficient. *IEEE Transactions on Magnetics*, 36(5):3279–3281, 2000.

[74] M. Sagawa. Development and prospect of the Nd-Fe-B sintered magnets. In *Proceedings of the 21th Workshop on REPM and Their Applications*, pages 183–186, 2010.

[75] O. Gutfleisch, A. Kirchner, W. Grünberger, D. Hinz, H. Nagel, P. Thompson, J. N. Chapman, K. H. Müller, L. Schultz, and I. R. Harris. Textured NdFeB HDDR magnets produced by die-upsetting and backward extrusion. *Journal of Physics D: Applied Physics*, 31(7):807–811, 1998.

[76] M. Jurczyk, J. S. Cook, and S. J. Collocott. Application of high energy ball milling to the production of magnetic powders from NdFeB-type alloys. *Journal of Alloys and Compounds*, 217(1):65–68, 1995.

[77] D. N. Brown, Z. Wu, F. He, D. J. Miller, and J. W. Herchenröder. Dysprosium-free melt-spun permanent magnets. *Journal of Physics: Condensed Matter*, 26(6):064202, 2014.

[78] W. Grünberger, D. Hinz, A. Kirchner, K. H. Müller, and L. Schultz. Hot deformation of nanocrystalline Nd-Fe-B alloys. *Journal of Alloys and Compounds*, 257(1–2):293–301, 1997.

[79] G. C. Hadjipanayis. Nanophase hard magnets. *Journal of Magnetism and Magnetic Materials*, 200(1–3):373–391, 1999.

[80] J. Bauer. *Nanokristalline austauschgekoppelte Dauermagnete auf Seltenerdmetall-Basis*. Mainz, 1995.

[81] A. M. Gabay, Y. Zhang, and G. C. Hadjipanayis. Effect of Cu and Ga additions on the anisotropy of $R_2Fe_{14}B/\alpha$-Fe nanocomposite die-upset magnets (R=Pr, Nd). *Journal of Magnetism and Magnetic Materials*, 302(1):244–251, 2006.

[82] S. Sawatzki. *Der Korngrenzendiffusionsprozess in nanokristallinen Nd-Fe-B-Permanentmagneten*. PhD thesis, Technische Universität Darmstadt, 2015.

[83] B. Grieb. New corrosion resistant materials based on neodym-iron-boron. *IEEE Transactions on Magnetics*, 33(5):3904–3906, 1997.

[84] P. Tenaud, A. Chamberod, and F. Vanoni. Texture in Nd-Fe-B magnets analysed on the basis of the determination of $Nd_2Fe_{14}B$ single crystals easy growth axis. *Solid State Communications*, 63(4):303–305, 1987.

[85] L. Li and C. D. Graham Jr. Mechanism of texture formation by hot deformation in rapidly quenched FeNdB. *Journal of Applied Physics*, 67(9):4756–4758, 1990.

[86] R. K. Mishra. Microstructure of melt-spun Nd-Fe-B magnequench magnets. *Journal of Magnetism and Magnetic Materials*, 54–57, Part 1(0):450–456, 1986.

[87] W. Grünberger. The solution-precipitation creep - A model for deformation and texturing mechanisms of nanocrystalline NdFeB alloys. In *Proceedings of the 15th International Workshop on Rare Earth Magnets and Their Applications*, pages 333–348, 1998.

[88] O. Gutfleisch, A. Bollero, A. Handstein, D. Hinz, A. Kirchner, A. Yan, K. H. Müller, and L. Schultz. Nanocrystalline high performance permanent magnets. *Journal of Magnetism and Magnetic Materials*, 242:1277–1283, 2002.

[89] L. Li and C. D. Graham. The origin of crystallographic texture produced during hot deformation in rapidly-quenched NdFeB permanent magnets. *IEEE Transactions on Magnetics*, 28(5):2130–2132, 1992.

[90] H. Kronmüller, R. Fischer, R. Hertel, and T. Leineweber. Micromagnetism and the microstructure in nanocrystalline materials. *Journal of Magnetism and Magnetic Materials*, 175(1–2):177–192, 1997.

[91] K. D. Durst and H. Kronmüller. The coercive field of sintered and melt-spun NdFeB magnets. *Journal of Magnetism and Magnetic Materials*, 68(1):63–75, 1987.

[92] S. Sugimoto, A. Kojima, M. Okada, and M. Homma. Enhancement of magnetic properties of $\mathrm{Sm(Fe,Co,Ti)_{12}}$ melt-spun ribbons by refining crystallized grains. *Materials Transactions, JIM*, 32:1180–1183, 1991.

[93] J.D. Livingston. A review of coercivity mechanisms. *Journal of Applied Physics*, 52(3):2544–2548, 1981.

[94] R. Skomski. Domain-wall curvature and coercivity in pinning type Sm-Co magnets. *Journal of Applied Physics*, 81(8):5627–5629, 1997.

[95] J. Zhou, R. Skomski, C. Chen, G. C. Hadjipanayis, and D. J. Sellmyer. $Sm-Co-Cu-Ti$ high-temperature permanent magnets. *Applied Physics Letters*, 77(77):1514–1516, 2000.

[96] R. Fischer, T. Schrefl, H. Kronmüller, and J. Fidler. Grain-size dependence of remanence and coercive field of isotropic nanocrystalline composite permanent magnets. *Journal of Magnetism and Magnetic Materials*, 153(1–2):35–49, 1996.

[97] T. G. Woodcock, Y. Zhang, G. Hrkac, G. Ciuta, N. M. Dempsey, T. Schrefl, O. Gutfleisch, and D. Givord. Understanding the microstructure and coercivity of high performance NdFeB-based magnets. *Scripta Materialia*, 67(6):536–541, 2012.

[98] Y. Gao, J. Zhu, Y. Weng, E. B. Park, and C. J. Yang. The enhanced exchange coupled interaction in nanocrystalline $\mathrm{Nd_2Fe_{14}B/Fe_3B} + \alpha-\mathrm{Fe}$ alloys with improved microstructure. *Journal of Magnetism and Magnetic Materials*, 191(1–2):146–152, 1999.

[99] J. Luo, J. K. Liang, Y. Q. Guo, Q. L. Liu, F. S. Liu, Y. Zhang, L. T. Yang, and G. H. Rao. Effects of the doping element on crystal structure and magnetic properties of $\mathrm{Sm(Co,M)_7}$ compounds (M=Si, Cu, Ti, Zr, and Hf). *Intermetallics*, 13(7):710–716, 2005.

[100] E.C. Stoner and E.P. Wohlfarth. A mechanism of magnetic hysteresis in heterogeneous alloys. *Philosophical Transactions of the Royal Society of London A: Mathematical, Physical and Engineering Sciences*, 240(826):599–642, 1948.

[101] J. Pastushenkov, K. D. Durst, and H. Kronmüller. Domain observations under applied fields of sintered $\mathrm{Fe_{77}Nd_{15}B_8}$ permanent magnets. *Physica Status Solidi (a)*, 104(1):487–495, 1987.

[102] E. F. Kneller and R. Hawig. The exchange-spring magnet: A new material principle for permanent magnets. *IEEE Transactions on Magnetics*, 27(4):3588–3560, 1991.

[103] J. Bernardi, T. Schrefl, J. Fidler, T. Rijks, K. De Kort, V. Archambault, D. Péré, S. David, D. Givord, J. F. O'Sullivan, P. A. I. Smith, J. M. D. Coey, U. Czernik, and M. Grönefeld. Preparation, magnetic properties and microstructure of lean rare-earth permanent magnetic materials. *Journal of Magnetism and Magnetic Materials*, 219(2):186–198, 2000.

[104] P. Crespo, V. Neu, and L. Schultz. Mechanically alloyed nanocomposite powders of $Nd_2Fe_{14}B/\alpha - Fe$ with additional elements. *Journal of Physics D: Applied Physics*, 30(16):2298–2303, 1997.

[105] Y. Li, B. Li, M. Yue, and J. Zhang. Preparation and properties of Nd-Fe-B/Fe nanocomposite magnets. *Journal of Iron and Steel Research, International*, 13, Supplement 1:187–191, 2006.

[106] S. Hirosawa, H. Kanekiyo, T. Miyoshi, K. Murakami, Y. Shigemoto, and T. Nishiuch. Structure and magnetic properties of $Nd_2Fe_{14}B/Fe_xB$-type nanocomposites prepared by strip casting. *IEEE Transactions on Magnetics*, 40(4):2883–2885, 2004.

[107] I.B. De Lima and W. Leal Filho. *Rare earths industry: Technological, economic, and environmental implications*. Elsevier, 2015.

[108] J. C. G. Bünzli and V. K. Pecharsky. *Handbook on the Physics and Chemistry of Rare Earths*. North-Holland, 2015.

[109] F. E. Pinkerton, C. Zhou, and J. F. Herbst. Exploring new permanent magnet materials for high power applications. In *2014 International Conference on NdFeB Magnets: Supply Chain, Critical Properties & Applications*, 2014.

[110] U.S. Department of the Interior and U.S. Geological Survey. *Mineral Commodity Summaries 2016*. Government Printing Office, 2016.

[111] O. Gutfleisch. Presentation slides, European School on Magnetism 2013. 2013.

[112] L. Hook. China tightens grip on output of rare earths. *Financial Times*, 2010.

[113] R. Skomski and J. M. D. Coey. *Permanent Magnetism*. IOP Publishing, 1999.

[114] R. Skomski. *Simple Models of Magnetism*. Oxford University Press, 2008.

[115] A. N. Nesmeyanov. *Vapor Pressure of the Chemical Elements*. Elsevier, 1963.

[116] S. Gao, M. Affronte, M. L. Baker, S. Blundell, L. Bogani, L. F. Chibotaru, R. Clérac, A. Cornia, C. Coulon, and N. Domingo. *Molecular Nanomagnets and Related Phenomena*. Springer, 2015.

[117] H. W. De Wijn, A. M. Van Diepen, and K. H. J. Buschow. Samarium in crystal fields, a case of strong J-mixing. *Physica Status Solidi (b)*, 76(1):11–30, 1976.

[118] J. M. D. Coey, H. S. Li, J. P. Gavigan, J. M. Cadogan, and B. P. Hu. Intrinsic magnetic properties of iron-rich compounds with the $Nd_2Fe_{14}B$ or $ThMn_{12}$ structure. In I. V. Mitchell, J. M. D. Coey, D. Givord, I. R. Harris, and R. Hanitsch, editors, *Concerted European Action on Magnets (CEAM)*, pages 76–97. Springer Netherlands, 1989.

[119] J. M. D. Coey and H. Sun. Improved magnetic properties by treatment of iron-based rare earth intermetallic compounds in ammonia. *Journal of Magnetism and Magnetic Materials*, 87(3):L251–L254, 1990.

[120] R. Verhoef, F. R. De Boer, Z. Zhi-dong, and K. H. J. Buschow. Moment reduction in $RFe_{12-x}T_x$ compounds (R=Gd, Y and T=Ti, Cr, V, Mo, W). *Journal of Magnetism and Magnetic Materials*, 75(3):319–322, 1988.

[121] L. Schultz, K. Schnitzke, and J. Wecker. High coercivity in mechanically alloyed Sm-Fe-V magnets with a $ThMn_{12}$ crystal structure. *Applied Physics Letters*, 56(9):868–870, 1990.

[122] K. H. J. Buschow. Magnetovolume effects in ternary compounds of the type $RFe_{12-x}T_x$ and $R_2Fe_{14}C$ (R = rare earth, T = Ti, V, Cr, Mo, W, Si). *Journal of the Less Common Metals*, 144(1):65–69, 1988.

[123] C. Zhou and F. E. Pinkerton. Magnetic hardening of $CeFe_{12-x}Mo_x$ and the effect of nitrogenation. *Journal of Alloys and Compounds*, 583(0):345–350, 2014.

[124] R. Grossinger, X. C. Kou, and G. Wiesinger. Magnetic anisotropy and magnetic phase transition of $RFe_{12-x}M_x$ (M= Ti or V). *IEEE Transactions on Magnetics*, 30(2):1018–1020, 1994.

[125] F. R. De Boer, Y. K. Huang, D. B. De Mooij, and K. H. J. Buschow. Magnetic properties of a series of novel ternary intermetallics ($RFe_{10}V_2$). *Journal of the Less Common Metals*, 135(2):199–204, 1987.

[126] C. M. Varma. Mixed-valence compounds. *Reviews of Modern Physics*, 48(2):219–238, 1976.

[127] J. M. Cadogan, D. H. Ryan, O. Moze, I. P. Swainson, and K. Suzuki. Noncollinearity of the magnetic structure of $TbFe_{10}V_2$. *Journal of Applied Physics*, 93(10):6972–6974, 2003.

[128] M. Melamud, L. H. Bennett, and R. E. Watson. Where are the iron atoms and iron moments in RFe_nAl_{12-n}? A Wigner-Seitz analysis. *Journal of Applied Physics*, 61(8):4246–4248, 1987.

[129] C. Piquer, O. Isnard, F. Grandjean, and G. J. Long. Magnetic and Mössbauer spectral properties of $DyFe_{11}Ti$ and $DyFe_{11}TiH$. *Journal of Magnetism and Magnetic Materials*, 265(2):156–166, 2003.

[130] Y. Yu, W. Xue-Feng, and J. Han-Min. The anisotropic Dy-Fe exchange interaction in $Dy(Fe_{11}Ti)$. *Journal of Physics: Condensed Matter*, 6(10):2077–2082, 1994.

[131] H. T. Kim, Y. B. Kim, C. S. Kim, and H. Jin. Magnetocrystalline anisotropy of $(Sm_{0.5}RE_{0.5})Fe_{11}Ti$ compounds (RE = Ce, Pr, Nd, Sm, Gd and Tb). *Journal of Magnetism and Magnetic Materials*, 152(3):387–390, 1996.

[132] B. P. Hu, H. S. Li, J. P. Gavigan, and J. M. D. Coey. Intrinsic magnetic properties of the iron-rich $ThMn_{12}$-structure alloys $R(Fe_{11}Ti)$; R= Y, Nd, Sm, Gd, Tb, Dy, Ho, Er, Tm and Lu. *Journal of Physics: Condensed Matter*, 1(4):755–770, 1989.

[133] X. C. Kou, T. S. Zhao, R. Grössinger, H. R. Kirchmayr, X. Li, and F. R. De Boer. Magnetic phase transitions, magnetocrystalline anisotropy, and crystal-field interactions in the $RFe_{11}Ti$ series (where R= Y, Pr, Nd, Sm, Gd, Tb, Dy, Ho, Er, or Tm). *Physical Review B*, 47(6):3231–3242, 1993.

[134] S. Obbade, D. Fruchart, M. Bououdina, S. Miraglia, J. L. Soubeyroux, and O. Isnard. About hydrogen insertion in $ThMn_{12}$ type alloys. *Journal of Alloys and Compounds*, 253:298–301, 1997.

[135] S. A. Nikitin, I. S. Tereshina, V. N. Verbetsky, and A. A. Salamova. Magnetic anistropy of $YFe_{11}Ti$ single crystal and its hydride. *International Journal of Hydrogen Energy*, 24(2–3):217–219, 1999.

[136] C. Zhou, F. E. Pinkerton, and J. F. Herbst. Magnetic properties of $CeFe_{11-x}Co_xTi$ with $ThMn_{12}$ structure. *Journal of Applied Physics*, 115(17):17C716, 2014.

[137] O. Isnard, S. Miraglia, M. Guillot, and D. Fruchart. Hydrogen effects on the magnetic properties of $RFe_{11}Ti$ compounds. *Journal of Alloys and Compounds*, 275:637–641, 1998.

[138] S. A. Nikitin, I. S. Tereshina, V. N. Verbetsky, and A. A. Salamova. Transformations of magnetic phase diagram as a result of insertion of hydrogen and nitrogen atoms in crystalline lattice of $RFe_{11}Ti$ compounds. *Journal of Alloys and Compounds*, 316(1–2):46–50, 2001.

[139] N. Tajabor, D. Fruchart, D. Gignoux, S. Miraglia, and L. Motevalizadeh. Spin reorientation and first-order magnetisation process in $HoFe_{11-x}Co_xTi$ compounds. *Journal of Magnetism and Magnetic Materials*, 314(2):122–127, 2007.

[140] R. Grössinger, R. Krewenka, and K. H. J. Buschow. Note on the anisotropy fields in tetragonal $RFe_{10}V_2$ compounds. *Journal of Alloys and Compounds*, 186(2):L11–L15, 1992.

[141] M. Jurczyk. Magnetic and crystallographic properties of $SmFe_{10-x}Co_xV_2$ compounds. *Journal of the Less Common Metals*, 162(1):149–154, 1990.

[142] Y. Z. Wang, G. C. Hadjipanayis, A. Kim, D. J. Sellmyer, and W. B. Yelon. Structure and magnetic properties of $RFe_{10}V_2N_x$ compounds. *Journal of Magnetism and Magnetic Materials*, 104:1132–1134, 1992.

[143] P. Bruno. Physical origins and theoretical models of magnetic anisotropy. *Magnetismus von Festkörpern und Grenzflächen*, 24:1–28, 1993.

[144] K. J. Strnat, G. Hoffer, and A. E. Ray. Magnetic properties of rare–Earth–Iron intermetallic compounds. *IEEE Transactions on Magnetics*, 2(3):489–493, 1966.

[145] R. Vert, D. Fruchart, B. Garcia-Landa, D. Gignoux, and Y. Amako. Magnetic properties of $RFe_{12-x}Mo_x$ compounds with R=Y, Gd, Ho, Er versus the molybdenum content. *Journal of Alloys and Compounds*, 275(0):611–614, 1998.

[146] L. Schultz, K. Schnitzke, J. Wecker, and M. Katter. High coercivities in mechanically alloyed Sm-Fe-X magnets. *Materials Science and Engineering: A*, 133(0):143–146, 1991.

[147] J. Wecker, M. Katter, and L. Schultz. High coercivity in Sm-Fe-Ti alloys by rapid solidification. *Materials Science and Engineering: A*, 133(0):147–150, 1991.

[148] S. F. Cheng, V. K. Sinha, Y. Xu, J. M. Elbicki, E. B. Boltich, W. E. Wallace, S. G. Sankar, and D. E. Laughlin. Magnetic and structural properties of $\mathrm{SmTiFe_{11-x}Co_x}$ alloys. *Journal of Magnetism and Magnetic Materials*, 75(3):330–338, 1988.

[149] S. Khazzan, N. Mliki, and L. Bessais. Structural and magnetic investigation on tetragonal R – Fe alloy with 1:12 stoechiometry. In *IOP Conference Series: Materials Science and Engineering*, page 012020, 2012.

[150] T. Saito, F. Watanabe, and D. Nishio-Hamane. Magnetic properties of $\mathrm{SmFe_{12}}$-based magnets produced by spark plasma sintering method. *Journal of Alloys and Compounds*, 773:1018–1022, 2019.

[151] A. V. Andreev, S. V. Andreev, and E. N. Tarasov. Magnetic properties of $\mathrm{UFe_{12-x}Si_x}$. *Journal of the Less Common Metals*, 167(2):255–259, 1991.

[152] B. Reinsch, B. Grieb, E. T. Henig, and G. Petzow. Phase relations in the system Sm-Fe-Ti and the consequences for the production of permanent magnets. *IEEE Transactions on Magnetics*, 28(5):2832–2834, 1992.

[153] J. Kerr. XLIII. On rotation of the plane of polarization by reflection from the pole of a magnet. *The London, Edinburgh and Dublin Philosophical Magazine and Journal of Science*, 3(19):321–343, 1877.

[154] A. Hubert and R. Schäfer. *Magnetic domains: The analysis of magnetic microstructures*. Springer Science & Business Media, 2008.

[155] J. McCord. Progress in magnetic domain observation by advanced magneto-optical microscopy. *Journal of Physics D: Applied Physics*, 48(33):333001, 2015.

[156] J. McCord. Presentation slides, IEEE Summer School 2017. 2017.

[157] D. Nunes, R. Colaço, J. T. M. De Hosson, A. P. Gonçalves, L. C. J. Pereira, and P. A. Carvalho. Magnetic microstructure of $\mathrm{YFe_{11}Ti}$ aggregates. *Journal of Alloys and Compounds*, 487(1–2):11–17, 2009.

[158] D. Halliday, R. Resnick, J. Walker, and S.W. Koch. *Halliday Physik*. Wiley, 2009.

[159] R. Bodenberger and A. Hubert. Zur Bestimmung der Blochwandenergie von einachsigen Ferromagneten. *Physica Status Solidi (a)*, 44(1):K7–K11, 1977.

[160] J.J. Croat. Current status and future outlook for bonded neodymium permanent magnets. *Journal of Applied Physics*, 81(8):4804–4809, 1997.

[161] Q. Zeng, A. M. Gabay, Y. Zhang, and G. C. Hadjipanayis. Fully dense Sm-Co-Fe-Cu and Sm-Co-Fe-Ga nanocomposite magnets by hot compaction. *IEEE Transactions on Magnetics*, 40(4):2916–2918, 2004.

[162] G. Bai, R. W. Gao, Y. Sun, G. B. Han, and B. Wang. Study of high-coercivity sintered NdFeB magnets. *Journal of Magnetism and Magnetic Materials*, 308(1):20–23, 2007.

[163] G. Kresse, M. Marsman, and J. Furthmüller. *Vienna Ab initio Simulation Package (VASP), The Guide - Computational Materials Physics*. Faculty of Physics, Universität Wien, 2014.

[164] G. Pizzi, A. Cepellotti, R. Sabatini, N. Marzari, and B. Kozinsky. AiiDA: Automated interactive infrastructure and database for computational science. *Computational Materials Science*, 111:218–230, 2016.

[165] J. P. Perdew. Electronic structure of solids' 91. In *Proceedings of the 75. WE-Heraeus-Seminar and 21st Annual International Symposium on Electronic Structure of Solids*, page 244, 1991.

[166] G. Kresse and D. Joubert. From ultrasoft pseudopotentials to the projector augmented-wave method. *Physical Review B*, 59(3):1758–1775, 1999.

[167] P. Scherrer. Bestimmung der inneren Struktur und der Größe von Kolloidteilchen mittels Röntgenstrahlen. In R. Zsigmondy, editor, *Kolloidchemie Ein Lehrbuch*, pages 387–409. Springer, 1912.

[168] K. Mishima and T. Hibiki. Quantitative limits of thermal and fluid phenomena measurements using the neutron attenuation characteristics of materials. *Experimental Thermal and Fluid Science*, 12(4):461–472, 1996.

[169] M. Hölzel, A. Senyshyn, and O. Dolotko. SPODI: High resolution powder diffractometer. *Journal of Large-Scale Research Facilities*, 1:5, 2015.

[170] F. Bolzoni and R. Cabassi. Review of singular point detection techniques. *Physica B: Condensed Matter*, 346:524–527, 2004.

[171] A. M. Gabay, R. Cabassi, S. Fabbrici, F. Albertini, and G. C. Hadjipanayis. Structure and permanent magnet properties of $Zr_{1-x}R_xFe_{10}Si_2$ alloys with R= Y, La, Ce, Pr and Sm. *Journal of Alloys and Compounds*, 683:271–275, 2016.

[172] G. Asti and S. Rinaldi. Singular points in the magnetization curve of a polycrystalline ferromagnet. *Journal of Applied Physics*, 45(8):3600–3610, 1974.

[173] *Magnetische Werkstoffe - Teil 5: Dauermagnetwerkstoffe (hartmagnetische Werkstoffe) - Verfahren zur Messung der magnetischen Eigenschaften (IEC 60404-5:2015)*. DIN e.V., Beuth Verlag GmbH, 2015.

[174] S. Khazzan, L. Bessais, G. Van Tendeloo, and N. Mliki. Correlation between the nanocrystalline $Sm(Fe, Mo)_{12}$ and its out of equilibrium phase $Sm(Fe, Mo)_{10}$. *Journal of Magnetism and Magnetic Materials*, 363(0):125–132, 2014.

[175] K. H. J. Buschow, J. H. N. Van Vucht, and W. W. Van Den Hoogenhof. Note on the crystal structure of the ternary rare earth-3d transition metal compounds of the type RT_4Al_8. *Journal of the Less Common Metals*, 50(1):145–150, 1976.

[176] J. A. Paixao, M. R. Silva, S. A. Sørensen, B. Lebech, G. H. Lander, P. J. Brown, S. Langridge, E. Talik, and A. P. Gonçalves. Neutron-scattering study of the magnetic structure of $DyFe_4Al_8$ and $HoFe_4Al_8$. *Physical Review B*, 61(9):6176–6188, 2000.

[177] Y. G. Xiao, G. H. Rao, Q. Zhang, J. Luo, G. Y. Liu, Y. Zhang, and J. K. Liang. Formation, structure and magnetic properties of $TbFe_{12-x}Mo_x$ (x=0.5-3.0) compounds. *Physica B: Condensed Matter*, 369(1):56–63, 2005.

[178] O. Isnard and M. Guillot. Investigation of the magnetic properties of $SmFe_{10}Mo_2$ and $SmFe_{10}Mo_2H$ in high magnetic field. *Journal of Applied Physics*, 85(8):4681–4683, 1999.

[179] A. Saccone, G. Cacciamani, D. Maccio, G. Borzone, and R. Ferro. Contribution to the study of the alloys and intermetallic compounds of aluminium with the rare-earth metals. *Intermetallics*, 6(3):201–215, 1998.

[180] Z. Cheng, B. Shen, J. Zhang, F. Wang, H. Gong, B. Liang, and W. Zhan. Effect of Al on the formation and magnetic properties of $Sm_2Fe_{17}C_x$ (x=0-2.5) prepared by arc-melting. *Journal of Magnetism and Magnetic Materials*, 140:1075–1076, 1995.

[181] E. J. W. Whittaker and R. Muntus. Ionic radii for use in geochemistry. *Geochimica et Cosmochimica Acta*, 34(9):945–956, 1970.

[182] C. K. Loong, S. M. Short, J. Lin, and Y. Ding. A study of nitrogenation of a $NdFe_{12-x}Mo_x$ compound by in situ neutron powder diffraction. *Journal of Applied Physics*, 83(11):6926–6928, 1998.

[183] K. Ohashi, Y. Tawara, R. Osugi, and M. Shimao. Magnetic properties of Fe-rich rare-earth intermetallic compounds with a $ThMn_{12}$ structure. *Journal of Applied Physics*, 64(10):5714–5716, 1988.

[184] K. H. J. Buschow. Structure and properties of some novel ternary Fe-rich rare-earth intermetallics. *Journal of Applied Physics*, 63(8):3130–3135, 1988.

[185] R. B. Helmholdt, J. J. M. Vleggaar, and K. H. J. Buschow. Note on the crystallographic and magnetic structure of $YFe_{10}V_2$. *Journal of the Less Common Metals*, 138(1):L11–L14, 1988.

[186] Y. Wang, J. Shen, N. X. Chen, and J. L. Wang. Theoretical investigation on site preference of foreign atoms in rare-earth intermetallics. *Journal of Alloys and Compounds*, 319(1–2):62–73, 2001.

[187] Z. D. Zhang, W. Liu, J. P. Liu, and D. J. Sellmyer. Metastable phases in rare-earth permanent-magnet materials. *Journal of Physics D: Applied Physics*, 33(22):R217, 2000.

[188] Z. Hu, W. B. Yelon, X. Zhang, and W. J. James. Neutron diffraction and magnetic studies of $RFe_{12-x}T_xC_y$ (R = Y, Er; T = V, Ti, Mo) alloys. *Journal of Applied Physics*, 79(8):5522–5524, 1996.

[189] X. C. Kou, E. H. C. P. Sinnecker, R. Grössinger, G. Wiesinger, T. Zhao, J. P. Liu, and F. R. De Boer. Magnetocrystalline anisotropy of $SmFe_{12-x}Mo_x$ compounds with x = 0.5, 1.0, 1.5, 2.0 or 3.0. *Journal of Magnetism and Magnetic Materials*, 140:1025–1026, 1995.

[190] X. Li, N. Zheng, Z. Hu, and Z. Yuan. Effects of combined substitution of Dy and Mo or Si on the crystal structures and magnetic properties of $Nd_{1-y}Dy_yFe_{11-x}TiM_x$ (M = Mo, Si) compounds. *Science in China Series B: Chemistry*, 52(8):1097–1103, 2009.

[191] V. Neu, L. Schultz, and H. D. Bauer. Grain size dependence of remanence enhancement and coercivity in nanocrystalline Nd-Fe-B-powders. *Nanostructured Materials*, 12(5–8):769–774, 1999.

[192] A. Bollero, O. Gutfleisch, K. H. Müller, L. Schultz, and G. Drazic. High-performance nanocrystalline PrFeB-based magnets produced by intensive milling. *Journal of Applied Physics*, 91(10):8159–8161, 2002.

[193] K. Easterling. *Introduction to the physical metallurgy of welding*. Elsevier, 2013.

[194] T. Saito, H. Miyoshi, and D. Nishio-Hamane. Magnetic properties of SmFeTi nanocomposite magnets with a $ThMn_{12}$ structure. *Journal of Alloys and Compounds*, 519(0):144–148, 2012.

[195] K. Ohashi, T. Yokoyama, R. Osugi, and Y. Tawara. The magnetic and structural properties of R–Ti–Fe ternary compounds. *IEEE Transactions on Magnetics*, 23(5):3101–3103, 1987.

[196] L. Schultz, K. Schnitzke, and J. Wecker. Magnetic hardening of Sm-Fe-Mo, Sm-Fe-V and Sm-Fe-Ti magnets. *Journal of Magnetism and Magnetic Materials*, 83(1–3):254–256, 1990.

[197] Z. Wang and R. A. Dunlap. Investigation of the hard magnetic properties of Sm_2Fe_{17} compounds with Ga substitutions. *Philosophical Magazine B*, 69(1):103–111, 1994.

[198] J. Köble and M. Huth. Preparation and structural analysis of $Fe_{2+x}Ti_{1-x}$ thin films in the C14 Laves phase stability range. *Journal of Crystal Growth*, 234(4):666–678, 2002.

[199] T. S. Chin, W. C. Chang, H. C. Ku, C. C. Weng, H. T. Lee, and M. P. Hung. Structure and magnetic properties of the $ThMn_{12}$ type NdFeM alloys (M=Si/Al/B/transition metals). *IEEE Transactions on Magnetics*, 25(5):3300–3302, 1989.

[200] Y. C. Chuang, C. H. Wu, and Z. B. Shao. Investigation of the Ce–Fe binary system. *Journal of the Less Common Metals*, 136(1):147–153, 1987.

[201] W. J. Ren, J. L. Yang, B. Li, D. Li, X. G. Zhao, and Z. D. Zhang. Magnetostriction and magnetic anisotropy of $(Sm, Ce)Fe_2$ compounds. *Physica B: Condensed Matter*, 404(20):3410–3412, 2009.

[202] E. T. Clementi and D. L. Raimondi. Atomic screening constants from SCF functions. *The Journal of Chemical Physics*, 38(11):2686–2689, 1963.

[203] R. D. Shannon and C. T. Prewitt. Effective ionic radii in oxides and fluorides. *Acta Crystallographica Section B: Structural Crystallography and Crystal Chemistry*, 25(5):925–946, 1969.

[204] J. C. Slater. Atomic radii in crystals. *The Journal of Chemical Physics*, 41(10):3199–3204, 1964.

[205] R. Lorenz, J. Hafner, S. S. Jaswal, and D. J. Sellmyer. Disorder and noncollinear magnetism in permanent-magnet materials with the $ThMn_{12}$ structure. *Physical Review Letters*, 74(18):3688–3691, 1995.

[206] M. Akayama, H. Fujii, K. Yamamoto, and K. Tatami. Physical properties of nitrogenated $RFe_{11}Ti$ intermetallic compounds (R=Ce, Pr and Nd) with $ThMn_{12}$-type structure. *Journal of Magnetism and Magnetic Materials*, 130(1–3):99–107, 1994.

[207] M. Solzi, L. Pareti, O. Moze, and W. I. F. David. Magnetic anisotropy and crystal structure of intermetallic compounds of the $ThMn_{12}$ structure. *Journal of Applied Physics*, 64(10):5084–5087, 1988.

[208] C. Nan-xian, H. Shi-qiang, W. Yu, and S. Jiang. Phase stability and site preference of $Sm(Fe, T)_{12}$. *Journal of Magnetism and Magnetic Materials*, 233(3):169–180, 2001.

[209] D. R. Penn. Stability theory of the magnetic phases for a simple model of the transition metals. *Physical Review*, 142(2):350–365, 1966.

[210] X. Y. Zhang, Y. Guan, L. Yang, and J. W. Zhang. Crystallographic texture and magnetic anisotropy of $\alpha - Fe/Nd_2Fe_{14}B$ nanocomposites prepared by controlled melt spinning. *Applied Physics Letters*, 79(15):2426–2428, 2001.

[211] Z. Chen, Y. Zhang, G. C. Hadjipanayis, Q. Chen, and B. Ma. Effect of wheel speed and subsequent annealing on the microstructure and magnetic properties of nanocomposite $Pr_2Fe_{14}B/\alpha - Fe$ magnets. *Journal of Magnetism and Magnetic Materials*, 206(1–2):8–16, 1999.

[212] O. V. Billoni, S. E. Urreta, L. M. Fabietti, and H. R. Bertorello. Dependence of the coercivity on the grain size in a $FeNdB + \alpha$–Fe nanocrystalline composite with enhanced remanence. *Journal of Magnetism and Magnetic Materials*, 187(3):371–380, 1998.

[213] G. Rieger, M. Seeger, L. Sun, and H. Kronmüller. Micromagnetic analysis applied to melt-spun NdFeB magnets with small additions of Ga and Mo. *Journal of Magnetism and Magnetic Materials*, 151(1–2):193–201, 1995.

[214] A. Jha, H. A. Davies, and R. A. Buckley. Glass forming ability and kinetics of crystallisation of rapidly quenched Nd-Fe-B alloys. *Journal of Magnetism and Magnetic Materials*, 80(1):109–114, 1989.

[215] J. J. Croat. Crystallization and magnetic properties of melt-spun neodymium-iron alloys. *Journal of Magnetism and Magnetic Materials*, 24(2):125–131, 1981.

[216] I. Betancourt and H. A. Davies. Exchange coupled nanocomposite hard magnetic alloys. *Materials Science and Technology*, 26(1):5–19, 2010.

[217] D. Lee, J. S. Hilton, S. Liu, Y. Zhang, G. C. Hadjipanayis, and C. H. Chen. Hot-pressed and hot-deformed nanocomposite $(Nd, Pr, Dy)_2Fe_{14}B/\alpha$–Fe-based magnets. *IEEE Transactions on Magnetics*, 39(5):2947–2949, 2003.

[218] E. Brodu and E. Bouzy. Depth resolution dependence on sample thickness and incident energy in on-axis transmission Kikuchi diffraction in scanning electron microscope (SEM). *Microscopy and Microanalysis*, 23(6):1096–1106, 2017.

[219] M. D. Vaudin. Pseudosymmetry in EBSD patterns. *Microscopy and Microanalysis*, 11(S02):510–511, 2005.

[220] I. S. Tereshina, S. A. Nikitin, T. I. Ivanova, and K. P. Skokov. Rare-earth and transition metal sublattice contributions to magnetization and magnetic anisotropy of R(TM,Ti)$_{12}$ single crystals. *Journal of Alloys and Compounds*, 275(0):625–628, 1998.

[221] A. Kubo, J. Wang, and Y. Umeno. Development of interatomic potential for Nd-Fe-B permanent magnet and evaluation of magnetic anisotropy near the interface and grain boundary. *Modelling and Simulation in Materials Science and Engineering*, 22(6):065014, 2014.

[222] K. J. Strnat. Rare earth-cobalt permanent magnets. In E. P. Wohlfarth and K. H. J. Buschow, editors, *Handbook of Ferromagnetic Materials*, pages 131–209. Elsevier, 1988.

[223] M. Solzi, R. Xue, and L. Pareti. Magnetic anisotropy and first-order magnetization processes in $Sm(Fe_{1-x}Co_x)_{10}M_2$ (M = Ti, Si) compounds. *Journal of Magnetism and Magnetic Materials*, 88(1–2):44–50, 1990.

[224] F. A. Kuijpers. Investigations on the $LaCo_5$-H and $CeCo_5$-H systems. *Journal of the Less Common Metals*, 27(1):27–34, 1972.

[225] Y. G. Pastushenkov, J. Bartolome, N. Suponev, K. P. Skokov, T. Ivanova, A. Larrea, M. Lyakhova, E. Semenova, and S. Smirnov. Stress-induced anisotropy, magnetic domain structure and spin-reorientation transition in $R(FeCo)_{11}Ti$ single crystals (R=Dy, Tb). *Journal of Alloys and Compounds*, 451(1–2):488–491, 2008.

[226] Y. G. Pastushenkov, A. Forkl, and H. Kronmüller. Temperature dependence of the domain structure in $Fe_{14}Nd_2B$ single crystals during the spin-reorientation transition. *Journal of Magnetism and Magnetic Materials*, 174(3):278–288, 1997.

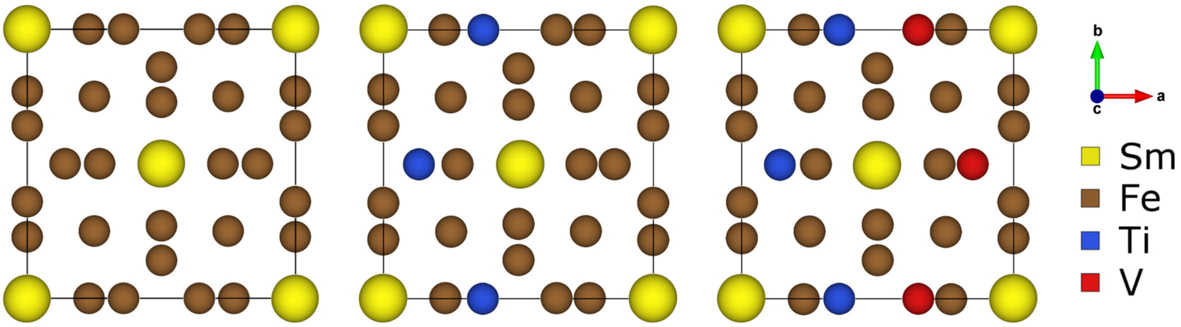

Figure A.1: Input structures of Sm_1Fe_{12} (left), $Sm_1Fe_{11}Ti_1$ (center) and $Sm_1Fe_{10}Ti_1V_1$ (right) for DFT-calculations. According to results of the present work, stabilizing transition metals are situated on 8i-sites.

Table A.1: Compositions of the different intensively milled $Sm_1Fe_{10-x}Al_xMo_2$-powders determined by EDX.

Phase	x	Sm / at.%	Fe / at.%	Al / at.%	Mo / at.%
$Sm_1Fe_{10-x}Al_xMo_2$	0.0	8.1	76.5	-	15.4
	0.8	8.5	71.2	5.8	14.5
	2.0	8.3	61.5	15.6	14.6

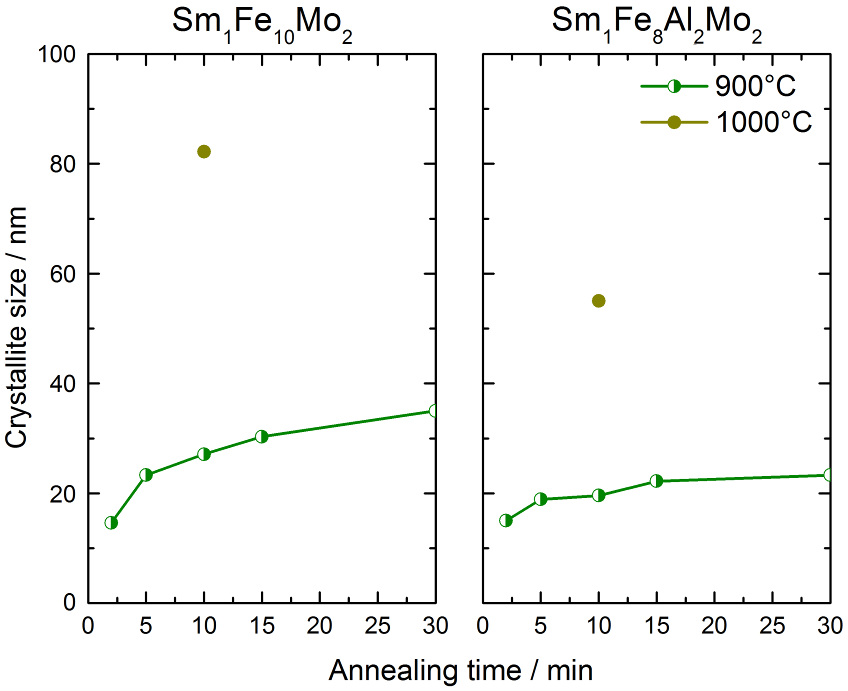

Figure A.2: Development of $Sm_1Fe_{10-x}Al_xMo_2$-crystallite sizes from the as-milled state for different annealing parameters.

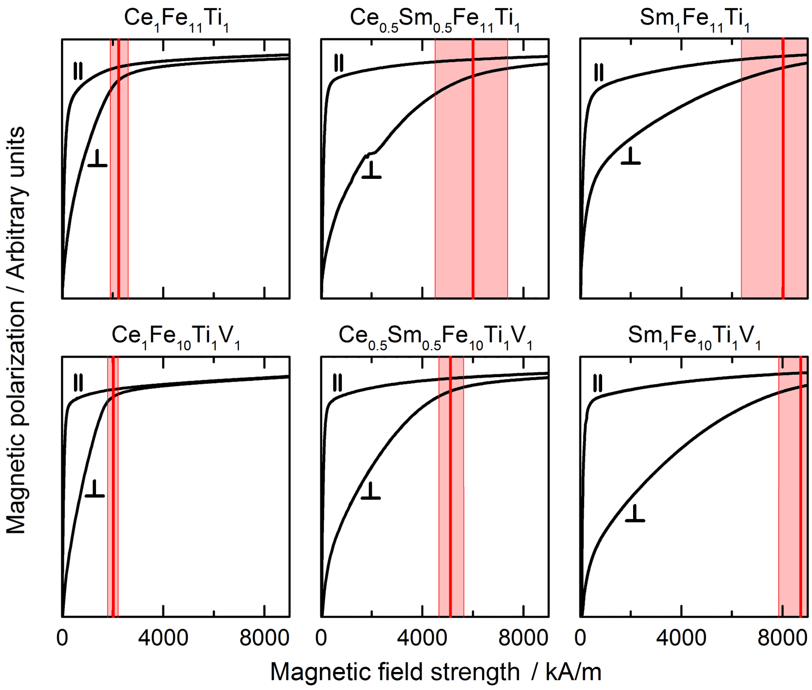

Figure A.3: Determination of the anisotropy field strengths of $Ce_{1-x}Sm_xFe_{11}Ti_1$ and $Ce_{1-x}Sm_xFe_{10}Ti_1V_1$ (x=0.0, 0.5, 1.0) from the intersection of measurements parallel and perpendicular to the easy (c-)axes.

Table A.2: Compositions of the different intensively milled $Ce_{1-x}Sm_xFe_{11}Ti_1$- and $Ce_{1-x}Sm_xFe_{10}Ti_1V_1$-powders determined by EDX.

Phase	x	Ce / at.%	Sm / at.%	Fe / at.%	Ti / at.%	V / at.%
$Ce_{1-x}Sm_x Fe_{11}Ti_1$	0.00	8.8	-	83.3	7.9	-
	0.26	6.4	2.3	82.8	8.5	-
	0.52	4.1	4.5	82.8	8.6	-
	0.73	2.0	5.4	84.4	8.2	-
	0.75	2.2	6.6	82.6	8.6	-
	1.00	-	8.2	83.9	7.9	-
$Ce_{1-x}Sm_x Fe_{10}Ti_1V_1$	0.00	9.2	-	75.0	7.9	7.9
	0.17	7.4	1.5	74.8	8.5	7.8
	0.26	6.2	2.2	76.3	7.5	7.7
	0.35	5.9	3.2	75.3	7.9	7.7
	0.47 (7 at.% RE)	3.7	3.3	77.1	8.1	7.8
	0.51 (8 at.% RE)	4.0	4.1	74.8	8.9	8.2
	0.49 (9 at.% RE)	4.5	4.3	74.9	8.0	8.3
	0.47 (10 at.% RE)	5.4	4.8	73.2	8.4	8.3
	0.73	2.0	5.2	77.3	7.7	7.9
	0.72	2.4	6.2	74.3	9.0	8.2
	1.00	-	9.3	72.9	9.3	8.5

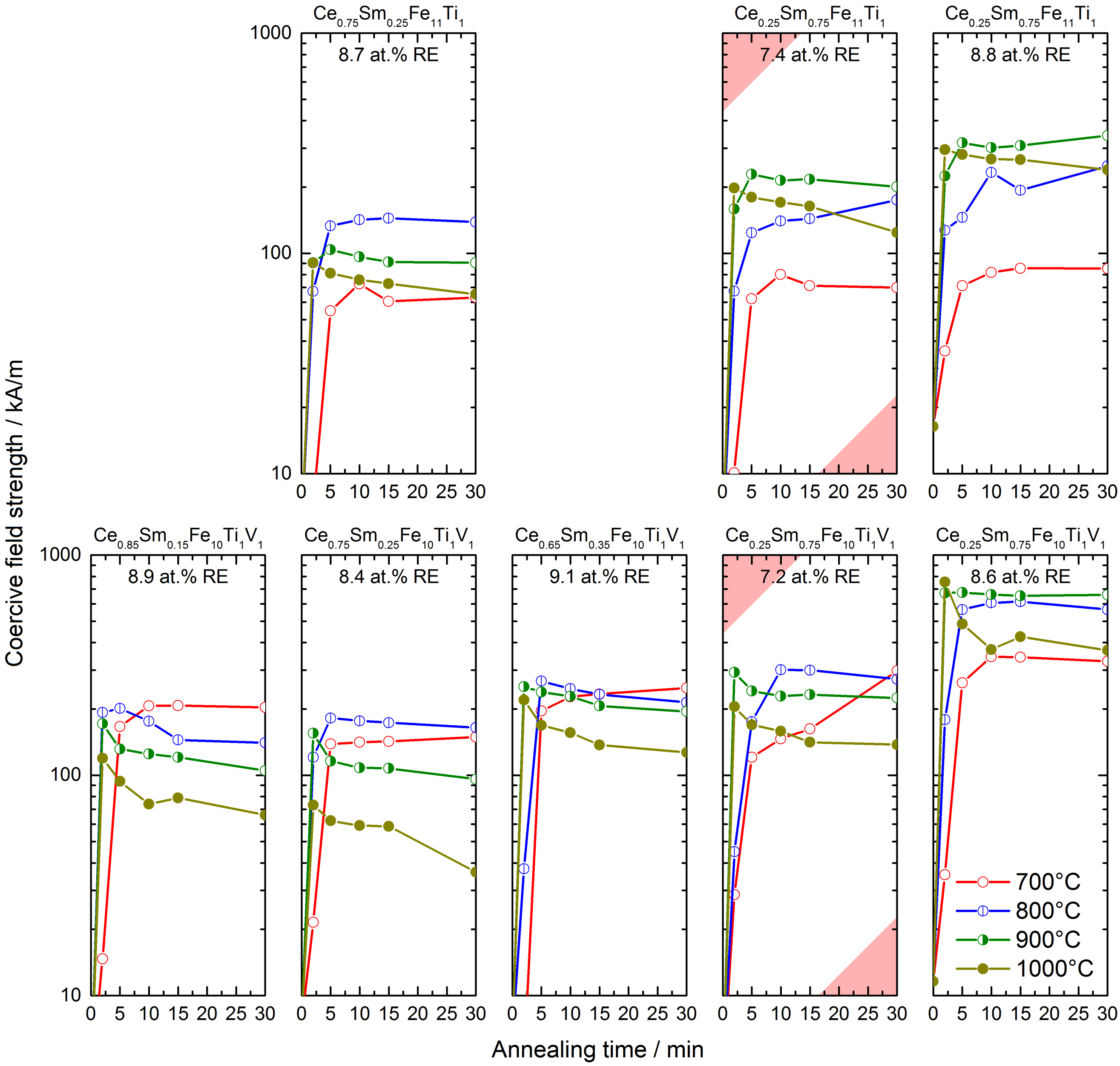

Figure A.4: Coercivities measured on intensively milled and subsequently annealed $Ce_{1-x}Sm_xFe_{11}Ti_1$- and $Ce_{1-x}Sm_xFe_{10}Ti_1V_1$-powders. Red edges indicate compositions with too low RE-content (supplementary to Figure 4.19).

Table A.3: Temperature coefficients α and β of intensively milled and annealed $Ce_{1-x}Sm_xFe_{11}Ti_1$- and $Ce_{1-x}Sm_xFe_{10}Ti_1V_1$-powders together with the corresponding values for the nanocrystalline bulk samples from Ga-containing $Ce_{0.5}Sm_{0.5}Fe_{10}Ti_1V_1$-melt-spun ribbons.

Phase	x	$\alpha(B_r)$ / %/°C	$\beta(H_c)$ / %/°C
$Ce_{1-x}Sm_x$ $Fe_{11}Ti_1$	0.00	-	$-0.46_{\pm 0.01}$
	0.26	-	$-0.47_{\pm 0.02}$
	0.52	-	$-0.68_{\pm 0.01}$
	0.75	-	$-0.40_{\pm 0.02}$
	1.00	-	$-0.51_{\pm 0.01}$
$Ce_{1-x}Sm_x$ $Fe_{10}Ti_1V_1$	0.00	-	$-0.46_{\pm 0.01}$
	0.26	-	$-0.46_{\pm 0.02}$
	0.49	-	$-0.58_{\pm 0.01}$
	0.51 (HP)	$-0.13_{\pm 0.01}$	$-0.46_{\pm 0.01}$
	0.51 (DU $\dot{\varphi}$ = 0.01)	$-0.20_{\pm 0.01}$	$-0.60_{\pm 0.03}$
	0.72	-	$-0.38_{\pm 0.02}$
	1.00	-	$-0.43_{\pm 0.01}$

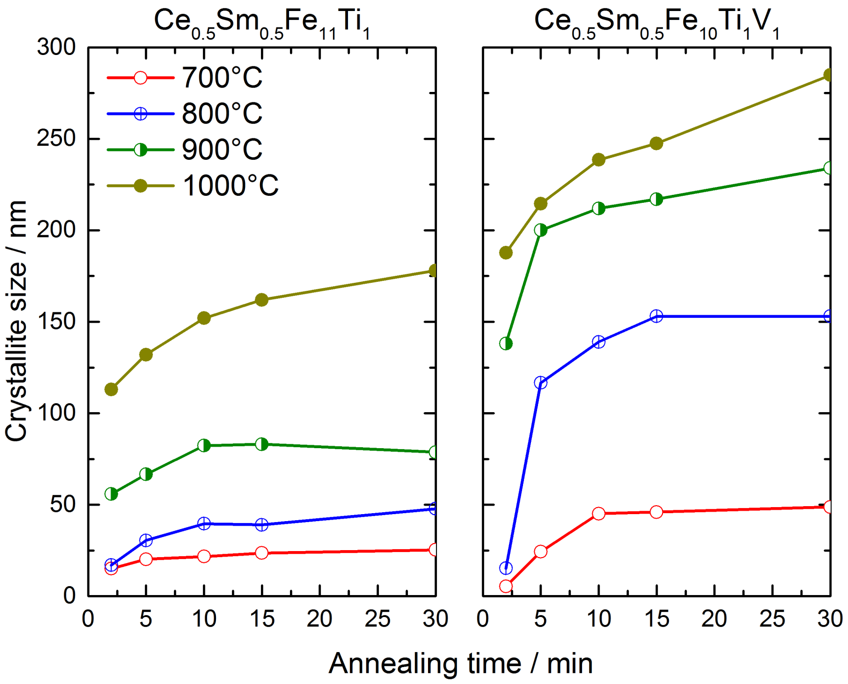

Figure A.5: Development of $Ce_{1-x}Sm_xFe_{11}Ti_1$- and $Ce_{1-x}Sm_xFe_{10}Ti_1V_1$-crystallite sizes from the as-milled state for different annealing parameters.

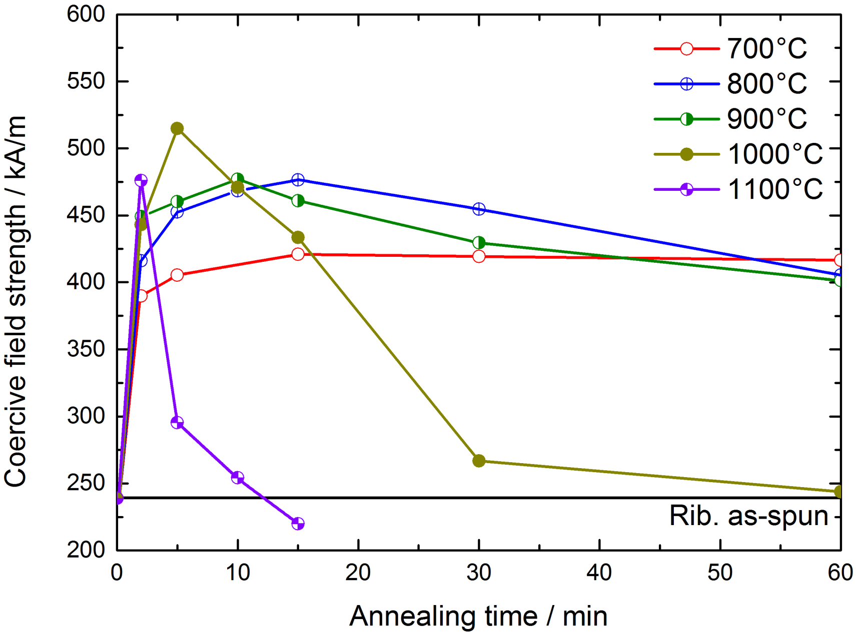

Figure A.6: Coercivities measured on melt-spun (25 m/s) and subsequently annealed Ga-containing $Ce_{0.5}Sm_{0.5}Fe_{10}Ti_1V_1$-ribbons.

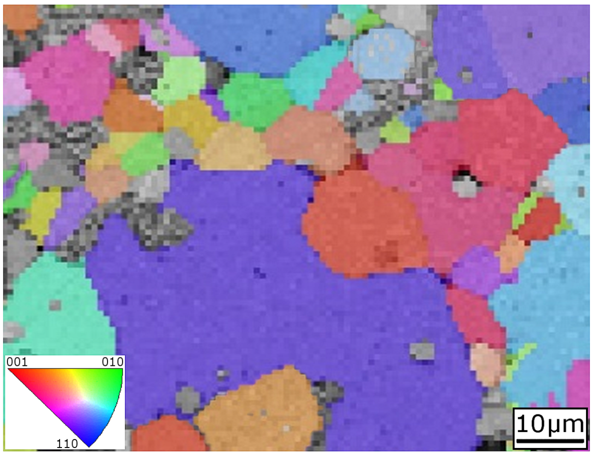

Figure A.7: EBSD-image of a melt-spun ribbon from Ga-containing $Ce_{0.5}Sm_{0.5}Fe_{10}Ti_1V_1$ that has been annealed for 150 h at 1000 °C.

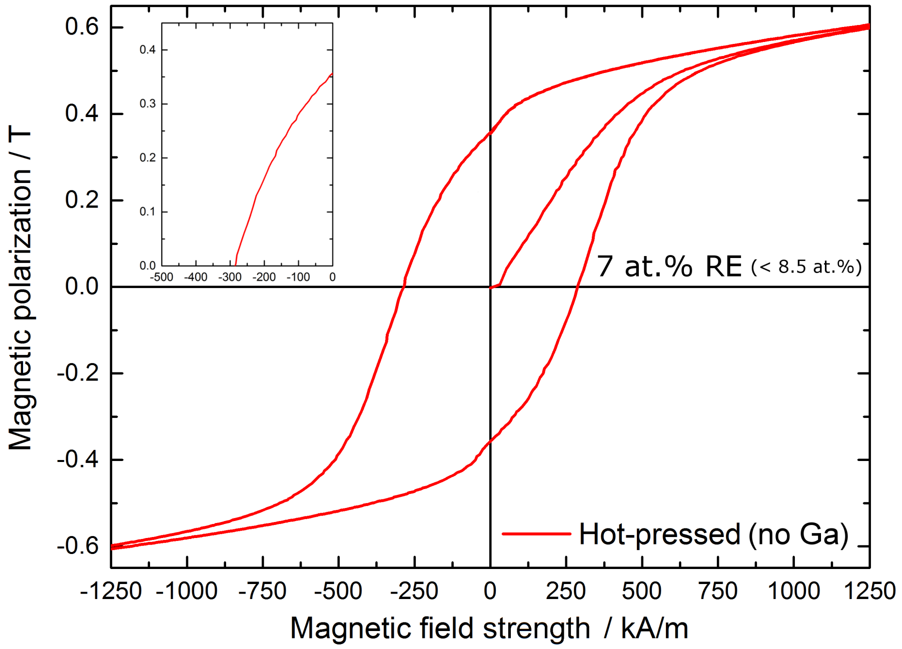

Figure A.8: Magnetic characterization of the hot-pressed magnet produced from Ga-free melt-spun ribbons. The inset shows a magnified section of the demagnetization curve. Note the slightly understoichiometric RE-content.

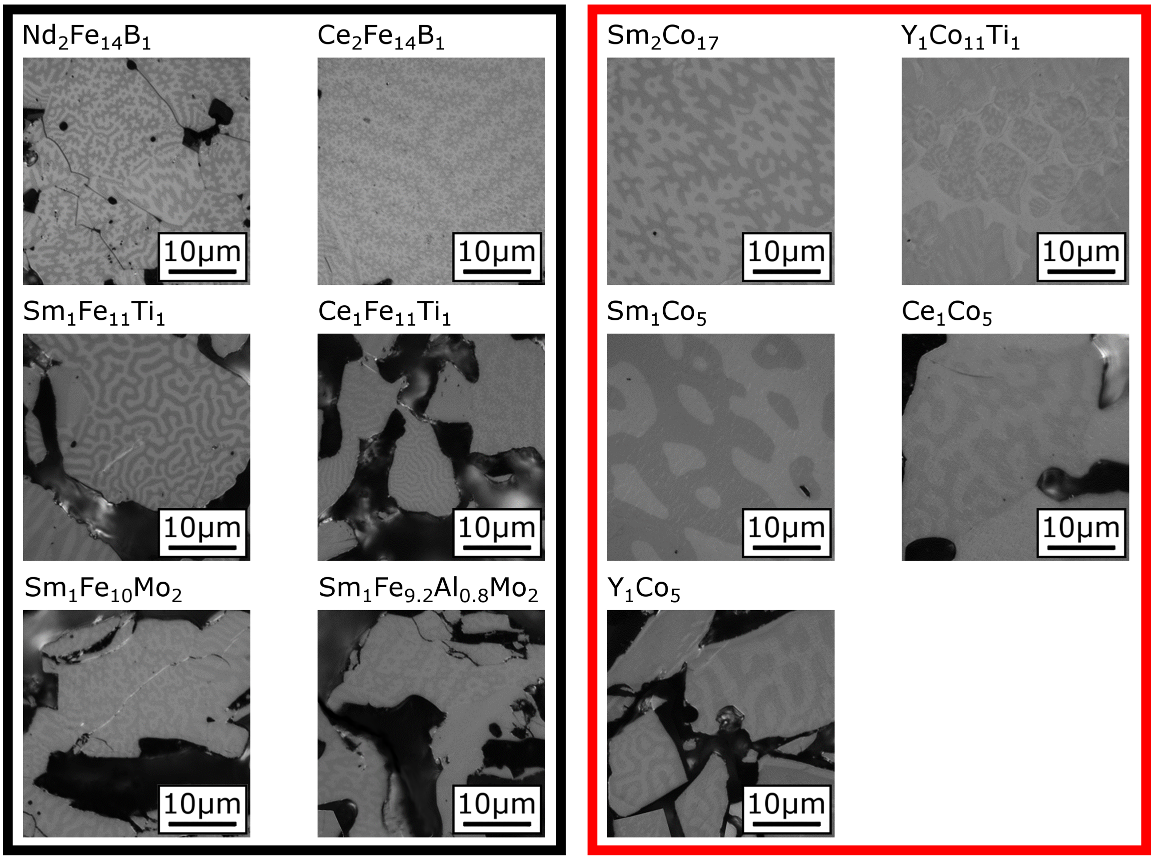

Figure A.9: Domain patterns of Fe- and Co-based samples for evaluations regarding their intrinsic magnetic properties. The patterns have different contrasts, characteristic lengthscales and shapes.

Acknowledgements

The presented results have been obtained during a collaboration between the Robert Bosch GmbH and the Technische Universität Darmstadt in the period from May 2015 to April 2018. More precisely, the involved parties are Bosch's corporate sector research and advance engineering in Renningen and the Functional Materials group of the university's Materials Science department.

Special gratitude is due to my doctoral thesis supervisor Prof. Dr. Oliver Gutfleisch. I joined his group for a research internship during my master studies, shortly after the group moved to Technische Universität Darmstadt. From his valuable academic advice, the experimental freedom and the pleasant and capacious working environment, I have benefited ever since. As part of his group, I have been introduced to the community of researchers on magnetic materials, including the exchange with international experts in this field. This have been very motivating experiences. I thank him for accepting the scientific supervision of my subsequent employment as Ph.D. student at Bosch, allowing the persistent contact to the whole group and the possibility to write my thesis in association with my university in Darmstadt.

I especially appreciate the efforts of Dr. Holger Wüst as my supervisor on-site in the company. He was a patient supporter throughout the entire period. With valuable scientific advice and discussions, he has steadily accompanied the progress of my interesting subject.

I greatly thank Bosch for having accepted my application as doctoral researcher, thus giving me the opportunity to professionally investigate new ferromagnetic materials. The company has persistently promoted my participation at international events and provided an advanced laboratory- and analysis infrastructure. Not least, fruitful discussions with internal experts from different areas and invited guests have contributed to a good example for the collaboration of industry and academia. I would like to thank the associates of the departments for functional materials and analytics for contributing to a pleasant and inspiring working atmosphere. Particularly noteworthy are Dr. Jürgen Rapp as head of the department and Dr. Witold Pieper, the group leader for electronic and magnetic materials. I have especially enjoyed working together with my dear colleagues Mr. Jürgen Oberle, Dr. Lars Bommer, Dr. Arne Huber, Dr. Jens Burghaus, Dr. Bernd Reinsch, Mr. Wolfgang Rammaier and Mr. Ralf Holzschuh. For performing the density functional-simulations, I thank Dr. Anika Marusczyk from the simulations team.

I would also like to emphasize the support of several colleagues from the neighboring analytics department for offering me an open and uncomplicated access to various characterization devices and assistance in dealing with these, whenever needed. It was a great experience to carry out far-reaching analyses independently at any time. Special thanks are due to Dr. Thomas Köhler for sharing his expertise in the interpretation of X-ray- and neutron diffractograms. In this context, I also appreciate that Prof. Dr. Helmut Ehrenberg (Karlsruhe Institute of Technology) and Dr. Anatoliy Senyshyn (Technische Universität München) were willing to perform the neutron diffraction experiments and took their time for discussions of their outcome. Among the analysts, Mr. Stefan Hinderberger deserves a special place in this section for his outstanding efforts regarding the careful and time-consuming ion beam preparation of lamellas. He also performed the analyses and contributed with fruitful discussions. I thank Dr. Lars Epple and

Dr. Christiane Müller for further basic introductions to X-ray diffraction and the calibration and maintenance of the devices. Likewise, I thank Dr. Friederike Köppen and Ms. Ingrid Wührl for introducing me to all relevant practices regarding materialography, scanning electron microscopy and the imaging of domains with polarized light. I further acknowledge the analytical support of Ms. Bozena Siekierka and Mr. Mario Tuchen for the quantification of elemental compositions by chemical means as well as thermoanalytical techniques, respectively.
Lastly, I want to mention my doctoral colleagues at Bosch for their contribution to the nice working environment and Mr. Jérôme Fliegans, Mr. Marco Meier, Mr. Simon Colanges, Mr. Jérémi Pirat and Mr. Dennis Kamuf who have been interns at the company and temporary companions in the laboratory.

I had the chance to accompany the recommissioning of a fast in-situ X-ray diffractometer for temperature-resolved analysis. I thank the external employee Mr. Oliver Pursche for training me with this exciting device despite no measurements were included in the final thesis.

I am equivalently grateful to the former and current members of the Functional Materials group in Darmstadt. In any sense, it has always been a great pleasure with them. It has been very exiting to see their individual progress and the evolution of the group from its beginnings in Darmstadt. The group actively contributed to the success of my experiments at Technische Universität Darmstadt. Beyond the scientific expertise, they have established a very nice and friendly atmosphere, which I have greatly appreciated as a longtime companion. I would like to express my thanks to Dr. Simon Sawatzki who kindly agreed to perform the hot-pressing and die-upsetting experiments with his great experience. I am very happy for the help and inspiring discussions with Dr. Léopold Diop, Dr. Konstantin Skokov and Dr. Ilya Radulov who were likewise performing magnetic measurements in high fields as an asset to my work. I want to highlight the technical assistance of Mr. Fernando Maccari, Ms. Gabi Andress and Ms. Helga Janning who were responsible for the melt-spinner and helped as second pair of hands to process the material at the very best conditions. I further acknowledge the help of Mr. Andreas Taubel, host of the vibrating sample magnetometer. Additionally, I want to mention Dr. Maximilian Fries, Dr. Tim Helbig, Dr. Semih Ener and the secretary of the Functional Materials group, Ms. Maija Laux.

In addition to the acquired expertise, it was great for me to get in touch with the latest characterization methods and the various elements of the periodic table. Beyond the specific research, I also want to mention Mr. Johannes Kroder who has always been a close partner with fundamental interest and fascination for magnetism.
Equally, I would like to pay tribute to the group of my closest friends, who also know that they are meant without being explicitly named.

To finish, I express my deepest gratitude for three loved persons with a higher-level role for the present work. These are my parents Ms. Ute Simon and Mr. Günter Simon who support me and are always there for me. Similarly, I am very grateful to Ms. Milena Simon for all her love and support.

Curriculum Vitae

Daniel Simon

Date / place of birth
21.05.1990 / Darmstadt

Nationality
German

Professional activities	
05 / 2018 – To date	**Development Engineer**: Function of lambda sensors Robert Bosch GmbH (Powertrain Solutions), Stuttgart-Feuerbach
Doctorate	
05 / 2015 – 04 / 2018	**Ph.D. thesis**: Development and Assessment of Rare Earth-lean Th_1Mn_{12}-Phases for the Use in Permanent Magnets Robert Bosch GmbH (Corporate Research), Renningen
Academic studies	
10 / 2012 – 04 / 2015	**Master's degree (M.Sc.) Materials Science** Master thesis: Influence of Microstructural Parameters on the Diffusion of Heavy Rare Earth-Elements in Sintered Nd-Fe-B Permanent Magnets Technische Universität Darmstadt
09 / 2013 – 03 / 2014	**7-month semester abroad** Graduate School of Chemistry, Biology and Physics, Bordeaux
10 / 2009 – 10 / 2012	**Bachelor's degree (B.Sc.) Materials Science** Bachelor thesis: Deformation Mechanisms in Nanocrystalline Copper: Molecular Dynamics-Simulations on the Influence of Strain Rate and Temperature Technische Universität Darmstadt
Education	
06 / 2009	**General qualification for university entrance** Albert-Einstein-Schule, Groß-Bieberau

Scientific Publications, Contributions and Attendances

Publications

I D. Simon, H. Wüst, T. Köhler, A. Senyshyn, H. Ehrenberg, and O. Gutfleisch. The quaternary system Sm-Fe-Mo-Al and the effect of Al substitution on magnetic and structural properties of its $ThMn_{12}$ phase. *Journal of Alloys and Compounds*, 770:301–307, 2019.

II D. Simon, H. Wüst, S. Hinderberger, T. Köhler, A. Marusczyk, S. Sawatzki, L.V.B. Diop, K. Skokov, F. Maccari, A. Senyshyn, H. Ehrenberg, and O. Gutfleisch. Structural and magnetic properties of $Ce_{1-x}Sm_xFe_{11-y}Ti_1V_y$. *Acta Materialia*, 172:131–138, 2019.

Contributions

I IEEE Magnetics Summer School 2017 at Palacio de la Magdalena (Santander, Spain)

Attendances

I 24th International Workshop on Rare Earth and Future Permanent Magnets and Their Applications, REPM 2016 (Darmstadt, Germany)